INFORMATION TO USERS

This manuscript has been reproduced from the microfilm master. UMI films the text directly from the original or copy submitted. Thus, some thesis and dissertation copies are in typewriter face, while others may be from any type of computer printer.

The quality of this reproduction is dependent upon the quality of the copy submitted. Broken or indistinct print, colored or poor quality illustrations and photographs, print bleedthrough, substandard margins, and improper alignment can adversely affect reproduction.

In the unlikely event that the author did not send UMI a complete manuscript and there are missing pages, these will be noted. Also, if unauthorized copyright material had to be removed, a note will indicate the deletion.

Oversize materials (e.g., maps, drawings, charts) are reproduced by sectioning the original, beginning at the upper left-hand corner and continuing from left to right in equal sections with small overlaps. Each original is also photographed in one exposure and is included in reduced form at the back of the book.

Photographs included in the original manuscript have been reproduced xerographically in this copy. Higher quality 6" x 9" black and white photographic prints are available for any photographs or illustrations appearing in this copy for an additional charge. Contact UMI directly to order.

UMI

A Bell & Howell Information Company
300 North Zeeb Road, Ann Arbor MI 48106-1346 USA
313/761-4700 800/521-0600

Dissipation Studies in $Y_1Ba_2Cu_3O_7$ Using Torsional Oscillators

Approved by
Dissertation Committee:

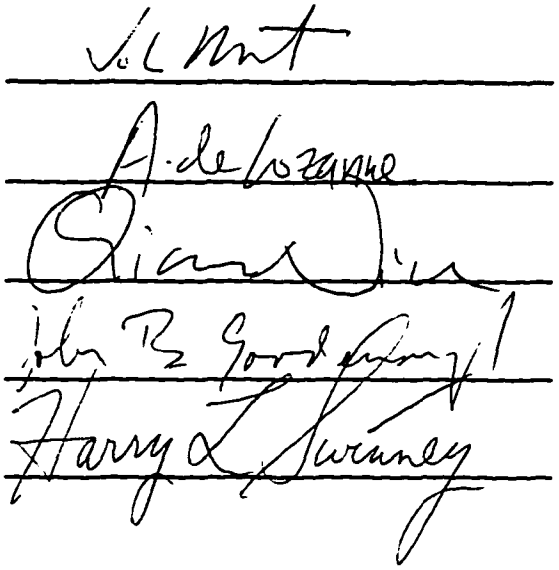

Dissipation Studies of $Y_1Ba_2Cu_3O_7$ Using Torsional Oscillators

by

Alexander Lloyd Barr, B.S.

Dissertation

Presented to the Faculty of the Graduate School of

The University of Texas at Austin

in Partial Fulfillment

of the Requirements

for the Degree of

Doctor of Philosophy

The University of Texas at Austin

December, 1996

Dedication

First and foremost I dedicate this dissertation to my family. Next I dedicate it to all the good teachers whom I have been fortunate to have had.

Acknowledgements

Professor Markert is not just a decent person but also a wise educator. His advisorial style has taught me to have confidence and vision when trying to obtain a goal and also to keep moving forward not only over obstacles but around them...and yes, he is patient also. I wish to thank my close friends Arturo Morosoff, Georgios Georgakis, and Cyrus Bharucha for making graduate school a truly enjoyable experience; for the rest of my life I will have good memories of this time. To Johnathan Cobb and all of the lab"ites", present and past, I have learned from you all. P.S., Johnathan, you can have the lock-in amplifier back now. :-) Special thanks to Chris Wooten for assembling the cryostat. Jesse Martinez, Harold Williams, Jim Pinget, Les Devers, Ed Knight, Mr. "Barbecue" Canon, and the rest of the shop, your help has been invaluable.

Last but not least, I wish to thank my father, who is one of the better scientists I have ever met; I say this not just as your son but also as your friend. Thank you all.

Dissipation Studies in $Y_1Ba_2Cu_3O_7$ Using Torsional Oscillators

Publication No._____

Alexander Lloyd Barr, Ph.D.

The University of Texas at Austin, 1996

Supervisor: John Markert

Energy dissipation from flux motion is studied in single crystal $YBa_2Cu_3O_7$ with high–Q torsional oscillators. The oscillator technique, which utilizes micro-machined single crystal silicon and a unique double torsional structure to produce oscillators of exceptional sensitivity, is developed. Samples can be coupled to the oscillator and vibrated in an external dc magnetic field so losses resulting from the coupling of the sample to field may be measured. A new torsioinal mode of dissipation based on the width and length of the crystal has been found with this technique. The dissipation is fitted against Brandt Dissipation Theory. The anisotropy of the crystal and twins is added to Brandt's theory and a twin anisotropy between 1–2 is estimated . A further experiment has demonstrated for the first time an amplitude dependence for the dissipation from these types of measurements. Additional fine structure is seen in the dissipation

curves at low amplitudes of vibration and is considered in terms of an intrinsic pinning model.

Table of Contents

List of Tables

List of Figures

Chapter 1: Introduction

"There are few subjects as difficult as magnetism..."

Encyclopedia Britannica

"...except for high temperature superconductivity."

Alexander Barr

Superconductivity is a unique field of physics. Its explanation lies in a crossroad where thermodynamic descriptions blend with quantum mechanical ones. For high T_c materials, the quantum picture is still unraveling, so more often than not, one must stick with the very clever thermodynamic picture drawn out by Ginzburg–Landau theory.

GINZBURG–LANDAU THEORY

GL theory [Ginzburg, 1950] rests on the premise that the free energy density, f, can be expanded in a power series of a complex order parameter, ψ:

$$f = f_{n0} + \alpha|\psi|^2 + \frac{\beta}{2}|\psi|^4 + \frac{1}{2m^*}\left|\left(\frac{\hbar}{i}\nabla - \frac{e^*}{c}\mathbf{A}\right)\psi\right|^2 + \frac{h^2}{8\pi} \qquad 1.1$$

ψ is sometimes considered a psuedowavefunction for an electron pair such that $|\psi|^2$ is the local density of superconducting electrons. f_{n0} is the free energy

density of the normal state, α and β are expansion coefficients, m^* is the mass of the Cooper pair [Cooper, 1956], and h is the local microscopic field. ψ is small and is assumed to vary slowly becoming zero above the transition temperature and approaching a value, ψ_∞ infinitely deep in the interior of the superconductor. Note, because ψ is complex, it is often convenient to write it as $\psi = |\psi|e^{i\phi}$. By integrating Eq. 1.1 over a volume, one may find the actual free energy. Just as one starts with a Hamiltonian and minimizes it to find the equations of motion, so may one minimize the free energy to get the "equations of motion" for a superconductor, the Ginzburg–Landau equations.

$$\alpha\psi + \beta|\psi|^2\psi + \frac{1}{2m^*}\left(\frac{\hbar}{i}\nabla - \frac{e^*}{c}\mathbf{A}\right)^2\psi = 0 \qquad 1.2$$

$$\mathbf{J} = \frac{e^*}{m^*}|\psi|^2\left(\frac{\hbar}{i}\nabla - \frac{e^*}{c}\mathbf{A}\right). \qquad 1.3$$

The length scale over which the order parameter varies is ξ, the coherence length. The coherence length is sometimes thought of the as the width of the psuedowavefunction or the separation of the Cooper pair. It diverges as the material becomes normal. The other major length scale associated with superconductors is the penetration depth, λ, which is given by

$$\lambda^2 = \frac{m^* c^2}{4\pi|\psi|^2 e^{*2}}. \qquad 1.4$$

The penetration depth gives the length over which screening currents and the field fall off as one moves further into the superconductor. For many of the high–T_c materials like YBCO ($Y_1Ba_2Cu_3O_{6.95}$), the coherence length and penetration depth are dependent on the direction. Equation 1.1 can be generalized for this case (Lawrence–Doniach model [Lawrence, 1971]).

The structure of the material may produce anisotropies for λ and ξ. For YBCO, CuO_2 planes carry most of the current with CuO chains acting as charge reservoirs. Insulating layers separate these (see Fig. 1.1).

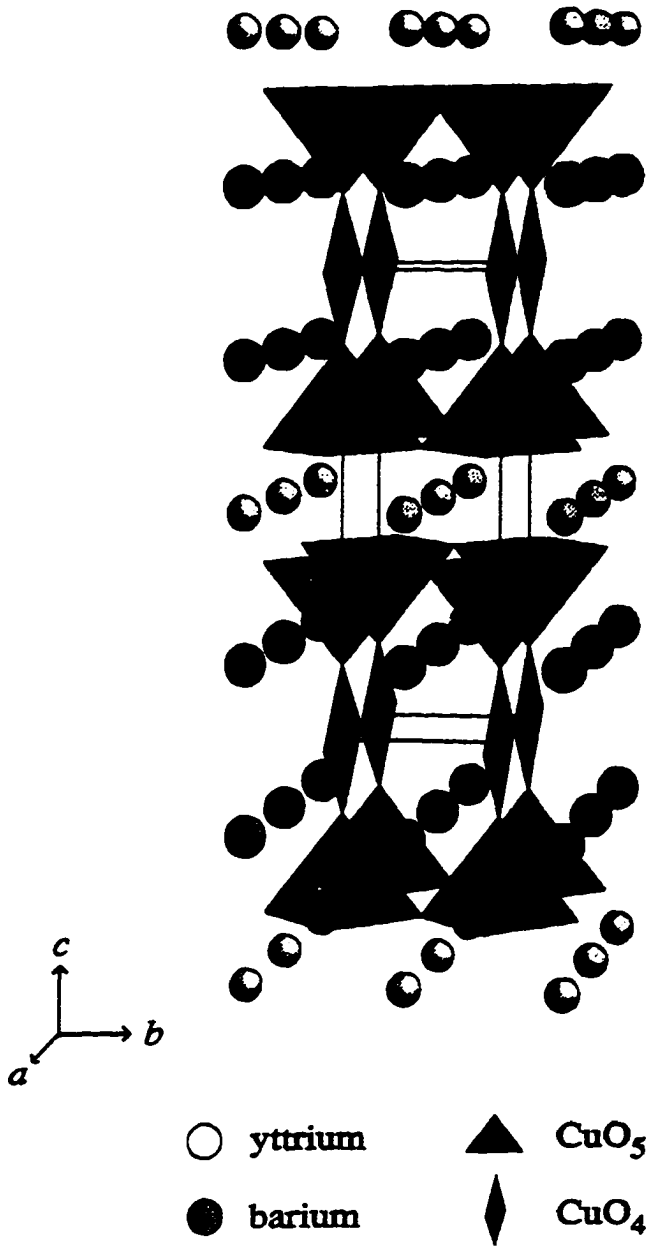

FIG. 1.1 Structure of YBCO with CuO_2 planes and CuO chains.

The spacing between the sets of CuO_2 planes is ~10 Å. This structural anisotropy, for example, makes current flow easier in the CuO (a–b) plane rather than perpendicular to it (along the c–axis). The coherence length is also different; $\xi_{ab}/\xi_c \approx 5.5$.

Another interesting property of these materials is that unlike many metallic superconductors, the coherence length (ξ_{ab} = 34 Å) is relatively short and penetration depth (λ_{ab} = 1200 Å) is relatively long. The ratio of these quantities, λ/ξ, gives the Ginzburg–Landau parameter, κ.. For $\kappa > 1/\sqrt{2}$, the superconductor will be of type II—it will have a phase in which flux can penetrate the material—while for $\kappa < 1/\sqrt{2}$, the superconductor will be of type I—the superconductor will always try to exclude flux [Abrikosov, 1957]. For some materials like the high–T_c materials, allowing some flux to penetrate in a certain temperature and field ranges lowers the free energy; i.e., at 200 Oe YBCO is type II between 56 K and 93 K [Dong–Ho, 1990].

Where the flux enters the material, it is normal. If one applies a field to a type II material, first a single vortex will enter, then as the field increases further, more vortices will enter until they overlap and the material becomes normal everywhere, thus, the upper critical field will have been reached. Looking at the field in a single vortex relative to position, one can describe the vortex as a having a normal core of radius ξ and having an exponential tail which falls off with characteristic length λ. (Fig. 1.2).

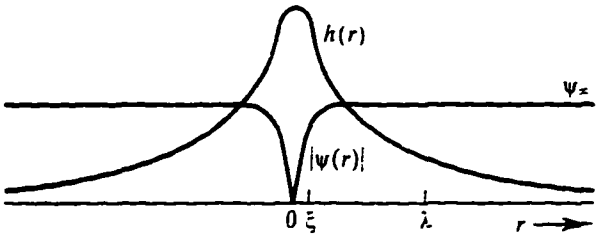

FIG. 1.2. Field and order parameter spatial dependence for a single vortex [Tinkham, 1996].

Interestingly enough the tubes of flux organize themselves much the same way as atoms do. The flux tubes form fluids, glasses, and the famous triangular Arikosov lattice of flux lines! The flux line is shielded from the bulk of the material by screening supercurrents which repel each other, so the vortices repel just as one would expect a plane filled with current rings to repel and spread out. Clearly the vortices interact—the exponential tail of one influencing the supercurrents of another. Needless to say that there are many exciting interactions and phenomena associated with this pseudo state of matter.

One current area of interest is energy dissipation which arises from flux motion—a moving vortex is a moving packet of normal state electrons which will, of course, dissipate energy. If the vortices are intentionally moved, one can use the dissipation to study the transition of going from a vortex liquid to a vortex solid. The dissipation as a function of temperature is considered in terms of flux

diffusion modes and intrinsic pinning of the flux lines by the crystal structure in chapters 4 and 5.

To study this topic, a new experiment was developed utilizing torsional oscillators. A torsional oscillator is a mechanical vibrator with two sections that twist opposite each other—this leads to a higher quality factor, Q, for the oscillator as examined in chapter 2. Similarly to a vibrating reed technique, a YBCO sample is glued to the oscillator. If the oscillator vibrates in the presence of a dc magnetic field, the sample will actually see an ac field because of the motion. Both the oscillator's motion and its response occur across a capacitive gap. The oscillators are made from single crystal silicon (see chapter 3) which gives higher Q's . The high Q's, 100 000+, and small drive amplitude, ~10 Å, allow for sensitive measurments. The samples were high quality single crystal YBCO grown from a flux. Crystals with rectangular geometry and unidirectional twin boundaries were chosen for these experiments. Note these same kinds of crystals were also provided for other studies and many other groups.

The dissipation, $1/Q$, can be monitored as a function of temperature and field. Doing so has shown multiple dissipation peaks [Barr, 1995] rather than the expected one peak normally seen going through the superconducting transition. In these experiments, a new torsional mode is hypothesized and fits the data. The twin boundaries are also included in the flux diffusion mode theory of Brandt. Various pinning parameters for different crystals have been found to be in agreement with other groups. The initial part of the dissipation curves also fits Brandt's theory and can be used to map out the irreversibility line, however, the secondary shoulder and width of some curves does not fit Brandt's modes. This

deviation may result from a distribution of length scales created by gluing the crystal on at an angle as explained in chapter 5. Further structure appears in the dissipation curves, which is shown to be sensitive to drive amplitude [Barr, 1996]. The fine structure also appears in field sweeps and in the frequency change. The fine structure is considered from the framework of intrinsic pinning of the vortex core by the CuO planes as theorized by Tachiki.

Finally a very small test study was carried out to see if oscillators could be used to study dissipation in thick aluminum films.

A photo of the experiment follows: oscillator electronics is on the left, magnet and temperature control electronics is on the right and the cross in the center is the probe in the Dewar.

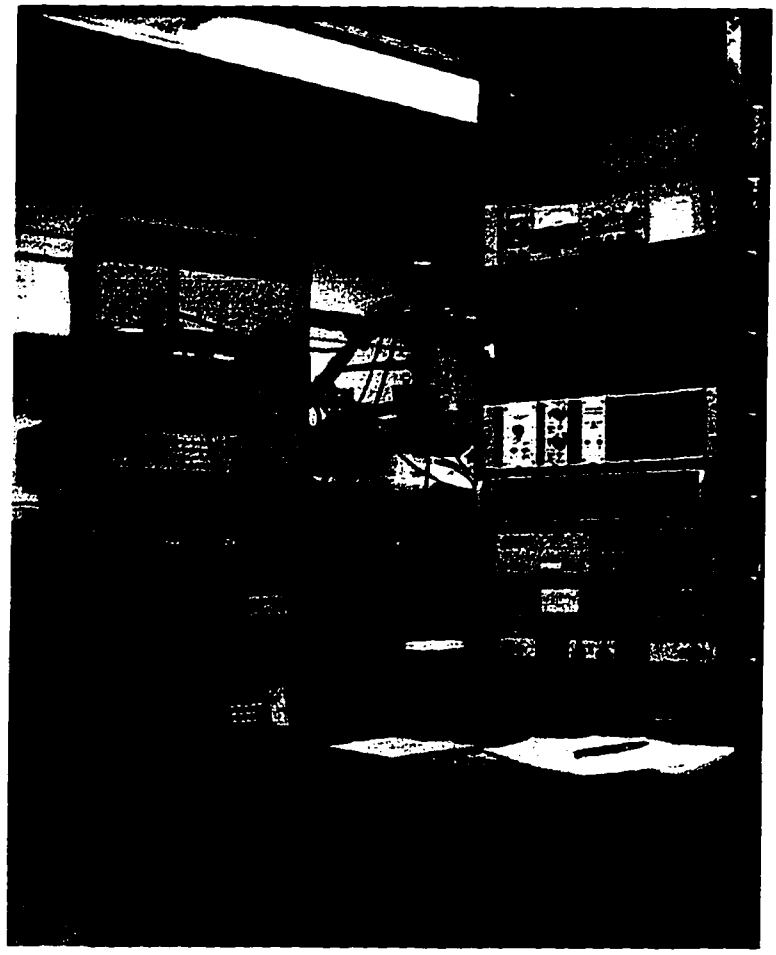

FIG. 1.3. Experimental set up.

Chapter 2: Small Force Detection With Oscillators

A Slinky, a Slinky, a Slinky's a wonderful toy.
A Slinky, a Slinky, for every girl and boy.

Mr. Slinky

INTRODUCTION.

Chapter 2 contains a blend of material on small force detection with oscillators. This chapter is partly a background chapter discussing simple oscillator theory and partly an experimental chapter discussing properties of the double torsional oscillators and related notes for using them in any small force measurement.

The basic idea

Two characteristics of an oscillating system are its resonant frequency and its Q. The resonant frequency can be thought of as the frequency at which the oscillator likes to oscillate. For a simple mass on a spring, it would depend on the mass and on the restoring force of the spring. The Q of an oscillator is a measure of its energy efficiency, in other words, how quickly it loses energy to the outside world during each cycle. Coupling an additional restoring force, such as an extra spring, to our simple mass and spring would change the resonant frequency.

Similarly, if one were to add more damping to the oscillator, such as gumming up the spring with glue, this would cause a decrease in the Q as the oscillator would dissipate more energy, E, per cycle. Technically, the Q is sometimes defined as

$$Q \equiv 2\pi \frac{\langle E \rangle_{\text{per cycle}}}{E_{\text{dissipated per cycle}}} \tag{2.1}$$

Thus by measuring changes in the Q and resonant frequency of a harmonic oscillator, information about restoring and or dissipative forces coupled to the oscillator can be ascertained.

GENERAL THEORY

As is so often the case, one begins with Newton's second law. Newton's law for a damped driven harmonic oscillator is:

$$M\ddot{x}(t) + M\omega_0^2 x(t) + M\Gamma\dot{x}(t) = F_0 \cos\omega t \tag{2.2}$$

where M is the mass of the oscillating object, ω_0 is the natural frequency (normal mode frequency) of the undriven undamped system, Γ is the damping constant, and F_0 is the amplitude of the driving force. Note, the resonances of the driven system are the normal modes of the undamped undriven system [Crawford, 1968]. If one looks at the motion after some time, $\tau=1/\Gamma$, when the transient oscillations have largely died out, the motion is in the steady state and Eq. (2.2) has the solution

$$x_{s.s.} = A_{ab} \sin\omega t + A_{el} \cos\omega t \tag{2.3}$$

where the absorptive amplitude, A_{ab}, which is 90° out of phase with the driver and the elastic amplitude, A_{el}, which is in phase with the driver are given by

$$A_{ab} \equiv \frac{F_0}{M} \frac{\Gamma\omega}{\left[\left(\omega_0^2 - \omega^2\right)^2 + \Gamma^2\omega^2\right]} \tag{2.4a}$$

$$A_{el} \equiv \frac{F_0}{M}\frac{\left(\omega_0^2-\omega^2\right)}{\left[\left(\omega_0^2-\omega^2\right)^2+\Gamma^2\omega^2\right]} \tag{2.4b}$$

respectively. These two amplitudes are shown in Fig. 2.1.

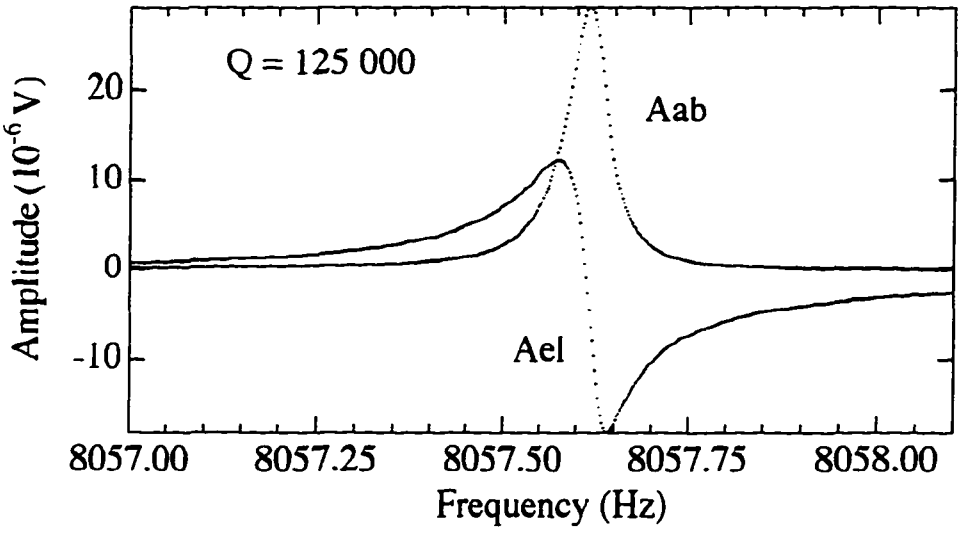

FIG. 2.1. Amplitude of a torsional oscillator, osc1, versus frequency. The amplitude has been split into two components: the elastic and the absorptive parts.

At resonance, $\omega = \omega_0$ (the resonance condition), the amplitude of the oscillator reaches a maximum; the absorptive term also becomes a maximum while the elastic term becomes zero. Another way of defining Q which uses the absorptive amplitude is

$$Q = \frac{f_0}{\Delta f_{FWHM}}. \tag{2.5}$$

This is important because the resonant frequency, f_0, can be measured along with the full width at half max., Δf, of the resonance curve, A_{ab} vs. f. Thus Q can be experimentally determined. Because

$$2\pi\Delta f_{FWHM} = \Gamma \tag{2.6}$$

(as determined from A_{ab} in Eq. (2.4)), Eq. (2.5) is sometimes written

$$Q = \omega_0 \tau . \tag{2.7}$$

This is useful to note because the Q can thus also be found by measuring the decay time, $\tau = 1/\Gamma$, of free oscillations. This is done in some experiments[Hunnekes, 1994]. For these experiments, however, the absorptive amplitude at resonance is constantly monitored. If Eq. (2.4), (2.5), (2.6), and the resonance condition are combined, one will find

$$A_{ab} = \frac{F_0}{M}\frac{Q}{\omega_0^2} \tag{2.8}$$

for the absorptive amplitude. Measuring A_{ab} and Q during a frequency sweep, i.e., from A_{ab} vs. f, then the constant, F_0/M can be found and Q can be monitored as A_{ab} changes.

The torsional oscillators have two "masses," the head and wing sections. This means that there will be two normal modes for each degree of freedom. There are two main degrees of freedom which result in two cantilever modes and two torsional modes. The torsional modes are the desired modes. The modes are distributed with a lower frequency cantilever mode at the lowest frequency and an upper frequency torsional mode at the highest as the following example from oscillator #5 suggests: 1273.2 Hz lower cantilever, 1625.1 Hz lower torsional, 5273.5 Hz upper cantilever, 85370.34 Hz upper torsional. The cantilever modes can be distinguished from the torsional modes by the sign of A_{ab}. A_{ab} is flipped for the cantilever modes (see Fig. 2.2a,b).

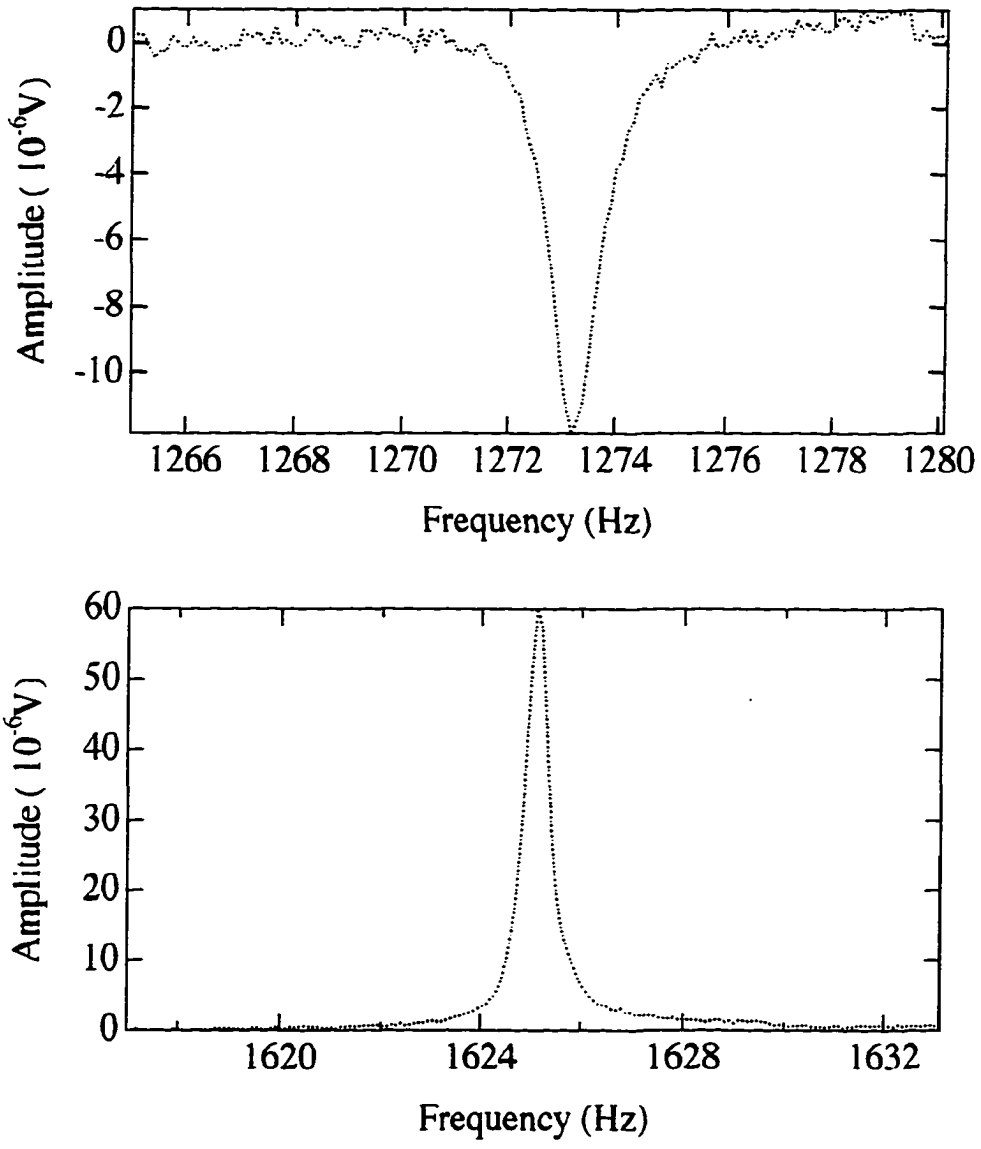

FIG. 2.2a. The top figure shows the lower cantilever mode while the bottom figure shows the lower torsional mode.

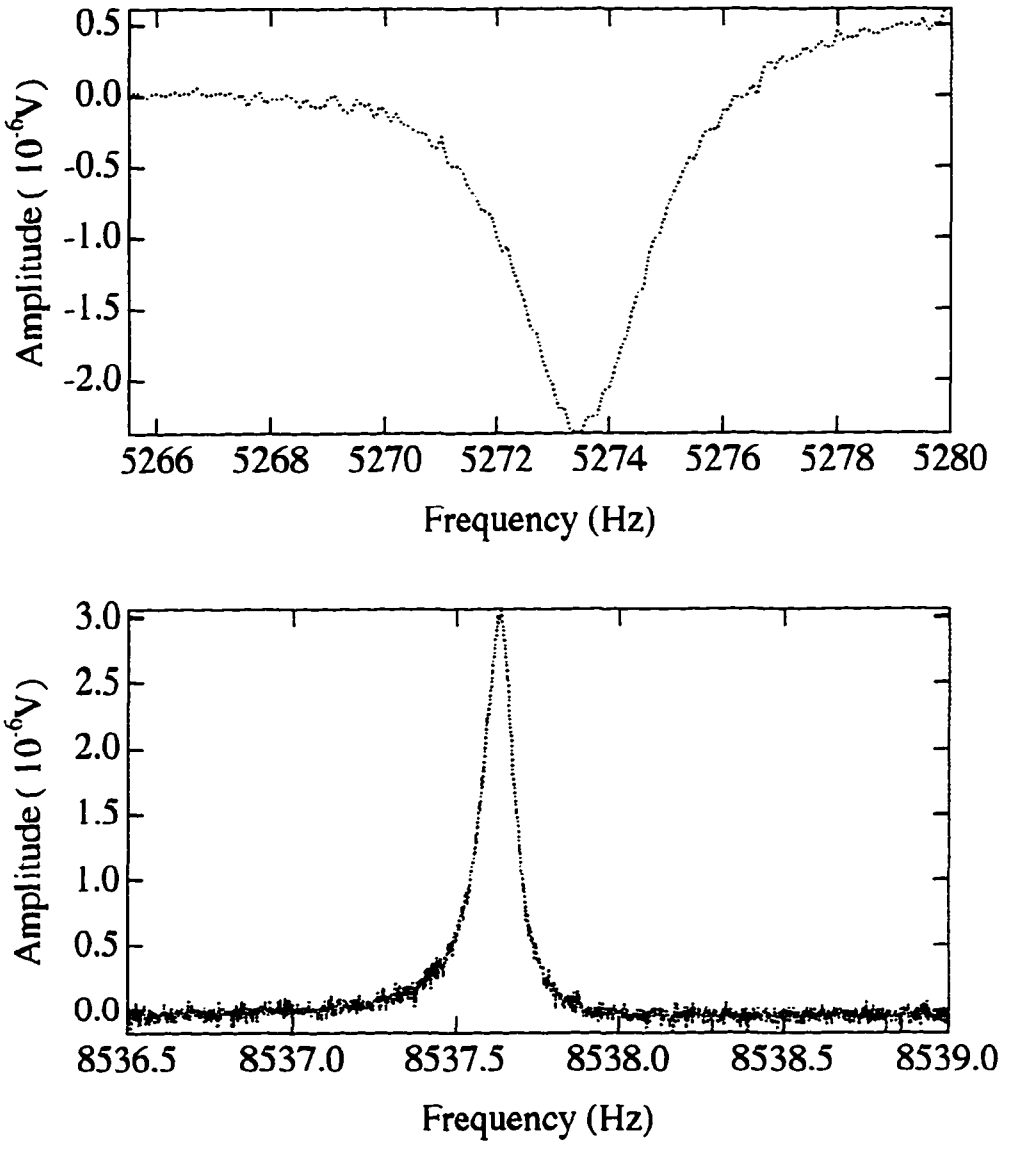

FIG. 2.2b. The top figure shows the upper cantilever mode while the bottom figure shows the upper torsional mode.

This asymmetry arises because, for the cantilever mode, the wing that receives the drive force moves in phase relative to the wing which produces the pick up signal.

For the torsional mode, the pick-up and drive wings are out of phase: when one moves closer to an electrode, the other one moves away (Fig 2.3a, b).

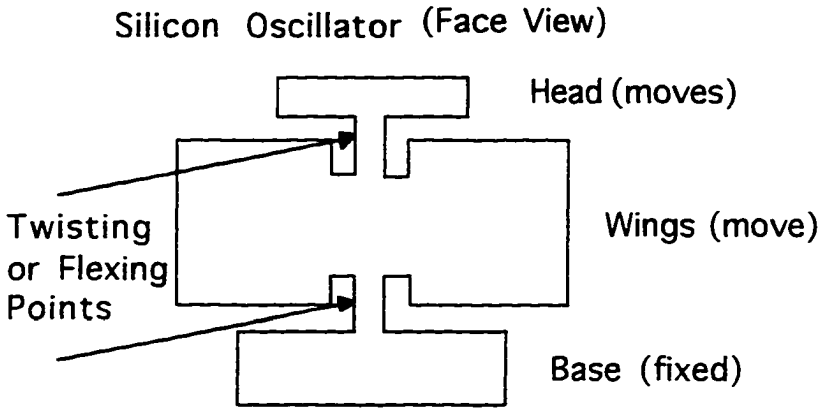

FIG. 2.3a. Face view of an oscillator. The head and wings are assumed to be rigid sections which move by twisting or flexing about the thin bars.

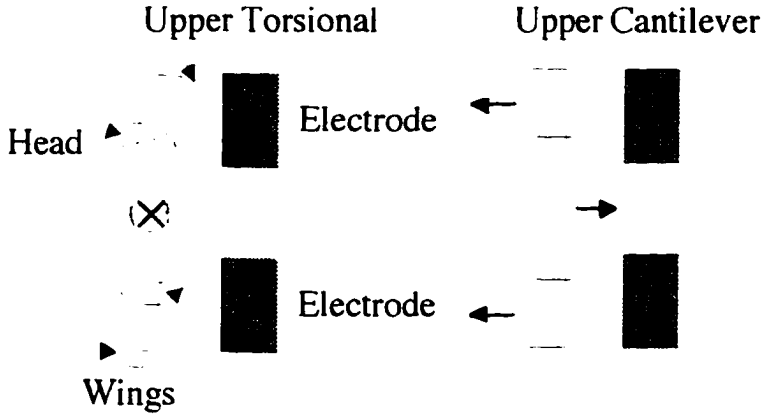

FIG. 2.3b. A top view of the head and wings of an oscillator. The rotational axis for the torsional mode is perpendicular to the page. The arrows indicate the relative motion of each part.

The room temperature Q's for the modes of oscillator #5 went as follows: 1157 lower cantilever, 2708 lower torsional, 2028 upper cantilever, 73 600 upper

torsional. The important thing here is that the upper torsional has by far the highest Q. Damping can be considered weak with such Q's.

Although the absorptive and elastic amplitudes are the superposition of the amplitude contributions from each resonance, this does not complicate matters. A good approximation for weak damping is to consider each resonance as if it arises from a one–dimensional driven oscillator. For widely separated resonances (further than $\omega_0 \pm 10\Gamma$), the absorptive amplitude from the other resonances will be negligible. The elastic amplitude for widely separated resonances is not always negligible, but for the torsional oscillators, the lower modes as compared to the upper torsional mode have low Q's and are thousands of Hz or many hundreds of Γ's from the upper torsional resonance. Thus, the A_{el} contributions from the lower modes are not significant—at least to within the noise, drift and offsets of the lock-in amplifier. The fall-off for A_{el} and A_{ab} can be seen from Eq. (2.4) as ω increases.

The lower and upper modes correspond to the symmetric and antisymmetric modes of oscillation. In the symmetric mode, the wings and head twist together, while for the antisymmetric mode, the angular momenta for the head and wings are equal and opposite. Note, the angular velocities are opposite but not equal for the anti-symmetric mode. As it turns out, the head has more of the energy in the anti-symmetric mode; thus, the maximum torsional angle and maximum angular velocity are larger than for the wing section. Because most losses occur at the epoxied base, the less the wings move, the lower the energy losses will be and hence, the higher the Q. This can be seen as follows. The total energy for the head (h) and wings (w) sections are

$$E_h = \frac{1}{2} I_h \left(\omega_h^{\max}\right)^2 \tag{2.9a}$$

$$E_w = \frac{1}{2} I_w \left(\omega_w^{\max}\right)^2. \tag{2.9b}$$

For the lower mode $(\omega_{max})_h$ may be substituted for $(\omega_{max})_w$. Thus

$$E_w = \frac{I_w}{I_h} E_h. \tag{2.10}$$

With I_w being much larger than I_h (~33 times), much of the motion is in the wings producing the lossy mode. The condition for the antisymmetric mode was

$$I_h \omega_h = -I_w \omega_w \tag{2.11}$$

With this condition and Eq. (2.9), the energy stored in the wing is smaller than that of the head,

$$E_h = \frac{I_w}{I_h} E_w. \tag{2.12}$$

So less motion of the wings will result in less energy loss through the base, leaving loss to come from the silicon neck; since the material is single crystal silicon, which is relatively defect free, losses will be low.

The Q may be improved further. These are just suggestions at this stage. As discussed in Chapter 3, the epoxy puts stress on the base, which has caused some oscillators to break at low temperatures even if the oscillators don't break, the stresses clearly must be inducing defects in the silicon. If some of the stress can be relieved by adding silicon to the epoxy, then silicon defect-induced losses at the base will decrease. Also, if the bottom torsional spring can be made longer and softer, the base will be further decoupled from the head's motion. One of the oscillators in the Series C set has been designed to test this hypothesis. Although

the actual oscillator has been made, it has not been tested yet (see Appendix A for current oscillator dimensions).

MINIMUM DETECTABLE FORCE

In reality the equation that describes a harmonic oscillator is

$$M\ddot{x}(t) + M\omega_0^2 x(t) + M\Gamma\dot{x}(t) = F_0 \cos\omega t + F_{fl} \tag{2.13}$$

where F_{fl} is a fluctuating force due to thermal fluctuations. These fluctuations put a limit on the minimum force that can be detected [Braginsky, 1977]. The form of the minimum force for a cantilever is

$$F_{\min} = \sqrt{\frac{4kk_B T\Delta\nu}{Q\omega_c}} \tag{2.14}$$

where ω_c is the resonance frequency of the oscillator, k_B is Boltzmann's constant, T is the temperature, k is the oscillator spring constant, and $\Delta\upsilon$ is the noise bandwidth [Sidles, 1992; Durig, 1992]. This can be applied to a torsional oscillator for a force that is applied out along the head at a distance, l. The torsional constant can be simply related to the spring constant through l, i.e.,

$$k = \frac{\kappa}{l^2}. \tag{2.15}$$

With Eqs. (2.14) and (2.15), $F_{min}/\sqrt{Hz}$ in SI units becomes

$$\frac{F_{\min}}{\sqrt{Hz}} = \sqrt{\frac{4k_B T\sqrt{\kappa I}}{Ql^2}} \tag{2.16}$$

or

$$\frac{F_{\min}}{\sqrt{Hz}} = 7.43\times10^{-12}\sqrt{\frac{T\sqrt{\eta I}}{Q}}\left(N/\sqrt{Hz}\right) \tag{2.17}$$

where $\sqrt{\eta} = l^{-2}\sqrt{\kappa}$ and where ω_c has been replaced by $\sqrt{\kappa/I}$. Clearly the higher the Q, the better the force sensitivity. Similarly, by reducing the temperature, F_{min} decreases. For example, a Series B big oscillator has a $F_{\min}/\sqrt{Hz}$ of 3.4×10^{-13}

$N/\sqrt{Hz}$ at room temperature while at 100 K this drops to 6.8×10^{-14} $N/\sqrt{Hz}$. For a 4000 Å thick 45 μm tall nitride oscillator, $F_{min}/\sqrt{Hz}$ is 0.31 $fN/\sqrt{Hz}$ at 295 K but only 3.6 $aN/\sqrt{Hz}$ at 4 K! The noise bandwidth can be determined from the lock-in amplifier time constant.

In reality, however, the minimum force of the oscillator will probably be set by the temperature stability and external vibrations. When operating at low drive voltages, loud talking in the room can disturb the oscillator even though it is in the Dewar! The disturbances are seen as jumps in the lock-in. To avoid thermal vibration other than those caused by noisy people, suspension of the Dewar may be required, but if higher frequency oscillators are used in the future, this might be avoided. Temperature stability of 0.01 K is not easy to achieve with the current probe. If an equi-temporal shield can be put around the oscillator stage, this might help—i.e., a copper can. But with space already tight, this will be a stretch. Nevertheless, because most of the runs are temperature sweeps, temperature stability is a secondary issue. Just make sure that the sweeps are slow enough to get temperature accuracy—no hysteresis.

CAPACITIVE DETECTION

The oscillator is driven by making it one plate in a capacitive gap and then using an electrode (the other plate of the capacitor) to apply a sinusoidal voltage. The motion of the oscillator is detected by another electrode, which picks up a small sinusoidal voltage induced by trapped charge, that moves with the oscillator. The trapped charge is placed on the oscillator by biasing the face at a high voltage. As a general reference, Fig. 2.4 gives a block diagram view while

2.5 (a) shows all components, including internal (in the probe) coax capacitance, c_b, and external coax capacitance, c_a; these values have not all been measured to date.

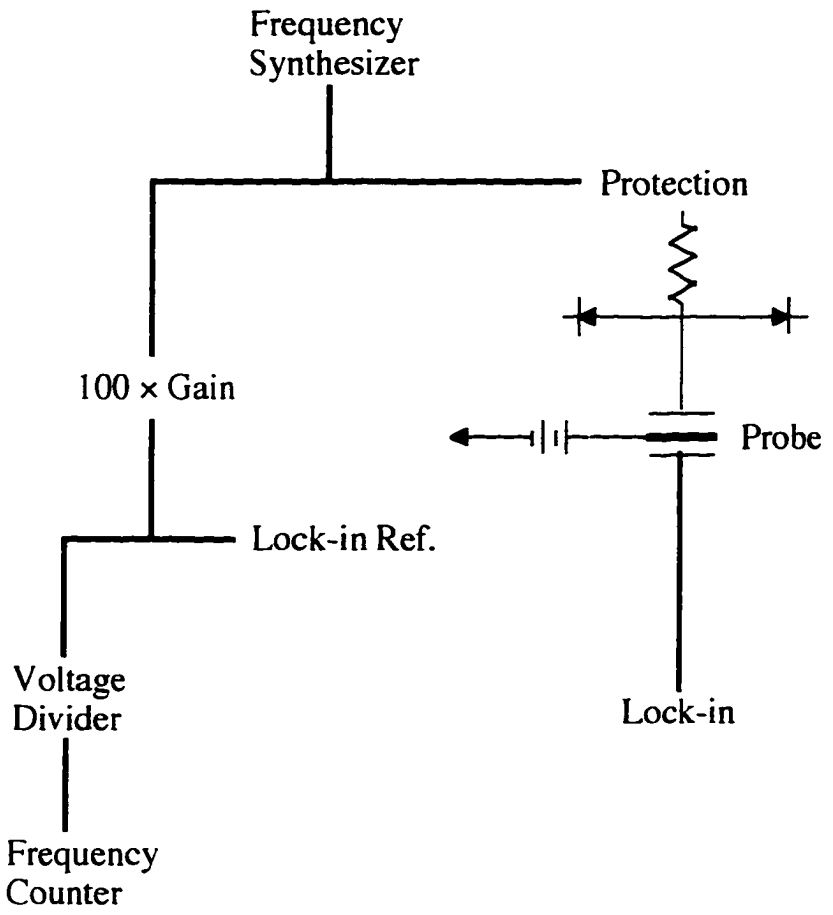

FIG. 2.4. Simple flow overview of the electronics.

The probe coax cable is ~200 pF, i.e., c_b. This value of c_b was for RG 174 coax; the ultra miniature C1 coax has a capacitance per length of 47 pF/ft. The ultra miniature coax needs to be replaced with ultra low noise coax up to the stage where space-saving miniature coax can then be soldered on. The gap capacitance

is 1.8 pF for a 0.16 mm gap. Now that the lab has a capacitance meter, these are easily measurable. The 10 kΩ resistor, *1, is part of the protection and should limit any current spikes. The rest of the protection is below *2; this includes the fast switching 1N 914B diodes and the 5 V biases that keep them away from the "conducting state" under normal probe operation; however, these will clip driving voltages over 5 V if this part of the circuit is left in. The diodes also have a capacitance, which unfortunately sinks signal; this is 5 pF for each of the 10 or 12 diodes in each protection circuit. The bias resistor is probably not needed; it was put in to keep charge on the oscillator so the signal doesn't disappear down the high voltage line. If it is needed, it would be best to replace the resistor with a diode, inductive load, and switch in parallel for keeping charge on and taking charge off the oscillator.

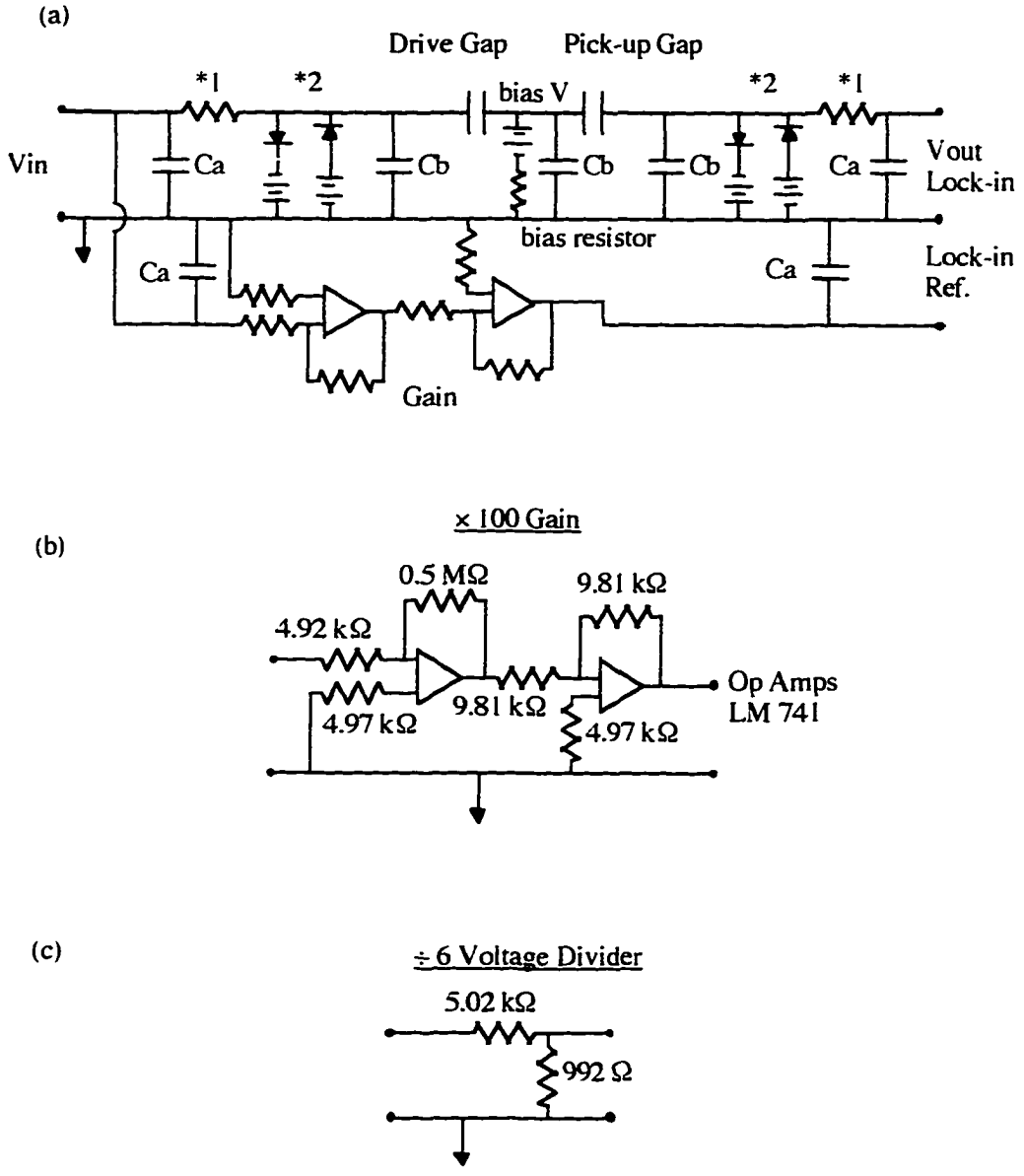

FIG. 2.5. (a) shows the over all circuit. (b) shows the component values of the gain sub-section in 2.5(a). Similarly (c) shows the voltage divider values.

The voltage divider is not shown in Fig. 2.5 (a) but in Fig. 2.5 (c) along with the 100 × signal gain (Fig. 2.5 (b))—the lock-in needs a minimum 100 mV input for the reference, so for sub 0.1 V drives, the reference signal must be boosted . The voltage divider before the frequency counter is necessary because the counter can only intake a maximum signal of 5 V_{rms}.

The trapped charge on the moving oscillator induces a voltage signal in the pick-up electrode across the capacitive gap. By biasing the oscillator, the sensitivity of the detection can be greatly enhanced. The force between the capacitor plates is

$$F = \frac{1}{4\pi\varepsilon_0}\frac{AV^2}{2d_0^2} \tag{2.18}$$

where ε_0 is the permeability of free space, d_0 is the gap spacing, V is the voltage and A is the plate area. If V is merely a 1 or sub-1 volt drive voltage, then this force would be small, the charge on the oscillator would be minimal, and little detection would be possible. However, by biasing the oscillator at a high voltage, a substantial amount of charge can be put on the "plates" of the capacitor. The drive voltage then applies a force

$$F \propto V_{bias}^2 + 2V_{bias}V_0e^{i\omega t} + \left(V_0e^{i\omega t}\right)^2 \tag{2.19}$$

where $V_0e^{i\omega t}$ is the drive voltage. Neglecting second–order terms as $V_{bias} > V_0$, the force is proportional to $V_{bias}V_0$. For this reason the oscillator is biased. Note also that the force is at frequency ω with bias, as opposed to frequency 2ω without it. The oscillator bias, however, cannot be set arbitrarily large. When the bias exceeds 270 V with ~100 mTorr of He exchange gas, the electrodes will arc across the gap; this causes the over–load light to flash on the lock-in. Most runs

should be carried out at 250 V. Helium is not a forgiving gas, it does not have many internal degrees of freedom to absorb energy in collisions; therefore, it tends to propagate break downs. Arcing is bad not only because it can damage equipment, but it can change the phase shift between the reference and input. After some time, the phase shift may return, but this does not help when one is in the middle of an experiment (see next section for more on the phase shift).

The detected signal, minus losses resulting from parasitic capacitance, corresponds to some amplitude of the oscillator. The amplitude of the oscillator is an important experimental quantity, so it must be determined. This can be accomplished by first looking at a simplified version of Fig. 2.5, which is shown in Fig. 2.6.

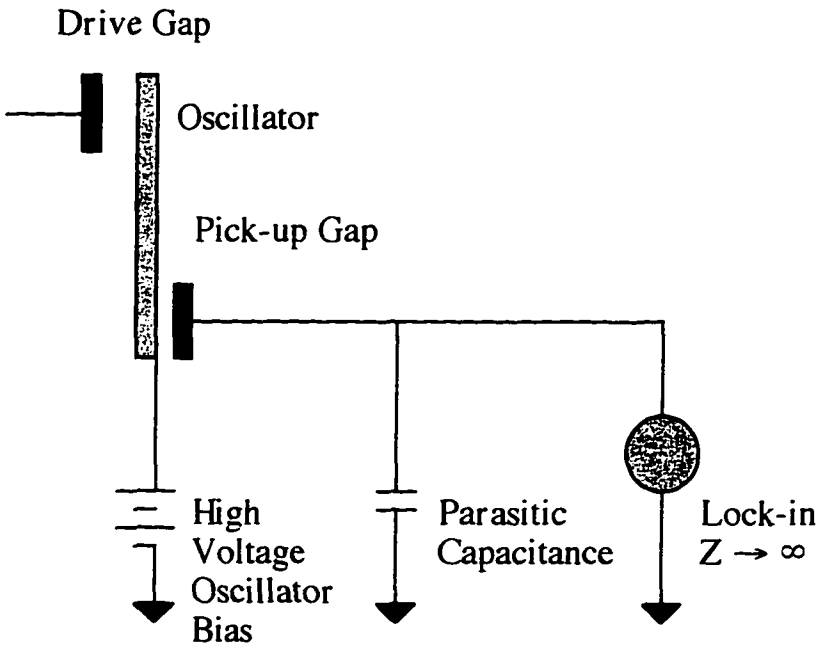

FIG. 2.6. Simple paradigm for circuit in Fig. 2.5 used to determine the amplitude of oscillation.

The area of an electrode is $\pi r^2 = 3.17 \times 10^{-5}$ m^2. Approximating the gap as a simple parallel–plate capacitor gives

$$C_{gap} = \frac{A\varepsilon_0}{d_0}. \tag{2.20}$$

For a 0.25 mm gap, this is 1.1 pF. The capacitance added by the fringe field is negligible, which can be ascertained by looking at the capacitance for two disks of radius, r [Gray, 1972]:

$$C_{disks} = \varepsilon_0 \left\{ \frac{\pi r^2}{d} + r\left[\ln\left(\frac{16\pi r}{d} - 1 \right) \right] \right\}.$$

If the oscillator is not epoxied well, it may set with a tilt so the plates are not parallel. In this case Eq. (2.20) is not quite accurate, either an average distance

will have to be used for d_0 or a more accurate formula will have to be worked out. On the other hand, C_{gap} can now be directly measured with the new Fluke 76 multi-meter, so working out C_{gap} may be a moot point. Because the lock-in has a large input impedance, one can write

$$\frac{dQ}{dt} = 0. \tag{2.21}$$

Alternatively this can be written

$$\frac{d(CV)}{dt} = 0 \tag{2.22}$$

where C is the total capacitance, $C = C_{gap} + C_{parasitic}$, and V is the total voltage, $V_{bias} + \delta V e^{i\omega t}$. The last term in the sum is the pick-up voltage. The gap spacing will also vary in time as a result of the oscillation, so $d = d_0 + \delta d e^{i\omega t}$. Differentiating Eq. (2.22),

$$V\frac{\partial C}{\partial d}\frac{dd}{dt} + C\frac{dV}{dt} = 0, \tag{2.23}$$

and dropping 2nd order terms,

$$-C(i\omega)\delta V e^{i\omega t} = \frac{-A\varepsilon}{d_0}\frac{V_{bias}}{d_0}\delta d(i\omega)e^{i\omega t}, \tag{2.24}$$

one can solve for δd, the amplitude of the oscillator,

$$\delta d = \frac{\delta V}{V_{bias}} d_0 \frac{C_{gap} + C_{paracitic}}{C_{gap}}. \tag{2.25}$$

For example, at the peak of dissipation, the amplitude of the detected signal is 1.90 μV. Given a gap of 0.16 mm, a bias of 260 V, a diode plus cable capacitance of 265 pF, and a gap capacitance of 1.8 pF; δd = 1.73 Å. Because the actual motion is a twisting where the edge moves closer to the electrode than the center, this value is taken to be an average value; thus, the center of the wing where the

detection occurs is taken to move this amount. The angular amplitude of the head is larger.

$$\theta_w^{\max} = \theta_h^{\max} \frac{I_h}{I_w} \tag{2.26}$$

The distance at which the sample sits is less than the midpoint of the wings by a factor of 3/5, so the amplitude of the head must be scaled down by 3/5. The sample is usually placed as far out along the head as possible. With the above arguments, the estimated amplitude that a sample sitting on the head goes through is

$$\begin{aligned} \delta d &= 1.73\,\text{Å} \times \frac{3}{5} \times \frac{32}{1} \\ \delta d &= 34\,\text{Å} \end{aligned} \tag{2.27}$$

(remember the ratio of I_h:I_w is 1:32).

The amplitude of oscillation may be checked another way (see Fig. 2.7). Similar to Eq. (2.2), the oscillator may be modeled,

$$\ddot{x}_b = -\frac{k_b}{m}(x_b - x_a) - \Gamma_b \dot{x}_b \tag{2.28a}$$

$$\ddot{x}_a = -\frac{k_a}{M}(x_a) + \frac{k_b}{M}(x_b - x_a) + \frac{F_0}{M}\cos\omega t - \Gamma_a \dot{x}_a. \tag{2.28b}$$

With

$$\begin{aligned} x_a &= Ae^{i\omega t} \\ x_b &= Be^{i\omega t} \end{aligned} \tag{2.29}$$

as solutions, the constants A and B have been solved for although the solutions are far too tedious to include. They appear in other lab documentation. The trick here is to use the measured Q's to determine Γ_a and Γ_b. The first and obvious choice is to use the lower Q to determines Γ_a and the upper Q to determine Γ_b.

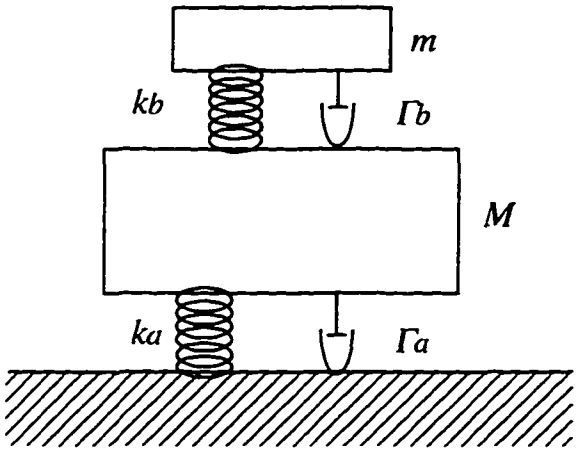

FIG. 2.7. The oscillator as two coupled masses with springs. Γ_b is from losses in the silicon while Γ_a is from losses in the base.

It should be noted that for all studies in this work, a constant driving force was used to study the Q. It is also possible to keep a constant drive amplitude, which requires an extra feed back loop to change the drive and bias voltage, thus keeping the amplitude fixed. The dissipation is then correlated to the drive or bias voltage. Note, the drive needs to be used in addition to the bias because the bias is ultimately limited by the arcing voltage.

FREQUENCY SWEEPS

In order to find the resonance and calibrate to a Q, a program that maps out the elastic and absorptive amplitude as a function of frequency was written in LabView (see Appendix B).

When using the program to sweep, even if the time interval is set to zero, the program will still only make ~two measurements per second—the handshaking between instruments is slow. As slow as this is, it is possible to

sweep too fast, producing oscillations in the peaks—beats (see Fig. 2.8). The frequency step must be sufficiently small to avoid this. For a 0.1 Hz–wide peak, probably 0.002 Hz steps with a 500 ms interval would work.

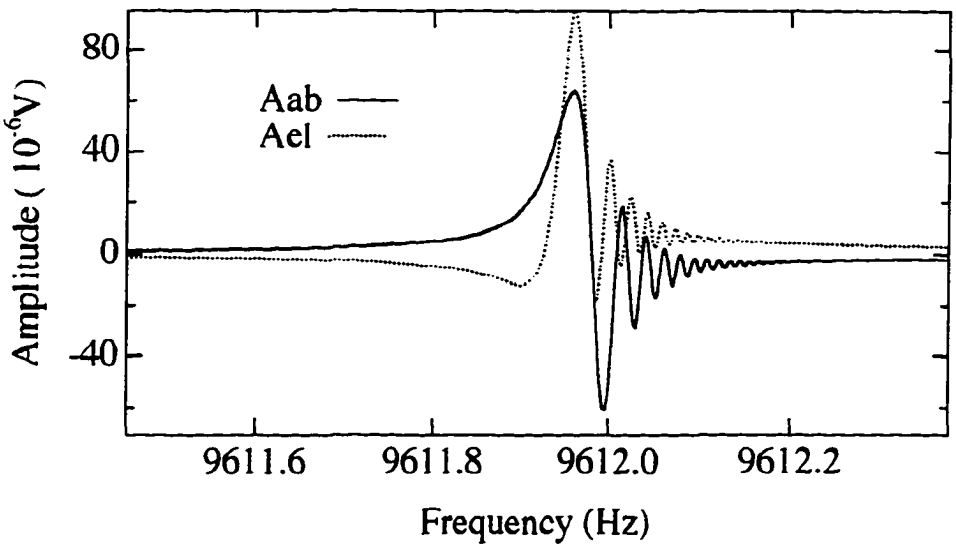

FIG. 2.8. Example of beats resulting from sweeping too quickly.

On the other hand, sweeping this slow to locate a resonance would take weeks. Clearly for such cases a larger step, 0.02 Hz with no time interval, is more appropriate. With experience it is often quicker to spend the half-hour to find a resonance manually. One can actually do this much faster if the oscillators are from the same wafer and one of the resonances is already known. No upper resonance for a Series B oscillator has ever been below 8000 Hz or above 9700 Hz. Steps as large as one Hertz can be taken manually; just look for the quiver of the lock-in needle i.e., the small beat oscillations. It is VERY subtle but distinct.

Another abnormal characteristic of sweep data is an asymmetric absorptive amplitude (see Fig. 2.9). This is caused by a phase difference between the reference and measured signal. The phase difference is between 15° and 20°. It may be partly caused by the protection circuit. The 10 kΩ protection resistor in parallel with the ~265 pF of coax and diode parasitic capacitance would be expected to cause a shift of $\phi = \tan^{-1}(\omega RC) = 8.5°$. Because the two protection circuits are in series, this would give a total of 17°, which is in the correct range. Regardless of the cause, the shift may be corrected for. With no phase shift entered into the lock-in, it would measure some amplitudes A_m and B_m,,

$$x = A_m \sin\omega t + B_m \cos\omega t. \tag{2.30}$$

However, the circuit introduces a shift which is hidden in A_m and B_m. What is measured could be written as

$$x = A_0 \sin(\omega t + \phi) + B_0 \cos(\omega t + \phi) \tag{2.31}$$

where A_0 and B_0 are the desired amplitudes without the phase shift. Expanding Eq. (2.31) and comparing to Eq. (2.30) one finds

$$A_m = (A_0 \cos\phi - B_0 \sin\phi) \tag{2.32a}$$

$$B_m = (A_0 \sin\phi + B_0 \cos\phi). \tag{2.32b}$$

One can solve Eqs. (2.32a) and (2.32b) at resonance ($B_0 = 0$; not $B_m = 0$) to find the phase shift introduced by the electronics,

$$\phi = \arctan\left(\frac{B_m}{A_m}\right). \tag{2.33}$$

Of course one must find the resonance frequency by graphing the total amplitude, $A = A_{el}^2 + A_{ab}^2$. Thus, if a shift of ϕ is found, a $(-\phi)$ must be sent to the lock-in to cancel the unplanned shift.

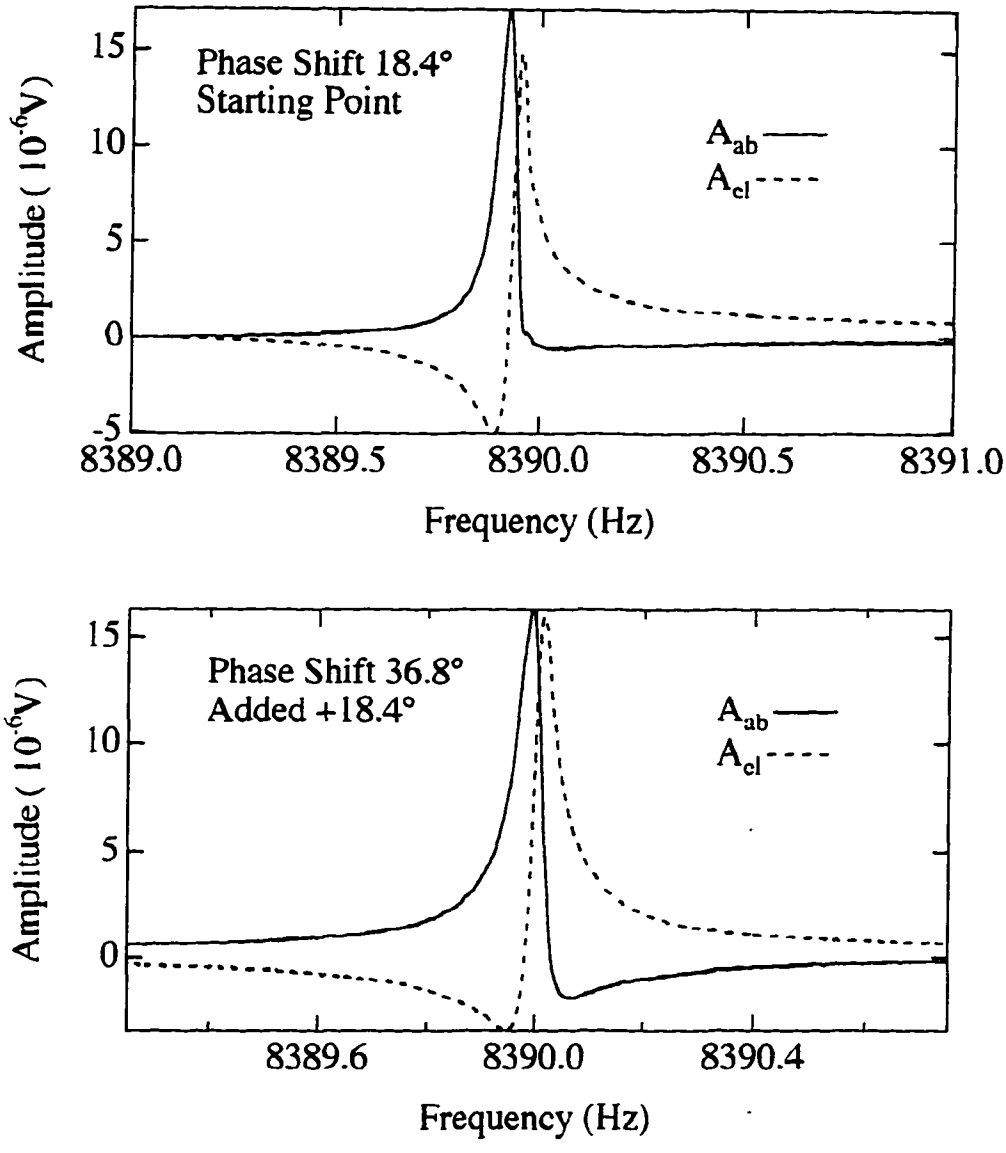

FIG. 2.9. See next page.

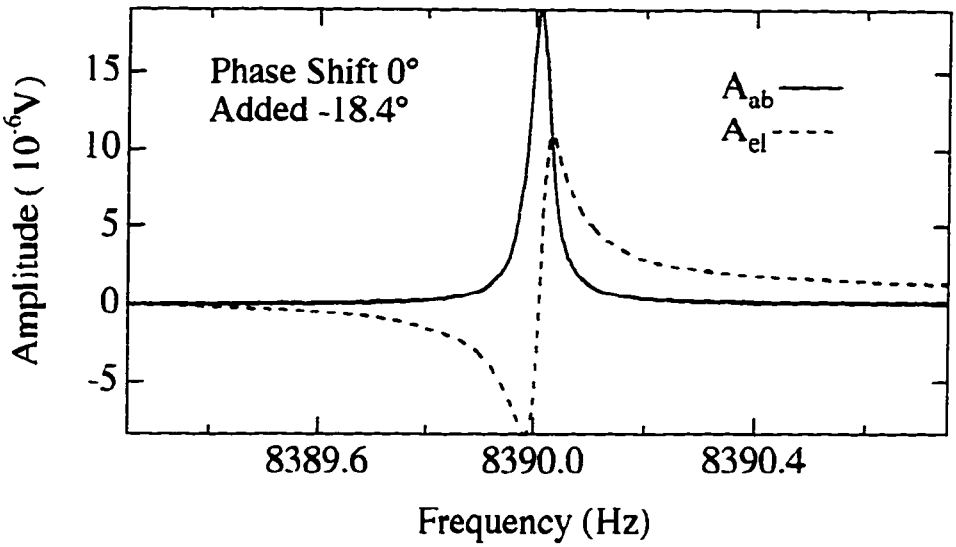

FIG. 2.9. The first graph shows the splitting of the amplitude into its two components where no phase correction was sent to the lock-in. The second graph shows the effect of adding the wrong correction of equal magnitude, while the last graph shows the effect of cancelling the phase shift by adding the correct phase correction.

Chapter 3: The Experimental Method

Polonius: "Though this be madness, yet there is method in't."

William Shakespeare. Hamlet.

INTRODUCTION.

The double torsional oscillator technique was developed at Cornell [Kleiman, 1985], brought to the University of Texas by John Markert, and implemented by the author. This chapter describes many of the associated issues and methods for setting up a torsional oscillator system. Hopefully, it will provide sufficient guidance to the wandering minstrel to keep the oscillator tradition alive. Besides the descriptions and explanations of various experimental parts and techniques that worked, some recommendations are made within to correct (or try to correct) for problems that occur in the experiment. Under no circumstance should any technique be considered as the "gospel truth," these are not necessarily the best or only way of doing things. Not all the descriptions enclosed are complete, some items or steps are left out for the readers imagination

and intuition. Remember, there is no substitute for common sense, so use it! Also don't be afraid to try out new ideas. With this said, we can begin.

DESIGN

The mass and spring constant are analogous to the inertia and torsional spring constant, so for many of the calculations it is more comfortable to write or think of the equations in terms of m's and k's rather than I's and κ's. The oscillators are designed by considering the oscillator as two coupled masses joined in series to an infinitely massive base by a spring. Three main design constraints must be juggled when determining the dimensions: size (so they fit in the respective experiments), frequency (above ten kHz for lower noise and better response time; also, studies of the frequency dependence of dissipation in the vortex lattice could be made if several different frequency oscillators were made), and sensitivity (so small forces can be detected; this is dependent on a high Q). For the large oscillators, the width and length are the main variables; the thickness, 15–20 mils, is set by the thickness of the purchased wafer. For the NMR oscillators, more control over the thickness exists, by controlling the film thickness or implant depth.

Before calculating the resonant frequency, minimum detectable force, etc., one must find the torsional spring constant, κ. The torsional constant for a bar of rectangular cross section is given by [Timoshenko, 1970] as

$$\kappa = \frac{GU_1 x_3^3}{U_2}\frac{1}{3}\left(1 - \frac{192}{n^5}\frac{x_3}{U_1}\sum_{n=0}^{\infty}\frac{1}{(2n+1)}\tanh\left((2n+1)\pi\frac{U_1}{2x_3}\right)\right) \qquad (3.1)$$

where G is the shear modulus and all other variables are the oscillator dimensions drawn in Fig. 3.1. However, this may be simplified since

$$\sum_{n=0}^{\infty}\frac{1}{(2n+1)}\tanh\left((2n+1)\pi\frac{U_1}{2x_3}\right)\approx 1-\frac{1}{12}\left(\frac{x_3}{U_1}\right)^4. \tag{3.2}$$

This approximation is accurate to 4% [Young, 1989]. By making a substitution, Eq. 3.1 reduces to

$$\kappa=\frac{GU_1x_3^3}{U_2}\left[\frac{1}{3}-0.209\frac{x_3}{U_1}\left(1-\frac{1}{12}\left(\frac{x_3}{U_1}\right)^4\right)\right]. \tag{3.3}$$

The shear modulus is a measure of the rigidity of the material under shearing forces. For silicon, $G = 6.63 \times 10^{10}$ Pa and for silicon nitride $G = (0.86–1.16) \times 10^{11}$ Pa. Note, 1 Pa = 10 dynes/cm^2.

Next, the inertia of the head and wings needs to be determined. Now

$$I=\int r^2dm, \tag{3.4}$$

as can be found in any freshman physics text [Halliday & Resnick, 1978]; thus performing the integral, the inertia of the head becomes

$$I_{head}=\frac{\rho}{12}H_1^3H_2x_3\left[1+\left(\frac{H_2}{H_1}\right)^2+\left(\frac{H_3}{H_1}\right)^2\right] \tag{3.5}$$

while the integral of the wings becomes

$$I_{wing}=\frac{2}{3}\rho w_2x_3\left(a_2^3\left[1+\frac{1}{4}\left(\frac{W_2}{a_2}\right)^2+\frac{1}{4}\left(\frac{x_3}{a_2}\right)^2\right]-a_1^3\left[1+\frac{1}{4}\left(\frac{W_2}{a_1}\right)^2+\frac{1}{4}\left(\frac{x_3}{a_1}\right)^2\right]\right) \tag{3.6}$$

The density, ρ, of silicon is 2.3289 g/cm^3 while for nitride the value is much higher, (2.77–3.22) g/cm^3—these are both at 25°C. Armed with the inertias and torsional constants for the oscillator, it is then possible to calculate the frequency for the antisymmetric torsional mode. Because the mode frequencies of the undriven system are approximately the resonant frequencies of the driven system,

we can write Newton's equations for each "mass" of the oscillator, i.e., the head and wings:

$$m_h\ddot{x}_h + k_h(x_h - x_w) = 0 \tag{3.7}$$

$$m_w\ddot{x}_w + k_w x_w - k_h(x_h - x_w) = 0. \tag{3.8}$$

Putting in the standard "best guess" solution, $x_h = A_h e^{j\omega t}$ and $x_w = A_w e^{j\omega t}$, one can solve the set of algebraic equations by taking the determinant and solving for ω^2.

$$\begin{vmatrix} k_h - \omega^2 m_h & -k_h \\ -k_h & k_w + k_h - \omega^2 m_w \end{vmatrix} = 0 \tag{3.9}$$

Thus ω^2 becomes

$$\omega_{\pm}^2 = \frac{1}{2m_h m_w}\left\{ m_h(k_h + k_w) + m_w k_h \pm \sqrt{\left[m_h(k_h + k_w) + m_w k_h\right]^2 - 4m_h m_w k_h k_w} \right\} \tag{3.10}$$

where the ± refer to upper and lower torsional modes. Note that in calculating these equations, rectangular cross sections were used. In reality, the cross sections are trapezoids because of the 54.7° of intersection between the etch stopping (111) planes and the masked (100) plane; thus, the backside of the oscillator is wider than the topside. This causes the inertias to be slightly larger and torsional springs slightly stiffer. An approximation could be made by taking the average of the top surface dimensions and bottom surface dimensions.

To calculate values for the inertias, spring constants, and frequencies of variously dimensioned oscillators, an Excel spread sheet has been made. For the Series B or C oscillators (those are for the stationary and rotatable probes, respectively, both are macroscopic, ~cms), the file is called *SERIES c (i's and k's)* and can be found under path *xander:osc design:series c*. This sheet contains the dimensions, given in cms, as described by Fig 3.1.

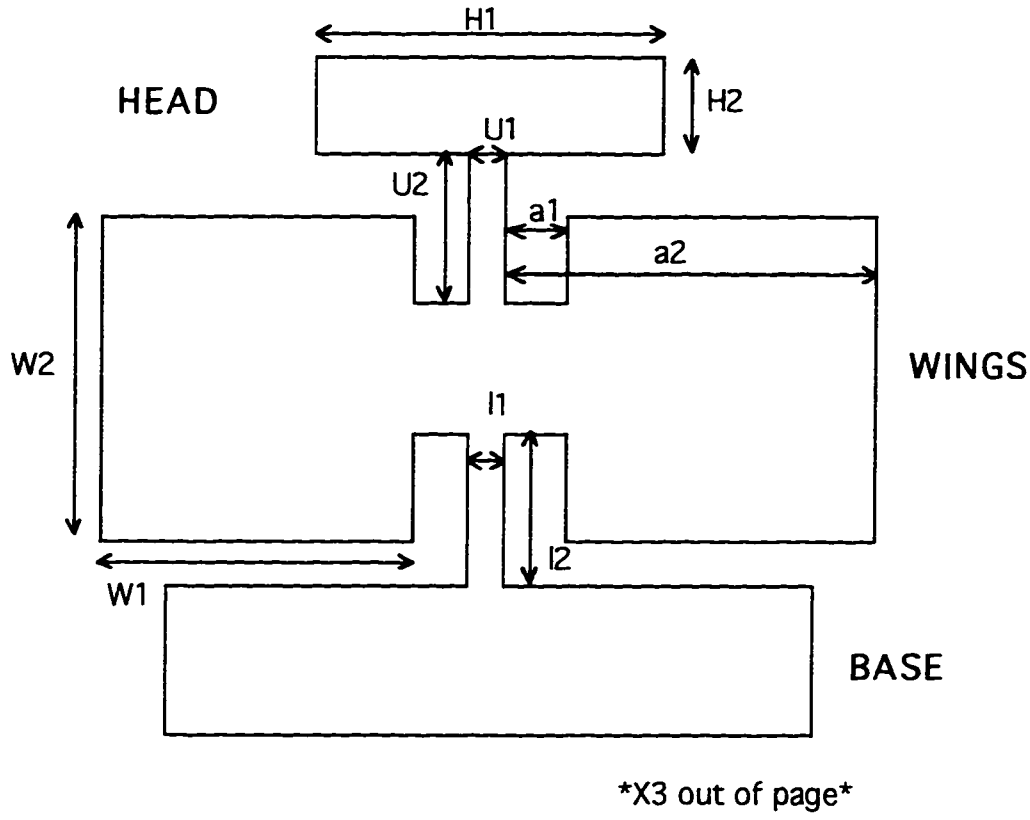

FIG. 3.1. Design parameters for an oscillator.

From these dimensions, *I's* and κ*'s* in g·cm^2 and dynes·cm are calculated respectively. The calculated *I's* are then copied and pasted into a file called *series c i1/i2*, which calculates the frequencies from the above formulas. A rebuilt stronger, faster spread sheet (made for less than six million dollars) for the NMR oscillators can be found in the *nmr2* folder called *NMR2/variable Dim. Mat...* This sheet can be used for the large oscillators also. The inputed dimensions are assumed to be in μm. Only the dimensions and constants such as the density of the material, modulus, etc., need to be changed in this sheet; the rest is automatic.

This spread sheet also finds a quantity called *eta* used in finding the minimum force at some length along the head, 50 or 75 μm. Note, *eta* would have to be changed if the sheet were used for the big oscillators. NEVER make changes and save over the original spreads sheets. To give a rough idea of the order of magnitude of sizes, frequencies and minimum forces, a table is provided below:

	Series B	**Series C**	**NMR (4000 Å)**
Head			
H_1	0.8 cm	0.6 cm	150 μm
H_2	0.25 cm	0.08 cm	25 μm
I_h	1.04×10^{-3} g·cm^2	1.3×10^{-4} g·cm^2	6.7×10^{-21} kg·m^2
Wings			
W_1	0.8 cm	0.4 cm	150 μm
W_2	0.85 cm	0.425 cm	100 μm
I_w	3.40×10^{-2} g·cm^2	1.78×10^{-3} g·cm^2	3.8×10^{-21} kg·m^2
Torsional Spring			
U_1	0.12 cm	0.08 cm	14 μm
U_2	0.3 cm	0.14cm	30 μm
κ	3.9×10^6 dyne·cm	4.9×10^6 dyne·cm	1.1×10^{-9} N·m
Frequency	13.8 kHz	32.0 kHz	71 kHz
F_{min} **(@ 300 K)**	3.4×10^{-13} N	6.0×10^{-14} N	2.8×10^{-16} N

Table 3.1. Oscillator dimensions. (Also see appendix A).

The actual resonance frequencies of the large oscillators has always been found to be lower than the theoretical values. This may be due to the larger inertias from the rectangular cross sections mentioned above. On average, the actual values hover around 9000 Hz. The actual frequencies of the nitride NMR oscillators have yet to be determined. The NMR resonant frequencies may actually be higher from rounding of the edges of the head and wings. Because the lock in amplifier has a limit of 100 kHz, the NMR oscillators should be targeted to have frequencies around the mid-tens of kHz.

OSCILLATOR PROCESSING

Once the design specifications, i.e., head, wing, upper and lower spring dimensions, have been determined, a new generation of oscillators is ready to go into production. The techniques used for making oscillators are the same techniques that are used in the semiconductor industry to make integrated circuits. Various steps involving lithography, deposition, etch, implantation, or diffusion can be used in different combinations to micromachine the desired structure [Kaminsky, 1985]; details for these processes can be found in many textbooks such as the classic: VLSI Fabrication Principles by Sorab K. Ghandi. Many of the supplies can be found in Semiconductor International's Technical Product Reference Source. Fig. 3.2 shows the outline of the silicon NMR process.

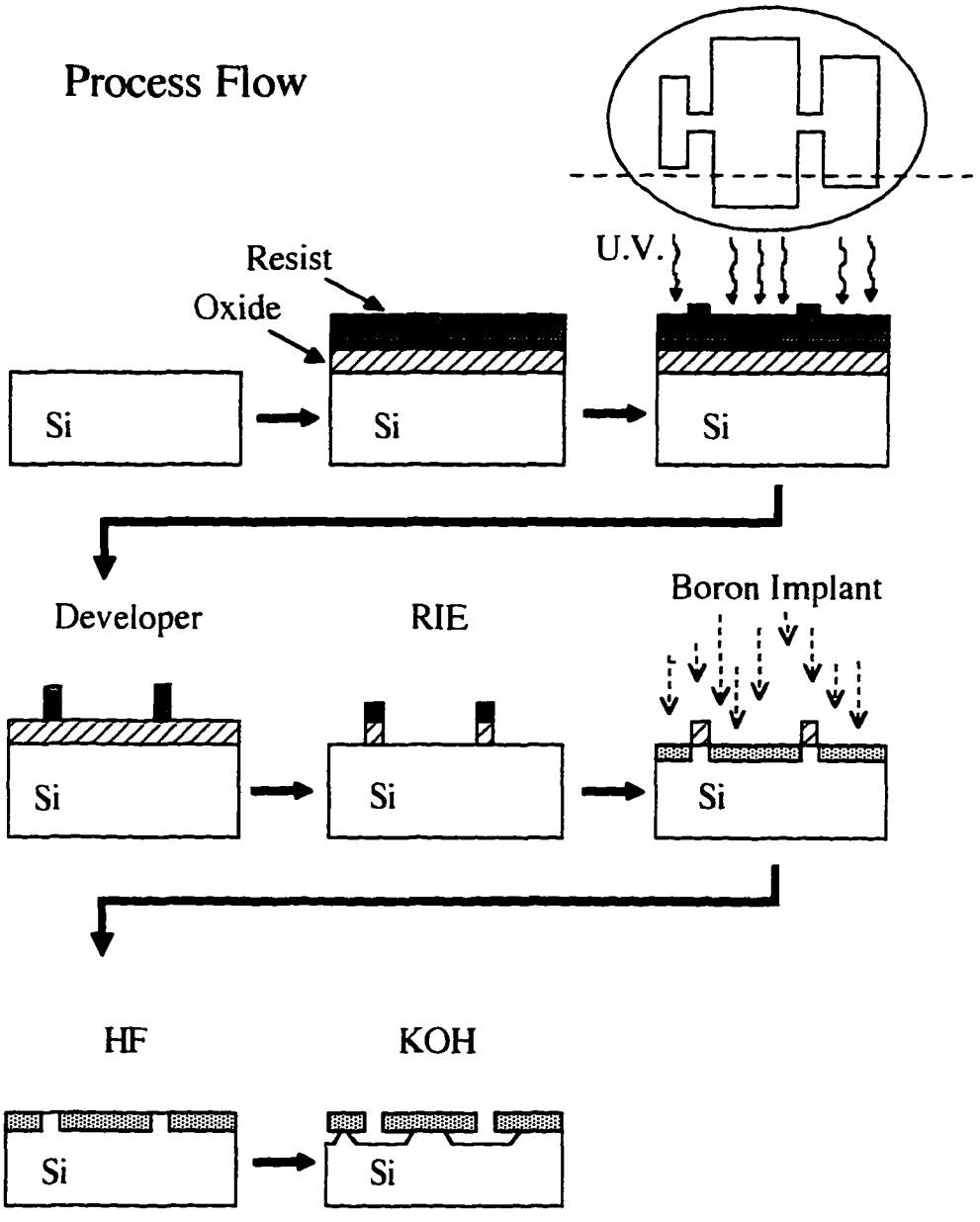

FIG. 3.2. Example of a Process Flow for Si NMR Oscillator.

Mask Lithography

One can begin with a very archaic but cheap method to produce a first generation mask. Note, a mask is a hard template with the desired pattern through which the entire wafer is exposed as opposed to a reticle which is a template of only one chip through which the wafer is exposed several times as the pattern is stepped across the entire wafer. These processes use masks. Physically, the mask is simply a green glass plate with a thin patterned layer of 1000 Å of chrome or 2000 Å of iron oxide that blocks UV light in regions covered by the pattern. First, a positive image of the oscillators should be drawn with Power Draw or some other CAD program (Fig. 3.3).

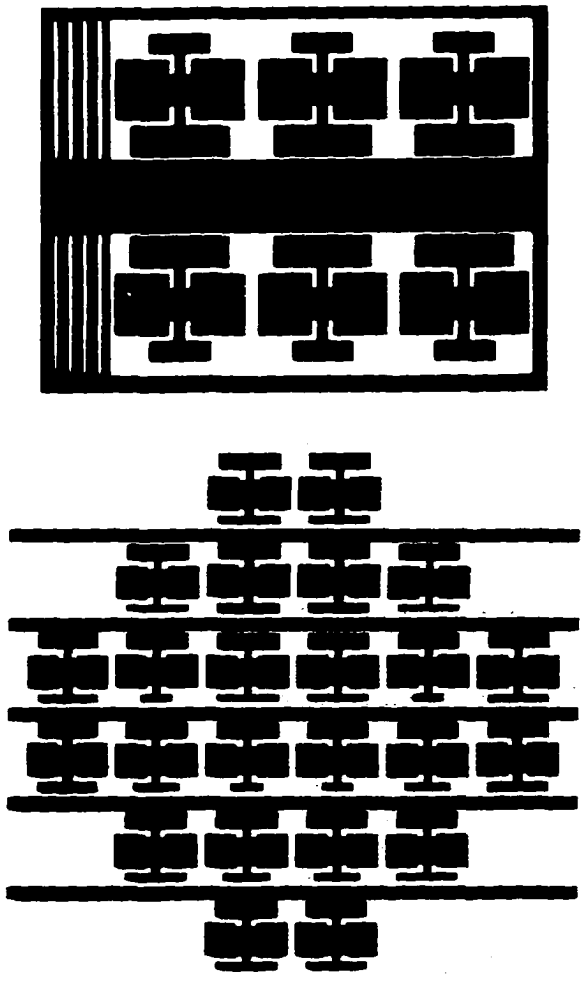

FIG. 3.3. See next page.

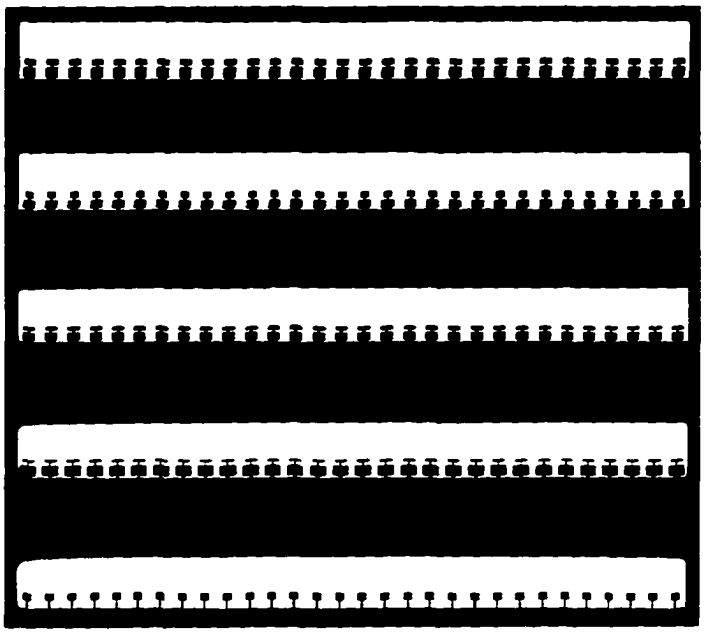

FIG. 3.3. Top figure shows the Series B oscillators with alignment bars on the left. The middle figure shows the Series C oscillators while the bottom figure shows the Si NMR oscillators—the bottom row of the NMR oscillators are actually cantilever paddles and not tortional oscillators.

The drawing should not be to scale, but rather a ten-times enlargement; this reduces error produced by limitations of the printer's resolution, and the drawing can easily be photographed down to the correct size. A positive image must be drawn—the oscillators being a solid black tone—as almost all photoresists used at the MERC are positive resists. This means that where light can go through the mask, the photoresist will be broken down and easily removed by the developer, leaving only the unexposed regions. Hence, a positive film image produces a positive image on the wafer, which is what is needed. Once the ten–times enlargement of the mask has been printed out (several pages for a ~3ft by ~3ft enlargement), the printer margins can be trimmed off. Tape the pages together as

accurately as possible and fill in with a black marker any white specks on the oscillators; also fill in the small gaps between the pages. Some sort of alignment pattern ought to be added to the mask because ultimately the mask will have to be aligned with the crystal lattice, i.e., the wafers flat (probably a (100) direction; however, one lot of wafers had the flat along the (110) direction)! A series of narrow bars provides a good set of markers hopefully, one will line up in the neighborhood of the wafer flat. For more advanced micromachined structures, with multiple mask levels, alignment patterns between the levels will have to be made. For the current generation of large (stationary probe), small (rotatable probe), and microscopic oscillators (NMR system), only one mask level is used. Self–aligned procedures are usually recommended for most semiconductor processing. With the huge blow-up in hand, request a photo reduction of the poster by ten times onto 7 mil high contrast at Miller Blue Print Inc.. For the NMR oscillators, a one hundred times reduction is needed. The films maximum resolution is around 10 μm: given a 10 μm × 10 μm square, substantial rounding of the corners will occur. Remember! A positive is wanted, but a negative is produced in the photographic process; thus, an extra image transfer is needed. However, there is an exception; for any structure that will be made by heavy etch stopping implantation, a negative is needed.

The film is basically a soft copy of the mask, which should be transferred to a more durable hard copy, the glass mask. This step is carried out at the MERC in the GaAs lithography bay, i.e., the place with the yellow lights. If you use these facilities, treat it as a holy shrine, be courteous of others, clean up after yourself and you just might keep your cleanroom privileges. The blank green

glass masks come from Nanofilm Inc. in California. Several mask sizes are available from one to several inches. For single chips, a 2 × 2 in mask is quite convenient; for 3 or 4 in wafers, a 5 × 5 in mask is a prerequisite. As previously mentioned, the mask has a layer of iron oxide or chrome with AZ1350J photoresist on it. The type of resist should be checked so the correct developer can be used. Occasionally, one can get away with the wrong developer. Iron oxide masks have the very nice feature of being somewhat transparent to visible light; hence, one can see what is being exposed through an iron film mask. The cleanroom processing goes as follows: Pre-bake mask for 15 minutes at 90°C. Place the film over the blank mask with the emulsion side of the film down against the resist. Put a piece of Plexiglas or clear green glass over the film so it presses the film flat against the mask. Flood expose this for approximately 50 sec with the HTG exposing system. Develop the mask with Microposit 452 or Shipely 325 for one minute or until the pattern is clear. The 325 developer is for AZ1350J while the 452 is for 5209 resist. Rinse with DI water. Post-bake mask at 120°C for 30 minutes. At this point the resist is stabilized and no longer photo-sensitive. The mask can now be taken out of the lithography bay. With iron oxide mask etchant, etch off iron in open areas through to the glass. This may take a few minuets depending on the age of the etchant. The etch rates should be 50 Å/ sec for Met 10 and 35 Å/sec for Met 35—these are commercial etchants available from Transene. Rinse with DI water, strip resist with acetone, clean mask with ethanol then DI water. The hard mask is done. Although it is tougher than film, it is still easy to scratch the metal film, so be careful with it as scratches and pits become magnified during the etching process.

Wafer Lithography

Many of the same steps used in the mask lithography are used in the wafer lithography. The first obvious difference is that the pattern is now being put onto a wafer and not a blank mask. Wafers can be purchased from Nova Electronics in Dallas. Nova is a supply house, not a manufacturer, so stocks vary in time. The last half-lot of 25 wafers bought were double-side polished 3 in wafers. All future purchases should be 4 in wafers as most equipment at the MERC is for 4 in.. P-type, boron, (100) orientation, 15–30 ohm-cm, 14–16 mils are the other specifications of the last lot. The resistivity should probably be kept over 1 ohm-cm (this corresponds to roughly 5×10^{16} ions/cm^3), and (100) is safer to stick with than (110).

The wafer lithography occurs after the necessary films have been put down on the wafer. The film process is described in the section below. A dump-rinse can be used to clean large dust particles off the wafer. Next a bake at 120°C is needed to dehydrate the wafer surface. This bake must be done even if no dump-rinsing has been done. A layer of primer is dripped with an eye dropper onto the wafer so that it is entirely covered. The primer helps the resist adhere to the wafer. Wait for 10 seconds to let the priming take effect, then spin it off the wafer with a 10 second spin. Immediately afterwards, drip 5209E photoresist on the center half of the wafer. The "09" in this number refers to the thickness after spinning at 4000 rpm. Spin the resist off at 4000 rpm for 30–40 seconds. Pre-bake the wafer at 90°C for 5 minutes to drive off excess solvents. Now the wafer is ready for the mask. Align the wafer flat to the alignment bars on the mask with

the HTG exposure system. Expose wafer for about 50 seconds—check log book for times that people are currently using. Time may need to be increased to 75 seconds if the bulb is getting weak. The intensity can be measured with a meter and compared to logged values; the intensity should be on the order of 2.8 mW/cm^2. Overexposing is more forgiving than underexposing because if resist remains where it is not wanted, the pattern will not etch. Although it is not always easy to tell on which side of the mask the iron is on, make sure the iron side is in contact with the wafer or the resist lines will look jagged and the pattern size will be magnified. After the exposure, place the wafer in a bath of AZ425 developer for about one minute while slowly agitating the tray. One should see the pattern developing. When the film underlying the photoresist is clear, the developing is done. Rinse wafer with DI water and blow off the residual water with the nitrogen gun, but be careful not to scratch the wafer with the tweezers. Flood expose the wafer, 3 seconds with lamp on and then wait 4 seconds with lamp off, for a total of four sets; this procedure will drive the solvent from the remaining resist. Finally, post-bake the wafer for 45 minutes at 125°C to completely stabilize and cross link the photoresist polymers. The wafer should no longer be sensitive to white light, and the resist should now be sufficiently hard for etching.

If mistakes are made with the resist or during exposure, the resist can be stripped with acetone and re-spun. This reprocessing can be done with wafers and also with the 2–in masks.

Wafer Films

Films may be deposited or grown on the wafer surface. Films play a variety of functions in semiconductor processing. For micromachining the big and small oscillators, the film serves as a protective layer. The protection is usually against chemical attack, but can sometimes be used as a barrier to prevent ion implantation. In some cases, the film is not a protective layer, but is the actual machined structure; AFM tips are an example of this, the first generation NMR oscillators are another.

In order to etch structures from the silicon, some portions of the wafers must be covered by a protective film, which prevents the plasma or etching solution from coming into contact with the silicon surface. The protecting film may be attacked and partially removed during its protective role. If this is the case, the etch rate of the protective layer and time exposed to etchant must be known so a film of sufficient thickness can be put down. The time of exposure to the etchant is related to the etch rate of the underlying film and to the depth to which one wishes to etch. For the first attempt, a wet oxide film, wet SiO_2, was grown. SiO_2 has the desirable property that it can be easily removed at a rate of 1000 Å/min with Hydrofluoric acid (HF) once it is no longer needed. (Note, although HF is a weak acid, it is biologically very dangerous. Since it does not burn immediately, exposure can go unnoticed for some time. During this time it is readily absorbed through the skin and proceeds to cause damage to nerve cells and bone. At this point it becomes very painful; calcium injections directly into the bone may be required. Be careful with HF.) Wet oxidation of silicon leads to

a lower quality film than dry oxidation, so all the dangling bonds and defects in this material lead to faster and more unpredictable etch rates than are found with dry oxidation. The etch rate for oxides usually runs around a couple 1000 Å/min for a low density oxide, 2.1 g/cm, in buffered HF (BOE—buffered oxide etchant) to 1000 Å/min for denser higher quality oxides, 2.25 g/cm. Dry oxide, however, cannot be used for long etches because it takes too long to grow a very thick film, as is shown in Fig. 3.4 for (100) silicon.

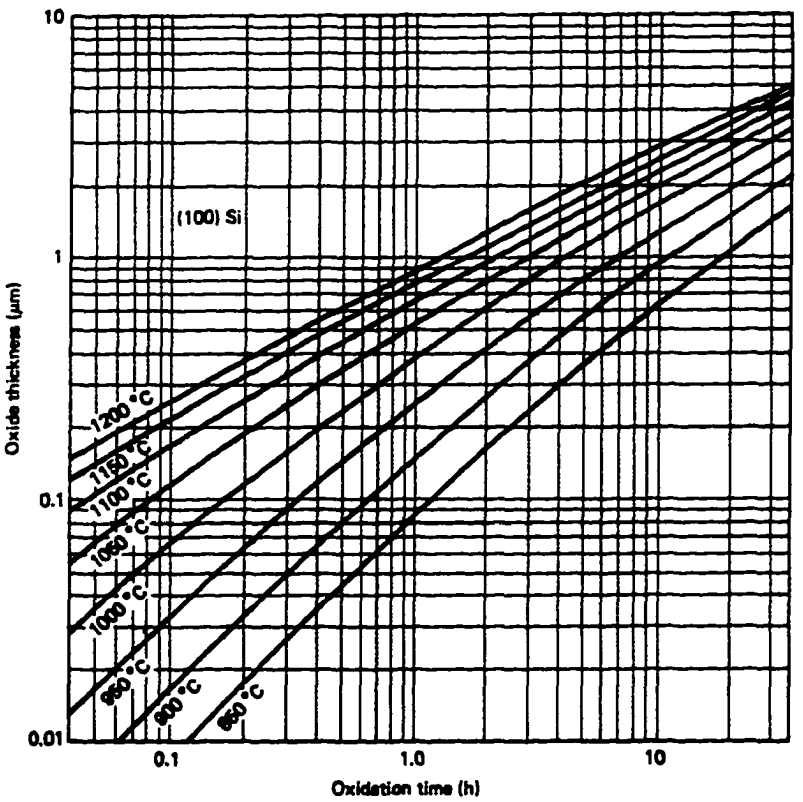

(a)

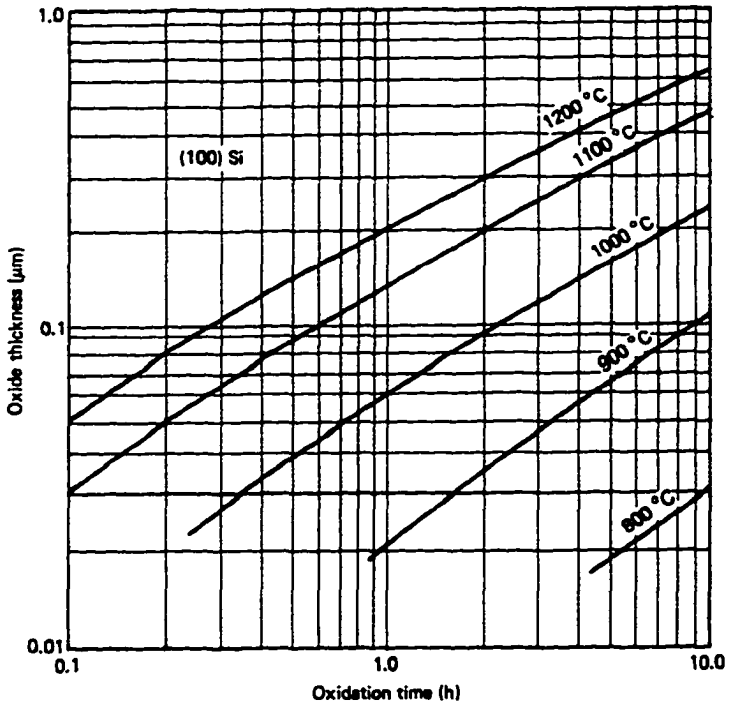

(b)

FIG. 3.4. (a) Time to grow a wet oxide film with a steam process. (b) Time to grow dry oxide film with dry oxygen. Notice the order of magnitude difference in the thickness given the same time and temperatures for the two processes [Ghandi, 1983].

The oxide growth rate also depends on the wafer orientation, i.e., (100), (110) or (111). An anneal may be carried out to densify the oxide, this densification would probably improve the etch resistance; this was never tried. Initially, around 12 000 Å of oxide was grown in order to etch clean through a 15 mil (0.38 mm) wafer. This proved to be insufficient. The etch rate of the SiO_2 was too fast and variable, especially on the back side of unpolished wafers, so a switch to silicon nitride was made. Silicon nitride, Si_3N_4, is an extremely chemically resistant, tough film with high tensile stress, $(1.2–1.8) \times 10^{10}$ dyn/cm^2 as compared to a

compressive stress of 3×10^9 dyn/cm^2 for SiO_2. The high stress means that for films greater than 1000 Å, the film may crack, so a thinner layer is required for masking. A 750 Å layer proved quite adequate. Although low strain nitrides do exist [Burns, 1990], the MERC's are not and changing tube chemistries is not permitted. Furthermore, low strain nitrides would most likely have higher etch rates and would produce lower *Q's* for the nitride oscillators.

Should the microscopic crystalline silicon torsional oscillators ever become a reality, they will be made by ion implanting the silicon with the desired pattern. The pattern will be determined by masking regions of the wafer with photoresist, SiO_2, or nitride to prevent doping in these regions. Baked photoresist would be the easiest to work with and pattern, but for heavy doping—doses over 1×10^{18} cm^{-2}—the photoresist may crack. Thus for high-energy high-dose implants, nitride or SiO_2 should be used. Initial calculations show a dose of 1.4×10^{16} boron ions/cm^2 at an energy of 134 keV is needed to make the silicon NMR oscillators. To mask at this energy, 0.5 μm of Si_3N_4 or 0.7 μm of SiO_2 would be needed to stop 99.99% of the implant (Fig 3.5). To play it safe, 0.75 μm of SiO_2 will be used. More on the doping can be found in the later section on ion implantation.

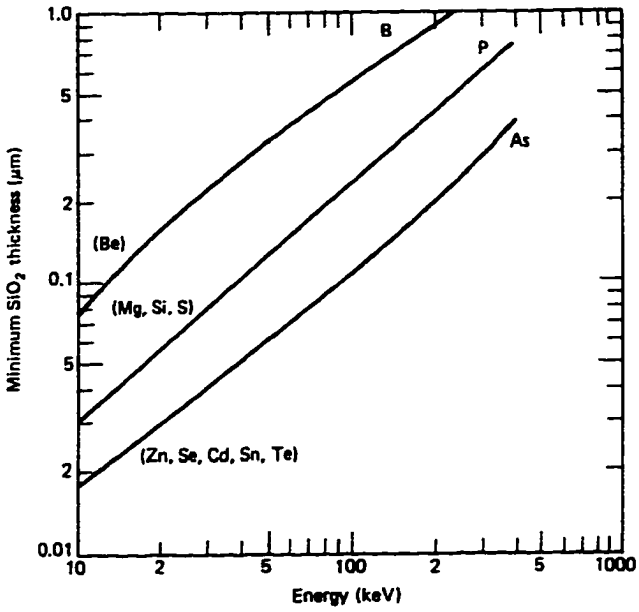

FIG. 3.5. See next page.

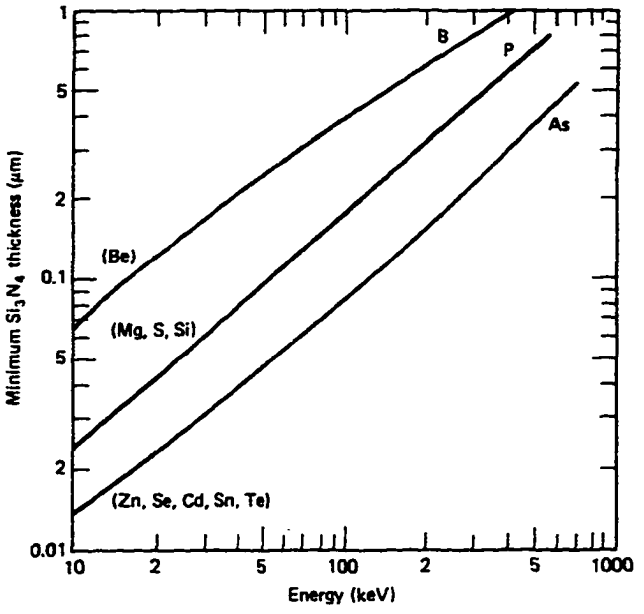

FIG. 3.5. Figures depict film thickness (SiO_2 above and Si_3N_4 below) needed to mask 99.99% of ions for various implant energies [Dearnaley, 1973].

A film may also be part of the desired micromachined structure. There are many such examples: membranes in microphones, accelerometers, AFM tips, even NMR oscillators [Prescesky, 1992; Burns, 1990; Hoen, 1993]. These are largely all mechanical sensors of one type or another; films for electrical interconnects will not be discussed. The nitride NMR oscillators were 5000 Å thick as determined by a Nanospec ellipsometer. The nitride was grown on (110) silicon to reduces film stresses [Hoen, 1993]. Nevertheless, such a thick film still led to severe cracking and pealing of the film during the wet etch. Despite the cracking, not all the oscillators were lost. Some subsequent efforts to stop the cracking were made. These included going to a 2000 Å film to reduce stress and

using the 4:1 rule. The 4:1 rule dictates that a layer of SiO_2 is grown first and then a nitride layer, which is 1/4th the thickness, is put down next. Supposedly, the tensile and compressive stresses of the two films will tend to cancel. Unfortunately for free hanging oscillators, this did not work exactly as planned, and the oscillators had a tendency to curl. Although this is a useful trick for many applications, the time and wafer expenditure needed to make it work for this case deemed it unsuitable. An attempt at making thinner, 2000 Å, oscillators did not work. Although the 2000 Å oscillators did not crack nearly as much, the oscillators were much more fragile and did not survive the etch or removal from the etch; (the surface tension of the liquid can cause breakage when removing or drying.) For this reason, 4000 Å for the nitride oscillators has remained the current thickness target.

Wafer Etch

Etching is the selective removal of an unprotected layer. For example, the developing of the photoresist pattern is technically etching. Similarly other layers can be partially removed. The resist will become a mask itself when etching the SiO_2 or Si_3N_4. A good reference for etching is Runyan, 1990. As previously mentioned, SiO_2 can either be etched with a reactive ion etcher (RIE) or buffered oxide etchant (BOE). Nitride can be removed in boiling phosphoric acid or by the RIE. The reactive ion etcher uses an oxygen and freon plasma to etch. It removes nitride at the same rate as baked photoresist, so the protecting photoresist layer must be at least as thick. BOE does not etch nitride at an appreciable rate, yet straight HF does. The problem with HF is that the photoresist will not adhere to a

surface in the presence of straight 49% HF. Thus a plasma is the most practical method for etching nitride.

The anisotropic etching of silicon requires a different etch. The primary silicon etch solution is as follows:

- 250 g KOH (potassium hydroxide)
- 200 g n-propanol or 2-propanol (isopropyl alcohol)
- 800 g H_2O

The KOH etch does not attack heavily doped p-type silicon, i.e., over 7×10^{19} [Bohg, 1971: Palik, 1982]. The etch rate for SiO_2 in KOH etch at 80°C is reported to be 20 Å/min [Kaminsky, 1985]. For the wet oxide put down at the MERC, the etch rate under the same conditions is considerably higher, 30 Å/min. Table 3.2 gives some useful etch information for the various etches summarized from papers referenced in this section.

Etch	**Characteristic**	**Composition**	**Rate/Comments**
BOE	etches SiO_2	7:1 NH_4F:HF	~1000 Å/min @ RT
RIE	etches Si_3N_4, SiO_2	CF_4 & O_2 plasma	~500 Å/min SiO_2, Si_3N_4, resist
(110) KOH	anisotropic Si etch 100 × (111) rate stops on p++	KOH n-propanol H_2O	~1 μm/min @ 80°C Si_3N_4 14 Å/hr SiO_2 30 Å/min
(100) KOH	anisotropic Si etch 600 × (111) rate	50-50 by volume KOH	same as above

	stops on p++	H_2O	

Table 3.2: Etch notes.

A great deal of work has been done on KOH etches [Bean, 1978]. The slow etch rate of the (111) planes relative to the (100) and (110) was initially thought to be related to the density of dangling bonds which are 1.36×10^{15}, 0.96×10^{15}, and 0.78×10^{15} cm^{-2} on the (100), (110), and (111) respectively. Supposedly, the (111) would oxidize the quickest in solution, resulting in an oxide layer that would passivate the surface and slow the etch. However, this does not explain the relative sequence or size of the etch rates observed in a $KOH:H_2O$ etch. Furthermore, the (111) is not always the fastest oxidizing surface. Recent work by Kendall has been proposed to explain the different rates [Kendall, 1990]. In the new model, three water molecules form a "tripod ion" around an OH^- ion, $OH:3H_2O^-$, similar to a hydronium ion in an acid. These complexes attach to dangling bonds. However, they can most easily attach to the threefold symmetric (111) surface allowing only water molecules to etch the surface and not the very reactive OH^- ions.

The patterned or doped wafer is mounted on a Teflon ring and suspended in the etch solution. A simple double boiler is made to keep the solution temperature uniform. A stir rod is used for the large oscillators, and the temperature is set at 60°C (a setting of about 4 on the hot plate). The KOH wet etches have an exponential temperature dependence where the silicon etch rate decreases with temperature while the selectivity over oxide or nitride increases.

Despite taking longer, lowering the temperature will help if the mask is not holding up well to the etch. The etch should be kept covered so the solution concentrations do not change too much with evaporation. Occasionally, water (and alcohol for (100)) etches should be added to account for evaporation. Water should also be added to the double boiler if the level becomes too low. The etch time is normally a couple of days. The etch may be turned off at night to avoid excess evaporation from the etch or double boiler. Should the temperature of the etch become to high, the entire wafer may dissolve—mask and all! This is why it is best to monitor the etch.

Two etches not used much, but which are worthy of mentioning, are the P-ED etch (pyrolcathechol, ethylene diamine, water, and pyrazine) and planar etch. The P-ED etch is an organic etch for silicon [Finne, 1967; Reisman, 1979; Lee, 1969]. It is a fast anisotropic etch removing more than 25 μm/hr of silicon at 100°C. On the other hand, the rate is variable when exposed to air, and at 100°C, the vapor poses a serious health hazard. For these reasons, it was dropped. The planar etch (HF, HNO_3, H_2O, and $HC_2H_3O_2$) is for isotropic etching of silicon [Robbins, 1960]. The planar etch can be used to under cut a nitride film. The etch rate should be kept low by reducing the nitric acid content and greatly increasing the water content. If the rate is too quick, the hydrogen that is produced forms fast moving bubbles that will break any structures being made. This etch does not stop on heavily doped silicon; in fact, it may speed up.

Ion Implant

As mentioned in the film section, an estimated dose of $1.4 \times 10^{16} B^+$ ions/cm^2 at an energy of 134 keV is needed to the make 4000 Å thick silicon oscillators. This thickness was chosen to put the frequencies in the mid-10's of kHz. The peak of the implant, R_p, was targeted for a depth of 4000 Å. The energy needed for this depth can be read from Fig. 3.6.

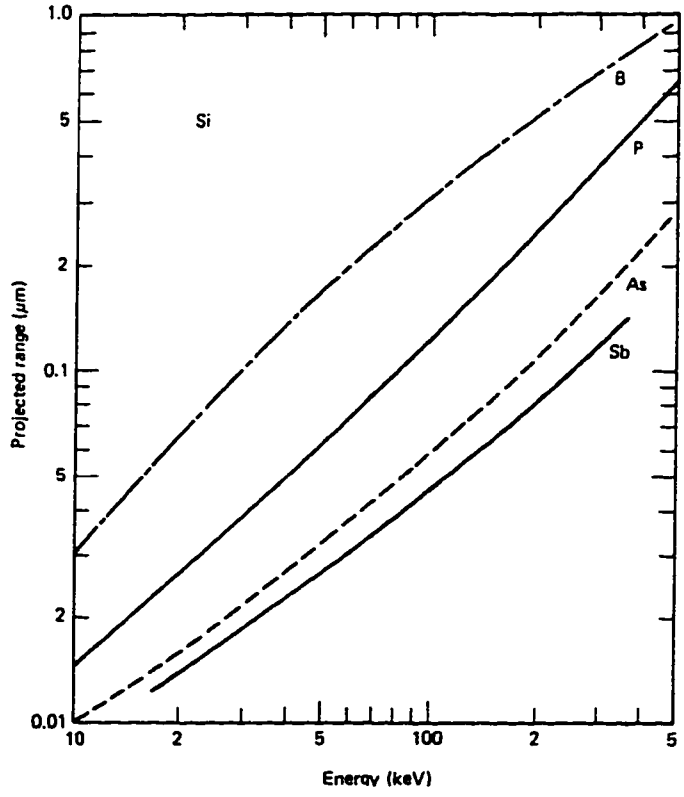

FIG. 3.6. Peak in the implant concentration depth vs. implant energy [Gibbons, 1975].

At this energy, the straggle, "the gaussian's width," is 0.08 μm as seen in Fig. 3.7. The overall profile should be similar to the curve in Fig. 3.8 where no temperature

activated diffusion has taken place, i.e., $Dt = 0$ where t is the anneal time in seconds. D is the temperature dependent diffusivity given in cm^2/s by Eq. 3.11,

$$D(T) = 3.17e^{-3.59/kT}. \tag{3.11}$$

In this equation, T is the temperature in Kelvin. The "3.59 eV" is an activation energy, and k is Boltzmann's constant in eV/K.

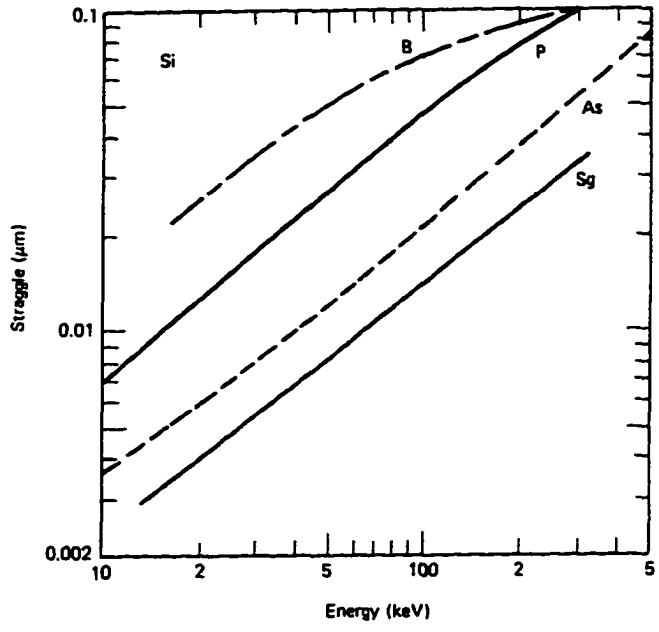

FIG. 3.7. Straggle for implants. The straggle specifies the gaussian width [Gibbons, 1975].

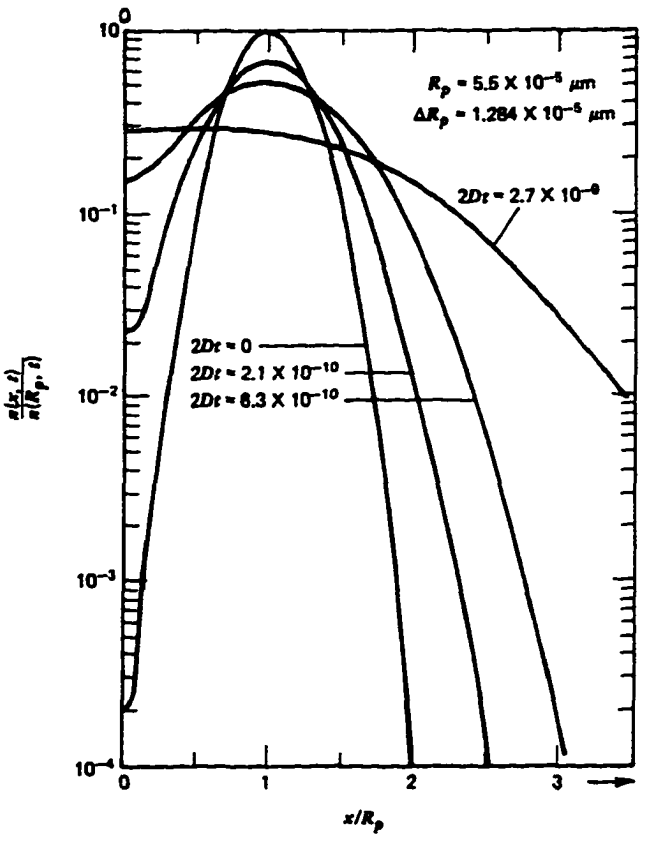

FIG. 3.8. Implant profiles normalized to peak implant concentration and peak implant depth [Seidel, 1969].

After the implant, a 15 or 20 min anneal at 1000°C will be needed to repair implant damage and activate the boron. The anneal must be short enough not to drive the boron into the substrate, thereby flattening the steep gaussian dopant profile needed for an abrupt etch stop. The result of longer anneals and the spreading can also be seen in Fig. 3.9. This figure was plotted from the modified dopant profile equation, given below, which was changed to account for

annealing affects. Figure 3.9 was normalized to the peak value for $t = 0$. Note that for $t = 0$ the standard first approximation dopant profile results:

$$N(x,t) = \frac{Q_0}{\sqrt{2\pi}\sqrt{\Delta R_p^{\,2} + 2Dt}} \exp\left[{}^{-(x-R_p)^2}\Big/_{2(\Delta R_p^{\,2}+2Dt)} \right] \qquad (3.12)$$

Equation 3.12 assumes the substrate boundaries are infinitely far away. Other equations are mentioned by [Ghandhi, 1983] to correct for a finite surface boundary, but they may not be correct.

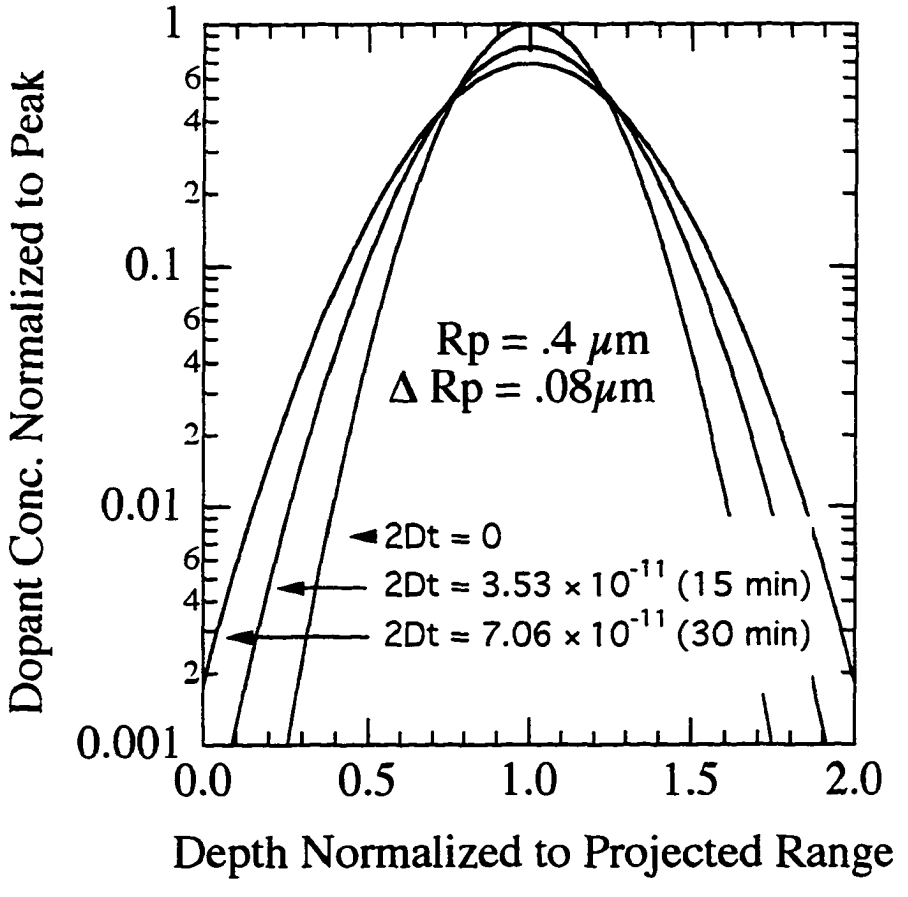

FIG. 3.9. Dopant profiles for various anneal times.

The dopant profile equation assumes that there is no channeling; otherwise, it can be grossly inaccurate. Channeling is a process by which the implant goes deeper than predicted for normal scattering events. This is possible when the ion beam is aligned with a major crystallographic orientation such that the implanted ions "channel" without collisions down the gaps in the lattice. To avoid channeling, the implanted region can be damaged by pre-implanting with the same ion species as the substrate. This procedure will create an amorphous silicon layer to prevent long mean–free paths of the dopant ions. Another method is to tilt the dopant beam by 7° with respect to the crystallographic direction. The final method, which is usually used in conjunction with the tilting, is to put down a thin amorphous film like SiO_2. For 134 keV, 150 Å SiO_2 should suffice to misalign the impinging boron atoms. This oxide layer thickness should be decreased linearly with energy.

Many of process steps described above such as the etch, oxidation, or implant can be modeled with a program called SUPREM. If access to SUPREM can be gotten through the electrical engineering department, it can accurately determine various process parameters, i.e., dopant profile, dose, anneal time etc. for the implant step.

HARDWARE

The hardware of the experiment describes miscellaneous parts of the experiment, excluding wafer processing and the cryostat, but mostly probe related items or preparing oscillators for the probe.

Epoxying the oscillators

Once all of the oscillators have been etched from the wafer and have sunk to the bottom of the beaker, they should be carefully removed and placed into another beaker filled with tap water. This beaker should be subsequently drained and refilled with tap water by using ones hand as a guide to channel the water to the side of the beaker and away from the oscillators. The fragility of the oscillators cannot be overstated. By repeating this procedure at least six times, the KOH can be effectively removed. The last couple of rinsings should be performed with distilled water. If the oscillators are going to be put aside at this point, they should be left in a full beaker of distilled water and covered with parafilm. Further, cleaning is recommended before metallizing the oscillators. Place the oscillators onto a large Kimwipe. Wearing latex gloves, the oscillators may be slid apart (not pulled) if they are stuck together and placed flat on the Kimwipe. Using a small Kimwipe folded into quarters or a Q-tip, the oscillator may be wiped with alcohol and or distilled water depending on what cruddy films, if any, are on the surface. Some pressure may be applied so long as the oscillator remains flat. Next, cut a piece of Teflon tape—approximately 6 cm by 0.5 cm. Holding the oscillator by the lower half in one hand, wrap the Teflon tape around the upper neck and head so that these regions are completely covered by the tape (Fig. 3.10a).

FIG. 3.10a. Masking the oscillator head. Photo sequence depicts method used to floss Teflon tape between the head and wings and then to wrap around the head and neck.

The tape must not cover any part of the wing or base on the side that is receiving metal. If the oscillators are going to be put aside at this point, they should be

covered with a Kimwipe. The oscillators are now ready to get metallization layers that will allow charge to be put onto the face. Clamp the oscillators in the circular ring holder with the alligator clips. This holder and the evaporation chamber lives in Cryogenics. The face of the oscillator is usually the polished side for one-sided wafers (the side that received the lithography). This side receives metal and is the one with the slightly smaller area. If one is looking down on this side, with the base nearer you and head further, the oscillator must be clamped on the right-hand side. The clamp will leave a shadow that has no metal. Thus, the base wire will be on the left-hand side, which is the correct side to fit the probe. Evaporate 20 Å of chrome and 100 Å of gold. The chrome allows the gold to stick to the oscillator surface, especially in the presence of SiO_2 films. The actual evaporation is done by Cryogenics. Once this is done, remove the Teflon tape gently; the oscillators are ready to be a wired and epoxied.

Clean a 14 mm long piece of copper wire (physically bigger than 20 gauge) or narrow copper strip with a weak nitric acid solution, such as chrome hearth etchant listed below, rinse and dry.

100 cc glacial acid

100 cc phosphoric acid

200 cc nitric acid

100 mg sodium nitrate

100 mg ammonium chloride

The wire is overlapped with the lower edge of the left-hand side of the base by around 3–4 mm and silver epoxied with Amicon C-751-2 silver epoxy from Cuming, Inc. A small support needs to be placed under the wire so that it remains

in flat contact with the oscillator. By gluing a broken piece of an oscillator on a glass slide, a convenient support step for the wire was made. This type of silver epoxy needs to be cured at 350°C for a few minutes. A dab of Stycast 2850 FT may be placed over the silver to strengthen the connection—2850 FT will cure overnight at room temperature.

A set of six Teflon molds have been made for epoxying the oscillators' bases. First cut two small 3 mm sections of 20 gauge Teflon tubing. Press flat and place on the bottom of the mold so that they lie across the width. These strips should be spaced ~1.5 mm apart. They serve as standoffs to stop the oscillator edge from being exposed and shorting the high voltage to the probe, which is kept at ground. The hole at the bottom of the mold should be filled with vacuum grease. It is there to allow the oscillator to be pushed out once the epoxy has set. The molds have three set screws to stand the oscillators upright (Fig. 3.10b).

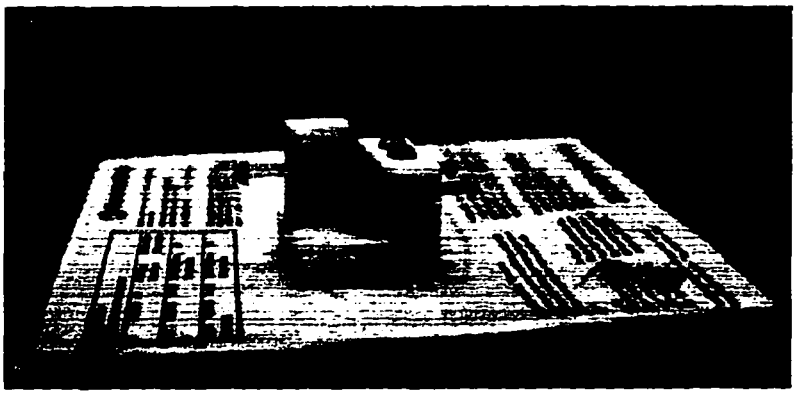

FIG. 3.10b. Epoxy jig for oscillator.

The two adjacent set screws make contact to the back of the wings. The third lone screw should not be screwed directly into the face because this would clamp

the oscillator firmly in place. The oscillator will shift a small amount when the epoxy dries; if it is firmly clamped at the top, it can break. To avoid this, a small wedge of wax paper folded into a "V" should be inserted between the oscillator and third screw (made from nylon). This produces a spring to press the oscillators against the back screws without clamping. The width of the epoxy base was initially 3/16 in. This is the upper limit of what the jaws of the probe stage will accommodate making it difficult to remove and insert oscillators. For this reason, the base's width was reduced to an 1/8 inch. This proved to be disastrous. The mismatch between the epoxy and silicon caused the oscillator bases to fracture entirely through the epoxy upon cooling. This complete breakage did not occur for a set of thick bases that were made with the same batch of epoxy at the same time as the thin bases. Clearly the thicker base allows some amount of thermal contraction mismatch. Nevertheless, there may still be some cracking of the silicon even in the thick base although not as much. The cracks in the silicon may be responsible for the glitches and sudden jumps in the data. No epoxy with as good thermal conductivity, electrical isolation, hardness, and match to silicon's thermal expansion has been found to be better than 2850FT. A ceramic might work and may be worth looking into, but it must be very solid, able to cycle, and set in a finite amount of time! A more feasible approach may be to add high purity silicon powder to the epoxy—maybe 25% by weight. This might help to reduce stress on the oscillator and stop it from cracking. A return to a thicker base is also necessary; however, it probably does not have to be as thick as 3/16 in. A base between 5/32 in might be a good compromise. The depth of the new mold shoulds also be increased by ~25 mils. The epoxy will cure overnight

at room temperature or in ~4–8 hrs at 45–65°C. The screws should be backed off and the support that holds the lone screw removed—careful that the support does not rotate into the oscillator when it is removed. The oscillator can be pushed out of the mold by pressing a Q-tip through the greased hole.

Electrodes

The last electrodes made use Stycast 2850FT as an insulator. Previously they used Stycast 1066. A suspicion arose that the epoxy was breaking down with all the thermal cycling at a high voltage, so the electrodes were replaced. Now, 2850FT is NOT machinable. So the new electrodes were made by epoxing the inner conductor in place. To make new electrodes, grease the outside threads of the outer conductor in case any epoxy gets on them. A Teflon cylinder, the same diameter as the inner conductor, is centered inside the outer conductor with a jig. Both the Teflon cylinder and the inside of the outer conductor are coated with epoxy—gaps and moisture traps in the dielectric are to be avoided. Remove the Teflon plug, and glue the inner electrode to the bottom of the jig. Pour epoxy in. The inner conductor of the drive electrode is recessed by 10 mils, while on the pick-up electrode, it protrudes. Two sets of 2850FT electrodes were made. One set has a threaded outer conductor, and the other has a smooth outer conductor. The threaded electrode allows for more careful positioning of the electrode with reduced risk of accidentally ramming the oscillator. The down side is that the coax connections have to be unsoldered if the electrodes are moved any sizable distance because the coax will break from the twisting. The smooth electrodes do not offer the anti-ramming protection, especially to those who have VERY

unsteady hands; however, they do not require unsoldering of the coax because no twisting is involved. The second set is kept with the oscillator station.

Thermometry

The thermometry of the probe includes a platinum thermometer good down to ~ 30 K, a germanium thermometer for accuracy at lower temperatures, and a carbon-glass thermometer for low temperatures at large fields. Specifics about the thermometers can be found in the Lake Shore Cryogenic catalogue. All thermometers were calibrated in reference to the lab standard. Calibration tables can be found in the black *osc probe* folder, which is kept with the other probe folders. Further information on thermometer calibration can be found in the classic Experimental Techniques in Low–Temperature Physics by White, 1987.

Probe

Detailed machine shop drawings for the various probe parts such as the electrodes, flanges, vice stage, etc. will not appear in this document. A photograph of the fixed stage probe is shown in Fig. 3.11a; because the actual probe is readily available, further details will be left to inspection. Similarly, detailed shop drawings for the rotatable stage probe will not appear. A sketch is shown in Fig. 3.11b.

However, a few useful wiring facts are in order. Three labeled BNC's connect the probe's high voltage, drive electrode, and pick-up electrode to the outside world. The probe has a 29 Ω heater which with, all thermometry, is connected through a 24 pin connector. Internally, all electrical feed-throughs have a layer of Stycast 1066 epoxy set around the pins to make them vacuum

tight. Soldering to them at a later stage could cause leaks to develop through the epoxy. The pin connections are given in Fig. 3.12.

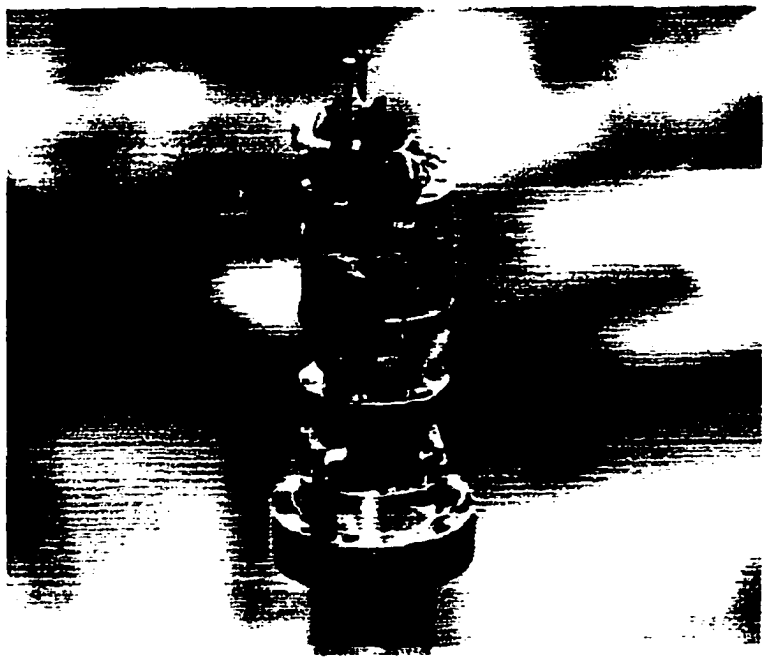

FIG. 3.11a. Fixed probe stage.

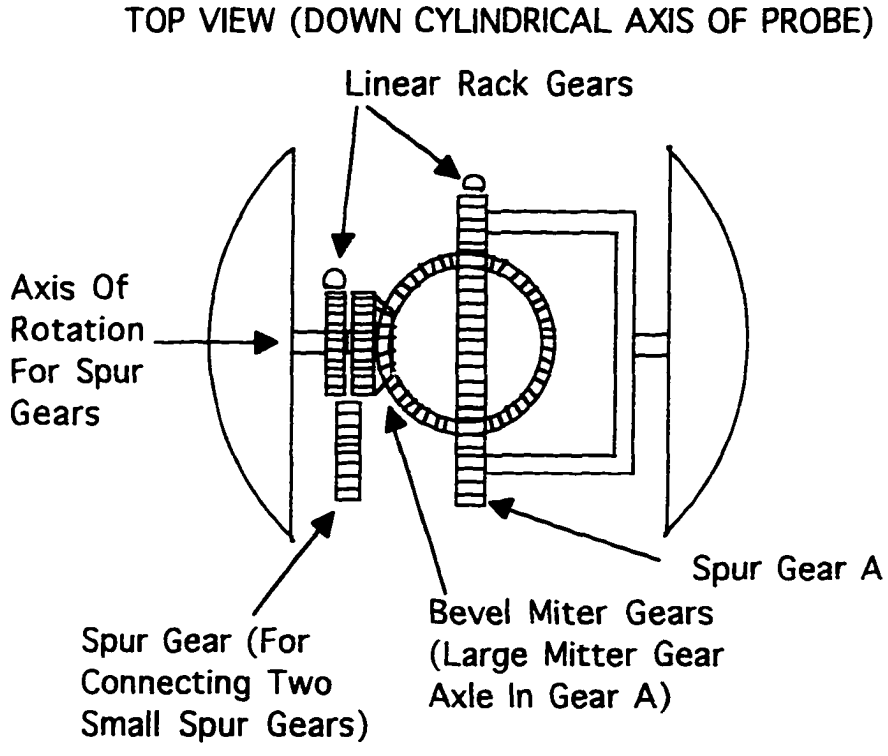

FIG. 3.11(b). Sketch of rotatable stage. This is under construction.

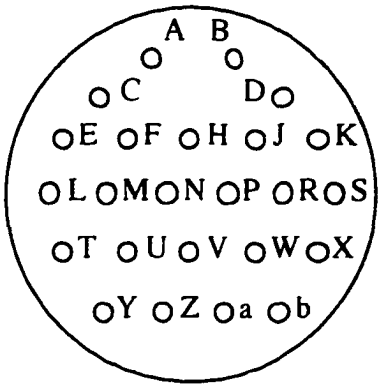

A
B Heater 42.1 Ω

E I+
F V+ Platinum Ther. PT103
J I- JE 113.7 Ω KF 113.6 Ω
K V-

L blue V-
M yellow V+ Germanium Ther.
N black I+ ML 6.9 Ω NP 10.2 Ω
P red I-

R black I+
S red I- LAB Standard (when added)
W blue V- RS 10.4 Ω WV 7.8 Ω
V yellow V+

C
D
H Not Used
T
U

a black I-
b white I+ Carbon Glass Ther.
Z green V- ab 14.7 Ω ZY 15.7 Ω
Y yellow V+

FIG. 3.12. Pin connections for fixed probe.

Automation

Attempts at automating the experiment were not successful. Keep in mind that for some oscillators the Q can be close to a 1 000 000 at 100 K and the frequency sensitivity 0.0005 Hz. At the same time, the frequency changes can be quite quick, perhaps 0.01 Hz/sec, so the frequency change per second is far greater than the resonance width. Remember, resonant frequencies are typically around 9000 Hz. To make matters worse, there are the occasional spontaneous frequency jumps that most likely arise from cracks in the oscillator. In any automation scheme, these spontaneous jumps will be very difficult to account for, and so a person may still need to be present in case they occur.

Nevertheless an automation scheme in which an error signal, using the elastic amplitude, is generated if the driver moves off of the resonance and can be used to change the drive to move back on the resonance. A block diagram for two possible automation techniques is shown in Fig. 3.13. These are still useful for lower–Q resonances.

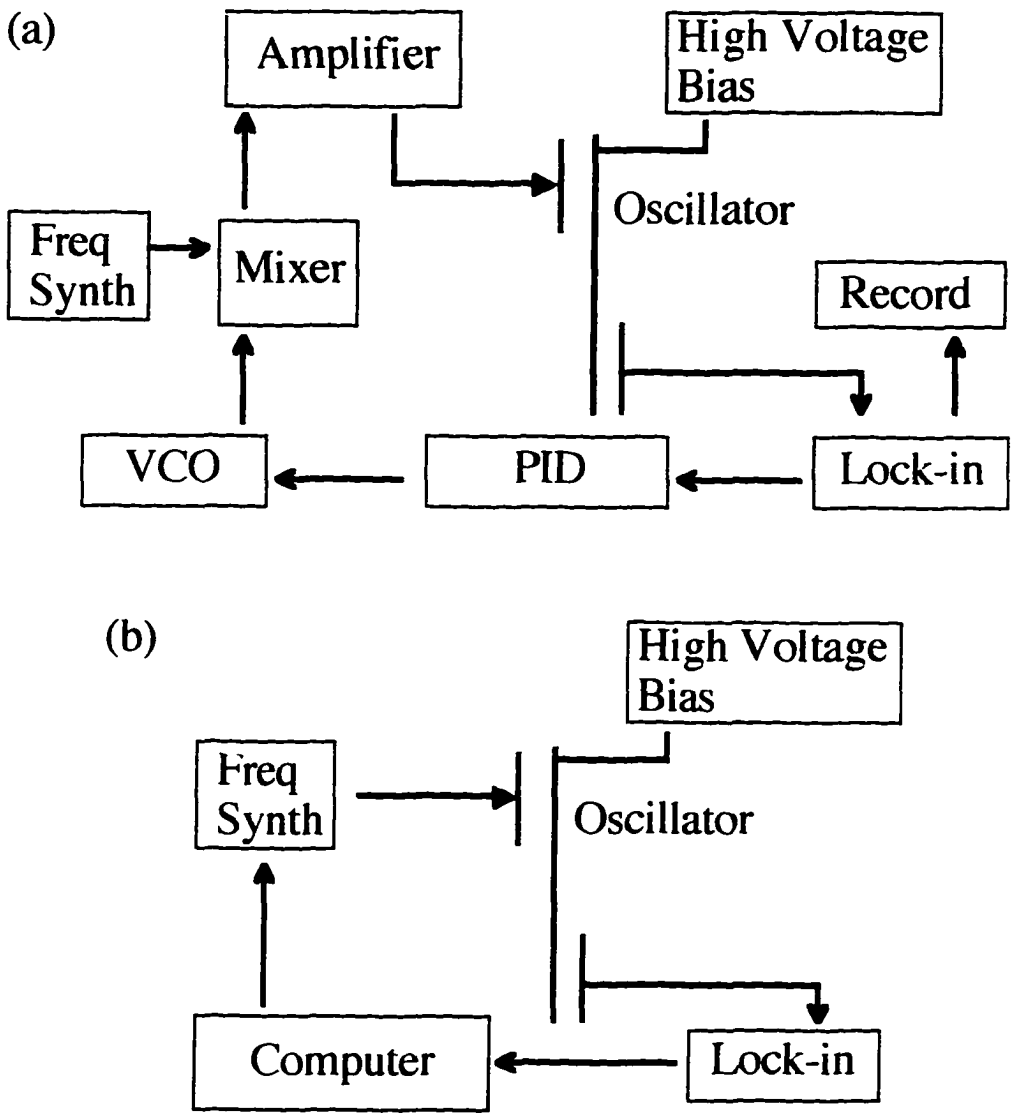

FIG. 3.13. Methods for staying on resonance: (a) analogue (b) computer.

The PID/VCO (voltage controlled oscillator) method is shown in Fig. 3.13(a) and the computer control is shown in Fig. 3.13(b). The PID is basically a temperature controller that takes an error signal, amplifies it through some combination of Proportional, Integral, and Differential gain, then uses the amplified signal as an

input to drive a power stage that supplies current to a heater, VCO, etc. [Swartz, 1985]. Further theory can also be found in [Moore, 1989]. Circuit diagrams for the various amplification stages can be found in other lab documentation. For the PID/VCO method, the error signal is sent to a VCO that then changes the drive frequency The main problem was that a VCO with sufficient stability could not be found. No VCO's with a stability higher than 1 part in 10^6 were availible. What is required is a stability of 1 part in 10^8, i.e., 0.0001 Hz out of ~10 kHz. One trick to get out of this quandary is to use frequency mixing. For most experiments, below 100 K, the frequency will change by a few Hz at most. So for a 10 kHz resonance, only changes of 1 part in 10^4 to 10^5 are actually relevant i.e., 0.0001 Hz out of 1 to 10 Hz. Thus, if the 3 orders of magnitude of unchanged frequency can be subtracted out, then a VCO technique might be possible. This can be accomplished by frequency mixing.

The other technique, Fig. 3.13(b), uses the computer to stay locked on resonance by reading the elastic amplitude and telling the frequency synthesizer to change the frequency by some amount if the elastic amplitude is not zero. However, LabView with the NI-488 board could only make 2 readings per second which is far to slow to track. In other words, the peak was shifting a substantial fraction of its width or sometimes more than its width, so the computer was never quite on resonance. Faster readings can be obtained with a PC running Lab Windows. Faster readings, at least 20 per second, would have allowed this method to work with the possible exception of the transition, which can be exceedingly abrupt. An A/D board instead of the lone NI-488 board would also probably help. Note, the Keithly 199DMM can act as a slow A/D board.

RUNNING THE EXPERIMENT

Although most of the time in performing an experiment occurs in the preparation done weeks in advance, there is a very intense period starting the week before with cryostat preparation and ending when all data has been gotten or more likely, when fatigue forces an end.

The Cryostat

The week before the experiment primarily consists of setting up the cryostat. This entails pumping it out and cooling down the magnet. The plumbing to the high-field magnet Dewar is shown in Fig. 3.14, and the Dewar schematic is shown in Fig. 3.15.

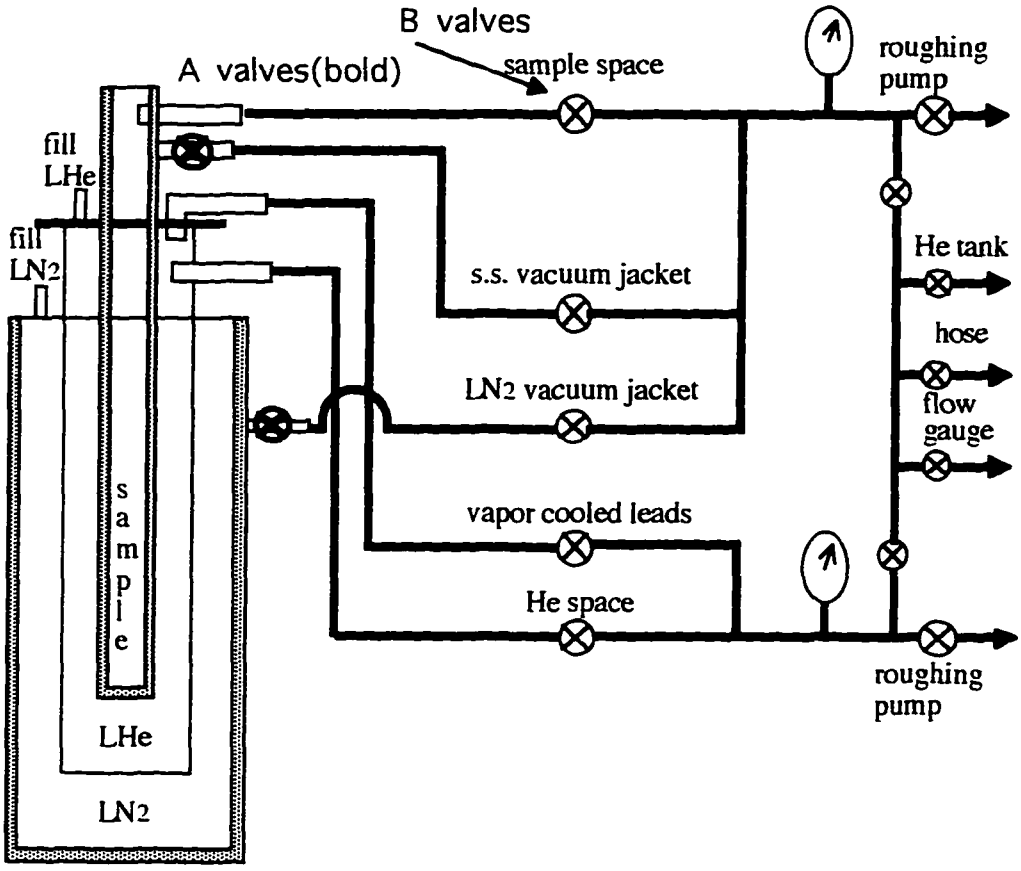

FIG. 3.14. Plumbing for cryostat.

The cryostat includes the nitrogen vacuum jacket, helium vacuum jacket, the sample space, liquid helium space, liquid nitrogen space, the plumbing to these spaces, various valves for isolation, choo-choo train exhaust valve, dry helium gas tank, two roughing pumps, two crude pressure gauges, one mTorr pressure gauge, needle valve, flow meter, superconducting magnet, Dewar thermometry, temperature controller, helium gas flow heater, magnet power supply and controller, superconducting switch, helium level meter, and helium transfer stick.

The general idea behind operation is as follows. Helium from the bath is channeled by a capillary into the sample space. The temperature controller controls a heater that heats the helium vapor that flows into the sample space. The helium flow in the capillary can be restricted with the needle valve. Between the needle valve and heater, temperature control of the sample space may be achieved. The magnet sits in the liquid helium bath, and of course, produces the field, up to 11 T in theory. The pumps, plumbing, valves, magnet control, etc. provide the arterial sustenance for the Dewar and whose purpose and operation are described in detail below.

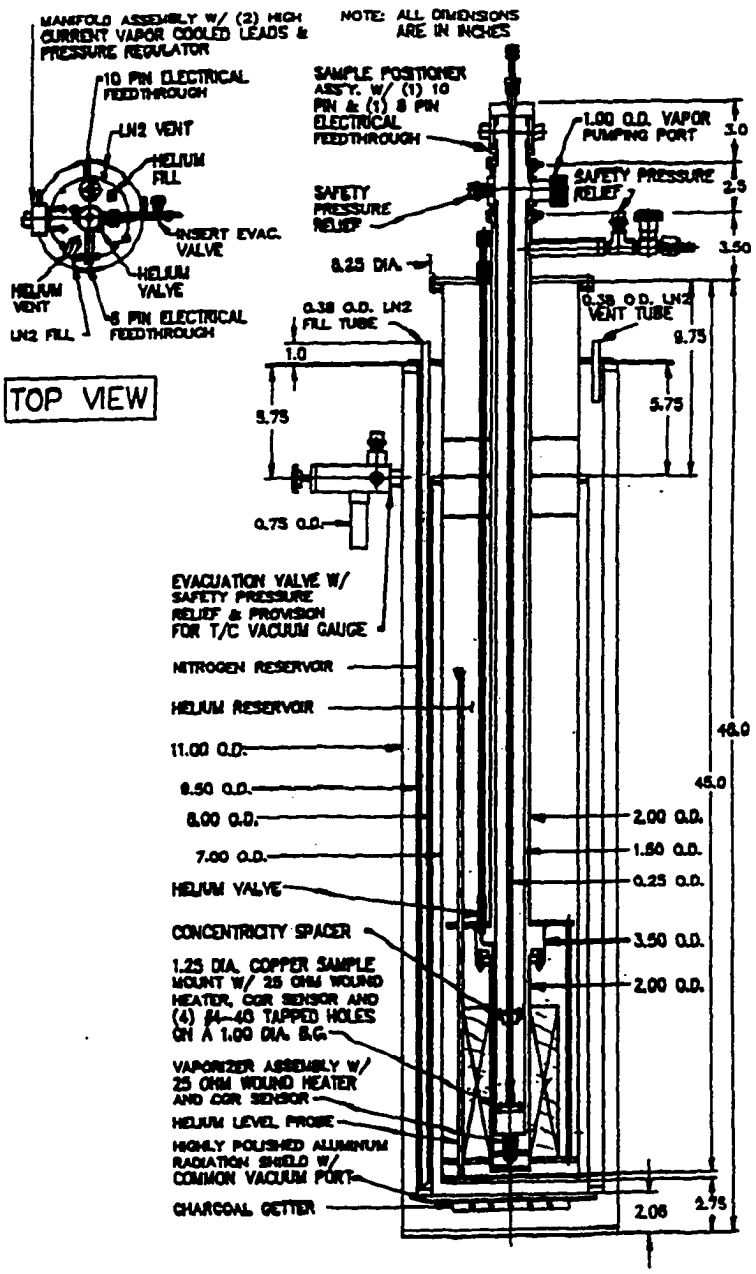

FIG. 3.15. Schematic for cryostat.

The Cool Down and Transfer

First, pump out the inner vacuum jacket and then the outer jacket. These must be pumped out first as the jackets can only take compressive pressure. When doing this, pump out the plumbing up to the last valves that isolate the jackets and check for leaks. There may be sizable outgassing in these lines. Pressures in both jackets should get below 100 mTorr; preferably to less than 30 mTorr. Do NOT back-flow helium into these jackets! Once the jackets have been pumped out, usually overnight, both "A" valves and the jacket "B" valves should be closed. Place tape over the jacket "B" valves so nobody accidentally opens them.

The needle valve should be closed (snugged with the fingers, not tightened with the wrist as this can cause the valve to permanently freeze shut after cooling). Always take care to note and check the status of the needle valve, the Dewar does not have temperature control without it.

After the vacuum jackets are pumped out, valve off the sample space and make sure there are no leaks in the plumbing to this space. Pump the space out. Once again this should easily get below 100 mTorr, ultimately down to ~25 mTorr after flushing with He. Back-fill this space with He gas. An under pressure should be kept when doing this procedure by filling to a pressure of 10 in Hg below zero (zero corresponds to atmospheric pressure). Pump out. Repeat the back-filling and pumping a few times. For the final fill/pump cycle, pump down to -25 in Hg and valve off the space. Do the same procedure for the liquid helium space; however, for this space, always back fill to -5 in Hg. Unlike for the sample

space, the last fill/pump cycle should end by back-filling to -5 in Hg. The LHe space is large and can trap a lot of gas and water vapor, so it may take quite a few fill/pump cycles to get the pressure on scale, let alone below 100 mTorr. This space is usually pumpable to between 30 and 60 mTorr. At some time in the future, the rubber hosing that joins the Dewar to the plumbing should be replaced with flexible stainless steel bellows. Huntington in Houston is a cheap source for such items.

Open the needle valve and bleed in pressure to sample space until the two spaces are approximately equal, -7 in Hg. Gently close needle valve. Fill the outer jacket with LN_2. Let the Dewar sit overnight filling with LN_2 whenever possible. Fill again in the morning, let sit for one hour and then top off.

The cryostat is now ready for liquid helium to cool down the magnet. During this whole transfer procedure, the idea is to cool the magnet and fill the LHe space without getting any oxygen in it. If the liquid helium transfer stick has not been used in a while, it is wise to pump it out. This will make for more efficient transfers. For the lab's 36 liter transfer Dewar, the stainless steel extension must be attached whenever cooling down the high-field magnet Dewar in order to reach the bottom of the transfer Dewar. The extension is also needed when transferring from a half empty Dewar. Connect an over-pressure line from a dry helium cylinder to the transfer Dewar; bleed this hose for a few seconds before connecting to blow air from line, but don't open the over-pressure valve on the transfer Dewar yet. Unscrew the choo-choo train valve compression screw. Put a very slight over-pressure on the liquid helium space, 0.5–1 lb. Open the transfer Dewar valve and insert the transfer stick into the Dewar and let the

helium over-pressure blowout the stick for a few seconds; this procedure will prevent oxygen from being blown into the liquid helium space. Place the other end of the stick in the LHe fill port. S l o w l y lower stick. (Note: if one is transferring LHe to an already cold magnet, one must get a flame/plume before inserting the other end of the stick into the cryostat. If one is cooling the magnet, then it is not necessary to get the flame/plume). Close the vent and safety relief valve on the transfer Dewar. Stop the over-pressure of dry helium gas to the LHe space, but do not cut it off to the transfer Dewar.

Once the transfer stick has reached the bottom, raise it half a centimeter. Adjust the regulator to less then 0.5 lb and slowly open the valve on the transfer Dewar, which is connected to the dry–He cylinder. Work the regulator until the choo-choo train valve makes a couple of puffs per second. The pressure gauge needle on the transfer Dewar should just split the "zero" marker, which is offset to the right. Do not be surprised if the regulator pressure reads zero. The transfer will take ~3 hr; during this time it will be necessary to adjust the regulator. The pipe leading to the choo-choo should not frost much; if it is frosting, the transfer is too fast. Record the magnet temperature periodically and compare to past runs in the log book. When the magnet temperature reads ~13 K, turn on the level meter periodically to see if collection has begun. Once it begins, leave the level meter on and connect a multimeter to it for easier viewing. The pressure can be turned to 0.5 lb, and after a level of 54%, a couple of lbs on the regulator (2 lb). Fill till the level meter reads 99% or the multimeter reads 103%. After this, the Dewar is being filled over 100%; this is okay, but the boil-off is faster at the top and one can't get a reading of the level. Stop the over-pressure and vent the

transfer Dewar. Replace the plug in the LHe fill port. Quickly lift the stick out; keep the heat gun handy to thaw o-rings on either Dewar. Turn off level meter as it burns a small amount of LHe.

Refilling is similar, but there are a few differences. Because the Dewar already has helium in it, no over-pressuring is needed when opening the LHe fill port. As previously mentioned, get the plume/flame before inserting into the transfer stick. This insertion should be quick. THE MAGNET SHOULD BE OFF, THE FLOW METER VALVE AND THE NEEDLE VALVE CLOSED WHENEVER FILLING THE CRYOSTAT DEWAR. The needle valve is at a level of 60%. When possible it is preferable to stay above this level; however, this is not an imperative if one has been careful not to get air in the LHe space. The magnet top is at 54%, so when running the magnet the level should not go below this level or else a quench may result. Quenching will be discussed in a later section. The superconducting switch is at 49%, this is even more critical if the magnet is on. The Dewar should be topped with LN_2 every 2 hours.

When putting a probe in the Dewar, it is best if the sample space temperature is above 100 K. This will help to stop air from accumulating inside. To put a probe into the cryostat, make sure the needle valve is closed, over-pressure the sample space with about 1 lb of dry helium. Lower the probe being careful not to put pressure on sample space walls. Turn off over-pressure. Open the flow meter. Turn on the temperature controller, and open needle valve half of a turn. Check the flow meter to make sure there is flow. Twiddle needle valve now and then. After 15 minutes, the needle valve can be opened more—this is a precautionary measure to try to blow any air out of sample space before it freezes.

Should the needle valve freeze, twiddling it and applying small amounts of heat after a LHe transfer has proved quite successful. It is also useful to achieve a good flow before closing the needle valve and transferring to prevent blockage from occurring in the first place.

The Magnet

Theoretically the superconducting magnet can produce fields up to 11 T when the LHe bath is pumped on and 9 T when not. Currently the magnet does not like to run with a positive polarity above 6 T. Exceeding any of these values can cause a quench. A quench occurs if the superconducting magnet has current running in it, i.e., it is in persistent mode, and the magnet suddenly becomes normal producing huge quantities of heat as the current is dissipated—remember $LI^2/2$. This heat produces a massive boil off of the precious LHe bath. For this reason, it is important not to over tighten the choo-choo valve because this is where the boiling helium vapor escapes. Should a quench start to happen, try to close the needle valve and wait till the quench is done.

The general control of the magnet is as follows. First, turn on the controller, next the small polarity box, and finally the power. Reverse order when turning off. Before ramping, make sure the He space vents through the vapor–cooled leads. Ramping up from zero field is the same as finding the magnet in persistent mode with zero current; hence, the persistent mode procedure will be described. The basic idea is that one does not want to expose the magnet to any large voltage jumps. So in order to change the current in the magnet, one must externally match the magnet current, thus canceling the current through the

superconducting switch. This procedure allows external control of the magnet's current without the magnet seeing any voltage spikes when the switch is broken (Fig. 3.16).

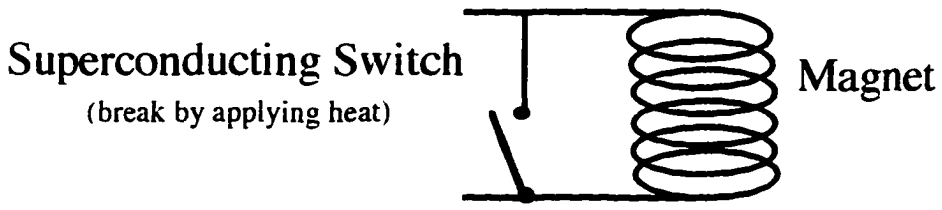

•Heater on/Switch open/Keyhole vertical

•Heater off/Switch closed/Keyhole horizontal

FIG. 3.16. Superconducting switch status.

Voltage spikes can quench the magnet. If the magnet is found in persistent mode (key out), first externally match the current by setting the current ramp range to 10 and setting the current limit to a value that matches the magnet value. The current limit may already be set to the correct value. (Check the magnet current in the logbook.) Toggle the current switch to the up position. Set the ramp range to 0.1. Put the key in and turn. Wait 15 seconds. Make sure the ramp range is 0.1. Turn up or down the current limit to the desired value. Note: 10 turns = 100 amps. Turn the key to the heater off position. Take the key out and wait 15 seconds. Put the ramp range to 10, and the toggle switch down. The magnet should now be at a new field in persistent mode.

Setting up the Probe

To place an oscillator in the vice, insert a screw driver between the vice jaws and twist. Watch that no wires are being severely pinched. Unscrew the electrodes away from where the oscillator sits because if the electrodes protrude too much, they will break the oscillator when the jaws close. If the electrode has to be moved a lot, it may be necessary to unsolder the C1 coax from the electrode.

The C1 coax should be spliced with ultra–low–noise coax to reduce cross talk between the drive and pick-up cables. A few inches of C1 cable should be left near the head and tail of the probe, but the middle section (about 1 yrd) needs to be changed. The cross talk may be the cause of the large and intermittent offsets as the cables flex and cross each other. Originally, the offsets were very small, and the 500 nV scale on the lock-in was useable. This deteriorated to a point where the differential mode of the lock-in needed to be used. At this time, the offsets were on the order of 50 μV with a 1 V drive. The electrodes were replaced with electrodes that had 2850FT set between the inner and outer conductor. This brought the offsets down so that a 20 μV scale could be used with a 1 V drive. More can be found in Chapter 2 in the capacitive detection section.

Slip the oscillator in place with the gold side towards the electrodes. Gently twist the screwdriver and remove. Tighten the set screw which presses the vice against the springs. Adjust both electrodes; if the gap is smaller than 0.1 mm, it may close upon cooling, especially if the electrode and oscillator are not parallel. Be aware that the gap may shrink when the 0-80 screws that lock the

electrodes in place are tightened. Resolder the electrode cables, if necessary, and also the high voltage line. By slipping pieces of wire of a known diameter in the top and bottom of the gap, the gap size can be determined to within ±0.02 mm. The oscillator stage can be tilted with the four supporting screws of the top stage. Generally, the oscillators will develop a small amount of tilt when the epoxy sets, ~1°, so tilting the stage is not always recommended. By pinching an index card and transparent ruler between the thumb and index finger, the total oscillator tilt can be measured by lining the edge of the card with the probe shaft and the ruler with the oscillator edge as viewed from the side.

A 15 mil metal o-ring made of 96% lead and 4% antimony from Canfield Inc. is used to seal the can. Pump out the probe using the roughing and diffusion pump. This may take an hour if the probe has been open for a while. Back-filling with dry helium will speed up the process. It is best to vent the probe with dry gas to shorten following pump downs. The zero of the gauge is around 15 mTorr. The exchange gas is put in last. Back-fill with helium to 1000 mTorr, valve off the probe, pump-out the line, and rough-out the probe to 150 mTorr by cracking the valve. The probe is ready for the Dewar.

The sample is glued to the head of the oscillator as far along the head as possible because this increases the effective torque on the oscillator produced by the sample. Thus the threshold of the minimum detectable force is decreased. The position and orientation along the head needs to be recorded. A photograph is a good way of documenting this. Superglue is soluble in acetone, dries quickly but not so fast as not to be able to put the crystal on. Furthermore, the crystal has never popped off with temperature cycling. The big problem with this glue is that

the crystal sometimes breaks upon dissolving the glue. Very little glue should be used to prevent this. With a sharp Q-tip, paint a small uniform area of glue. Drop the crystal with the vacuum tweezers. Poke the crystal into place; if it seems stuck don't push. Redissolve by placing only the oscillator head in acetone. Try again. Untwinned crystals will break the easiest as they have undergone huge stresses during detwinning. No part of the crystal should overhang the oscillator edge unglued because it will break—there will be a mismatch of thermal expansion coefficients along the edge. Different glues have been tried from Duco cement to GE varnish. Duco dries too fast and does not cycle as well as superglue. GE dries too slow. So until a gentler glue can be found, it'll be Superglue. One possible solution to stop the sample breakage of large overhanging crystals is to glue the crystal to a small section of a cover slide.

The crystal is not always placed on the oscillator face ($H \perp c$); for one run, it was placed on the top ($H \parallel c$). The beveled edge of an old oscillator can be cut with the diamond saw or cleaved, then the non-beveled edge polished flat with the metal clip/ epoxy system. Start with the roughest grit paper and use machine oil for a lubricant. A small piece of expendable material should be placed in the epoxy with the shard as an indicator of the depth polished off. The beveled shard can be epoxied with 2850FT to the top of an oscillator to make a flat stage for samples. By holding the oscillator head with one pair of tweezers and the shard with the other, the shard may be popped off without breaking the oscillator. Keep the shard small so as not to kill the Q and shift the frequency too much. A 100 μg crystal at the edge of the head will drop the frequency by 100 Hz and freezing to 100 K will increase it by 30 Hz. A shard of 0.0015 g epoxied near the edge

caused the frequency to shift down 200-400 Hz and the Q to decrease by a factor of four.

Taking the Data

Most of the coax cable is labeled and is not to be removed for any purpose. The "Quick Record" Labview program should be selected for manual data taking. This program currently relies on the Keithly DMV 195. Ultimately this should be replaced with the Keithly DMM 199; this will require a change in the GPIB address and in some of the commands sent. Additional commands specifying the channels will also need to be sent. This would be useful because both phases of the resonance curve could be recorded and the field also. The DMV 195 needs to be connected to the front panel output of the lock-in amplifier. The computer needs to be connected to the temperature controller, the frequency counter, and the DMV 195. Once in the program, carefully specify the path and file for saving the data. Flip the toggle switch on (up) on the virtual instrument panel and click the LabView start arrow on the title bar (Fig. 3.17). Click on the button to record a point.

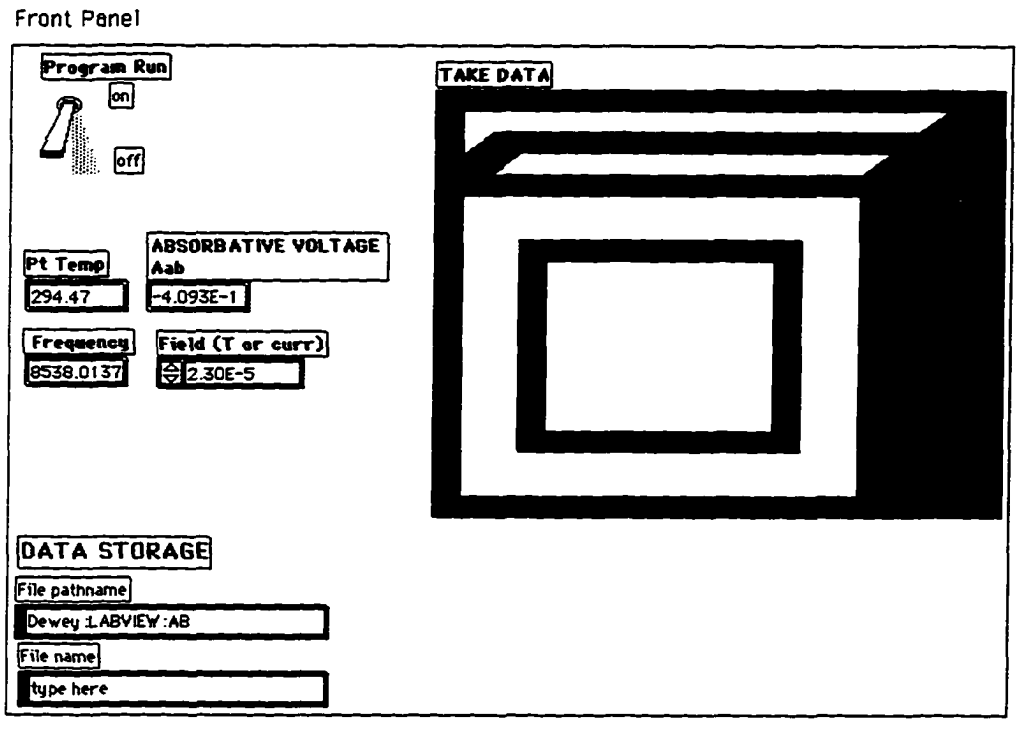

FIG. 3.17. LabView data collection front panel.

One should try to remain on resonance continuously. Ideally, points are taken when the elastic part of the amplitude is zero; realistically, they are taken when A_{el} is within ~1% of A_{ab}. Moving off and on resonance should be avoided because it is necessary to remain on the resonance for several seconds before the value reaches its true maximum. Each run takes approximately 3 hours in going from 100 K to 70 K. The needle valve only needs to be opened between half and three-quarters of a turn when cooling. Try to work out a consistent pattern of timed temperature decreases on the controller so that hysteretic differences between runs do not occur. A 10 K difference in the set point and actual temperature usually produces a sufficient gradient for moderately quick cooling.

When going through a transition a gradient between 5 K and 3 K is more appropriate. These temperature differences are actually dependent on the conductivity of the probe at various temperatures, so they should only be used as a rough guide. The most critical measurements should be performed at the beginning of the week as the needle valve will start to develop some blockage with time and control becomes more finicky. For YBCO, one should probably warm back to 105 K between each run. The probe heater can be used to speed this up. Do not exceed 0.1 A of current through this heater or it may burn out. When above the freezing point of oxygen, pump out probe every few days and put in fresh helium exchange gas. Be consistent with the amount, usually 150 mTorr is enough. See the previous chapter to see the affect of pressure on the oscillator.

When doing field sweeps, the temperature must be fixed. Stabilizing the temperature to within 0.1 K is possible. Stabilizing to a specific temperature is not as easy. One must approach the target temperature slowly, stop a few degrees above it and let the temperature over shoot carry one to it. Because the conductivity of various parts of the probe change at different temperatures, this is hard. Once the correct temperature has been hit, it becomes a balancing act. If the flow from the needle valve is not uniform, it will also be hard to remain stable; once again these runs should probably be done near the beginning of the week.

Clear and consistent recording of data and the conditions of each run is of extreme importance. This cannot be over emphasized as it will save time later. Even checking and rewriting conditions that have not been changed between runs must be done because unintentional changes do occur; one may not remember the

exact conditions three months later, or another person may be looking at the data. For oscillator runs, this is a minimum of the information that should be recorded: frequency, temperature, absorptive amplitude (these are recorded by the LabView program), the data file name, the field, the crystal orientation, the pick-up electrode gap, the sample name, mass, and position, the angle of the oscillator, the sensitivity and dc offsets of the lock-in, the exchange gas pressure, the oscillator bias voltage, the ac drive magnitude, the starting and ending time, the date. The Q of the oscillator at room temperature must be known before the run as well as the conditions under which it was taken. This is done using the frequency sweep program and knowing the gap, dc bias, ac drive magnitude, pressure. When determining the Q at RT, try to use a gap, bias, and pressure that will be used in the experiment. Occasionally the Q can be measured before the sweep at a low temp, ~100 K, if the temperature is stable. This can be very convenient because the exact Q for the experimental condition at hand can be measured with no conversions to account for differences in set up as with the room temperature measurement. A few things that should also be checked before each field or temperature sweep are as follows: the time constant of the lock-in, the driving wave form, the set points for ramping down the temperature, the NEW name of the file for the new data (if the name is not changed, LabView will over write the previous file). It would probably not hurt to make an Excel "fill in the blank" spread sheet with all of these items.

When starting the run, zero 4 or 5 Hz above the starting resonance, then check the offsets. Check these at the bottom temperature also. Sometimes it is necessary to re-zero during the run—do not do this during the transition! Select a

lock-in sensitivity that puts the signal on a scale where it is not more than 60%. Do not forget to set the phase shift, which should be determined before the run as explained earlier. The phase offset does not appear to be dependent on the temperature or gap, but rather the electronics/ oscillator. If there is an arc from the oscillator to the electrodes, the phase can temporarily shift. Beware of "data glitches," these are sudden jumps in the amplitude and frequency. Usually, the frequency does not change by more then a couple hundredths of a Hertz. These jumps are believed to come from cracks where tensions built up and release like mini earthquakes. The shock of cracking ice on the Dewar has also produced similar effects. In fact, at the very low amplitudes, loud people in the room produce registrable jumps in the lock-in; however, these jumps relax to the pre-stimulus state once the noise is gone, so it is best not to respond to them. Filling the Dewar with LN_2 should not be done during the sweep.

The voltage signal to the lock-in is not a Q, but is a voltage which is proportional to the physical motion, pick-up gap, and oscillator bias. This voltage signal will be referred to as the amplitude of the oscillator although it is technically a quantity proportional to the amplitude as seen in chapter 2. The amplitude of a bare oscillator is dependent on the bias (V_B), drive (V_D), pressure (p), gap, temperature (T). The signal recorded by LabView from the DMV 195 is not the amplitude seen by the lock-in, but rather a value dependent on the scale of the lock-in. This is why it is an imperative that the lock-in scale be recorded. The amplitude is the product of the recorded value, and the scale (i.e. 5 μV) divided by 10 V. To transform the amplitudes to Q's, the Q and signal size for a given set of conditions must be known. Because $Q \propto$ Amplitude,

$$\frac{Q(V_{B1}, V_{D1}, p_1, gap_1, T_1)}{A(V_{B1}, V_{D1}, p_1, gap_1, T_1)} = \frac{Q(V_{B2}, V_{D2}, p_2, gap_2, T_2)}{A(V_{B2}, V_{D2}, p_2, gap_2, T_2)} \qquad 3.13$$

If the V_B's, V_D's, p's, gap's are kept the same between the "1" and "2" indexed variables or their relative dependence is known, the Q at any temperature can be found from the old known Q. The amplitude dependence on V_D is linear for driving voltages under 1 V given a 0.25 mm gap. The amplitude dependence on V_B is roughly quadratic (Fig. 3.18).

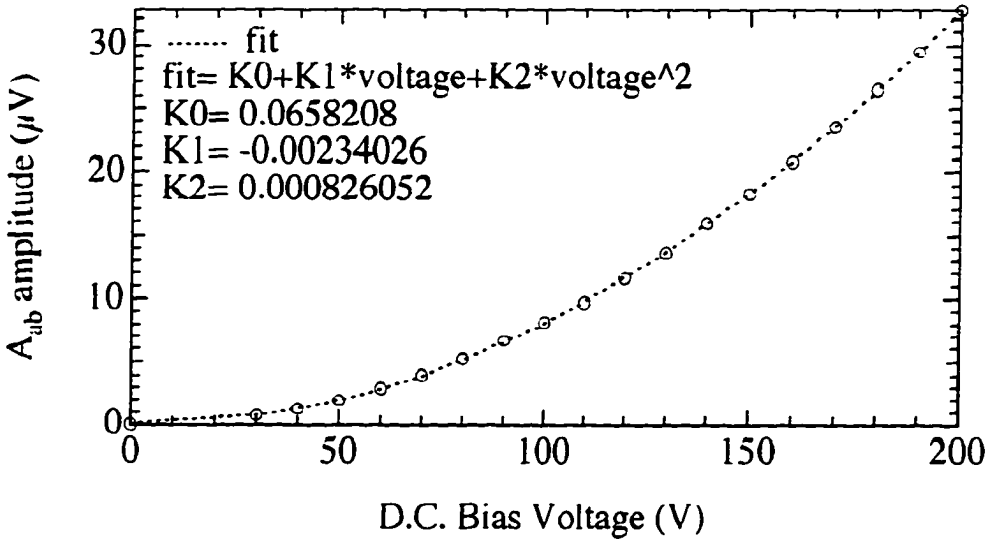

FIG. 3.18. Dependence of amplitude on bias voltage.

The helium exchange gas, used to facilitate temperature equilibration, will decrease the oscillator amplitude, so using more than a couple hundred mTorr is unwise. The drop in amplitude is most pronounced in the first two hundred mTorr. The effect of pressure on amplitude is give in Fig. 3.19. The fits are frequency = A0 + A1exp(–A2×pressure) + A3exp(–A4×pressure) where Ai = {8390, –0.12274, 0.00087664, –0.021252, 0.023314} and amplitude = B0 +

B1exp(–B2×pressure) + B3exp(–B4×pressure) where Bi = {7.2687, 6.5952, 0.0019297, 7.0857, 0.015306}.

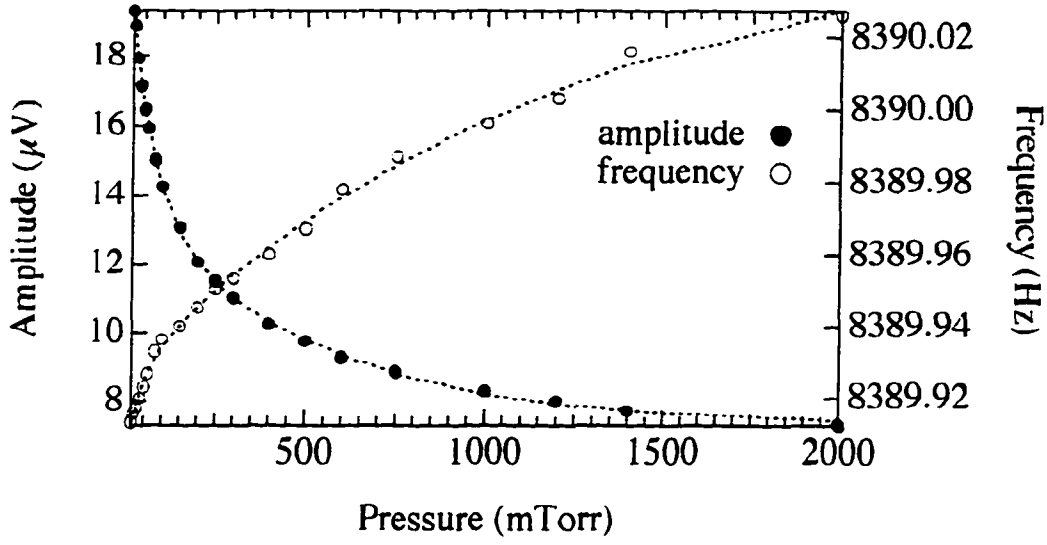

FIG. 3.19. Dependence of amplitude on pressure.

The gap, like V_d, is also assumed to be linear also. For example, suppose all conditions were the same except that a different drive voltage was used, when measuring the Q at room temperature, than was used for the experiment. The new $Q(T)$ would be

$$Q(T) = \frac{A_{.125V}(T)Q(RT)}{\left(\frac{.125}{2.5}\right)A_{2.5V}(RT)} \qquad 3.14$$

If $Q(RT)$ = 42 000, $A_{2.5V}(RT)$ = 22.75 μV, $A_{.125V}(100\ K)$ = 7 μV, then $Q(100\ K)$ = 260 000, where (.125/2.5) × $A_{2.5V}(RT) = A_{.125}(RT)$.

The dissipation, $1/Q$, for the oscillator system is a combination of the crystal effects that are being studied and the background (field and temperature

effects on the bare oscillator) that must be subtracted to give only the crystal effect.

$$\Gamma_{crystal}(H,T) = \frac{1}{Q(H,T)} - \Gamma_{background}(H,T) \qquad 3.15$$

The background is determined by doing a slow temperature sweep and cycling the field between 1 and 8 T; this gives a series of temperature dependent curves for each field. These can be fit with Igor, a program from WaveMetrics, and subtracted from the $1/Q$'s. For the single-side polished oscillators, the amplitude is weakly quadratic with temperature for any field, and the amplitude decreases with increasing field. A table with the quadratic fit coefficients for the single-side polished oscillator amplitudes is given below. Fits for the frequency are also possible by subtracting the pre-transition frequency shift; this is also reason to start the run well above the transition so that there are enough points for a good fit.

H	a (x^2)	b (x)	c
1	.075831	-14.679	1026.5
2	.053168	-11.04	875.32
4	.039784	-8.64061	734.91
6	.030042	-6.4061	574.831
8	.024421	-5.1379	468.02

Table 3.3: Background amplitude fits.

THE SAMPLE AND ITS CHARACTERIZATION

A king without subjects is akin to an experiment without a sample. Much of the early progress on high T_c materials was hampered by a lack of clean and homogeneous samples. As can be imagined, this led to spurious and often contradictory results. However, as experience with the new materials grew, techniques for their synthesis, especially YBCO, developed. Nevertheless, to this day the growing procedures for large rectangular YBCO crystals still entails a dollop of luck and possibly even a hint of witchcraft.

The process for growing single crystal YBCO starts with the drying of the standard high purity reagents Y_2O_3, $BaCO_3$, CuO at 900°C, 120°C, and 450°C respectively. Because single crystals are grown from a flux of excess starting reagents and not from the stochiometrically exact ratios of reagents, as is the case when making polycrystalline sample, some error in the weighing of the starting material is probably tolerable. The error should be kept to a minimum (< 1% by weight) for the sake of repeatability. Five "nines," 99.999%, starting reagents are available from APL Engineered Materials in Urbana, IL—APL may be a subsidiary of Johnson Matthey. The reagents undergo the standard mixing, firing at 906°C, and regrinding that polycrystalline samples see. After the final firing, the pellet, which is ~4 g, is placed in a zirconium stabilized rectangular tray and cooked with the program shown in Fig. 3.20a. These crucibles are sensitive to thermal shock, so sudden temperature changes should be avoided. They can be purchased from McDaniel Refractory for the minimal price of $100+ per tray! The tray should always be located at the same position in the oven so the sample

sees the same temperature during each run. Several possible starting fluxes can be used so long as one can find the correct melting temperature of the pellet, i.e., the peak temperature in the program. Many fluxes from 1-4-10, 1-6-18, to 1-6-30, where the numbers indicate the molar ratios of yttrium to barium to copper, have been tried. Note, should one want to change the program, the melting temperature is lowered by the increase in copper content of the flux. The peak temperature only needs to be sustained for a few minutes to achieve a melt followed by a downward ramp during which the crystals should grow. Once the program is complete and the oven has cooled to below 40°C, the tray can be removed. The crystals do not always form on the surface as is the case for a 1-4-10 flux, but often internally in pockets like the crystals of a geode. Pocket formations are more common for the higher copper content fluxes such as 1-6-30, which has produced the most successful growths for the author. The crystals are extracted by hacking with a scalpel and stored in drierite until enough are collected for an oxygenation run.

The crystals that are grown are not $YBa_2Cu_3O_7$ but rather $YBa_2Cu_3O_{7-\delta}$, thus they need to undergo an extra oxygenation step to achieve the uniform fully oxygenated structure, technically this is $YBa_2Cu_3O_{6.95}$. The crystals are placed in small gold boats, which are in turn placed in a large alumina boat. Because of the tendency of aluminum to substitute itself in place of copper, the crystals cannot be placed directly on the alumina boat surface. Gold also dopes in place of the copper, but it tends to raise the transition temperature rather than lower it as aluminum does. A slow flow of oxygen at atmospheric pressure is fed into the

tube oven over a 4 week period (Fig 3.20b)—the diffusion of oxygen through the crystal is slow!

The actual temperature should be around 520°C for maximal absorption [Jorgenson, 1990; Schleger, 1990]. The resulting crystals should be fully oxygenated and have a transition temperature between 91 K and 93 K with a Δ T on the order of a degree as determined by SQUID magnetometry. Occasionally, some study may require crystals with a sharp transition but which are not fully oxygenated, i.e., a lower transition temperature. Deoxygenated crystals are produced by annealing batches of crystals with partial pressures of O_2 and Ar for various times at 520°C and then quenching the samples in liquid nitrogen. (The tube ovens have a tendency to over shoot the set temperature, so this extra temperature must be taken into account.) An inhomogeneous oxygen distribution in the crystal often results from freezing the crystal in a transient state of oxygen redistribution as can be seen from the broad ΔT. Fortunately, the crystal does anneal, becoming homogeneous at room temperature as the oxygen redistributes itself over a couple of days following the quench [Veal, 1990]. Once the redistribution has occurred, the T_c of the sample may shift and the transition may sharpen. Unfortunately, the quenching is a rather violent process during which the surface of the crystal may become damaged also. Such damage is apparent from the hazy appearance of the surface.

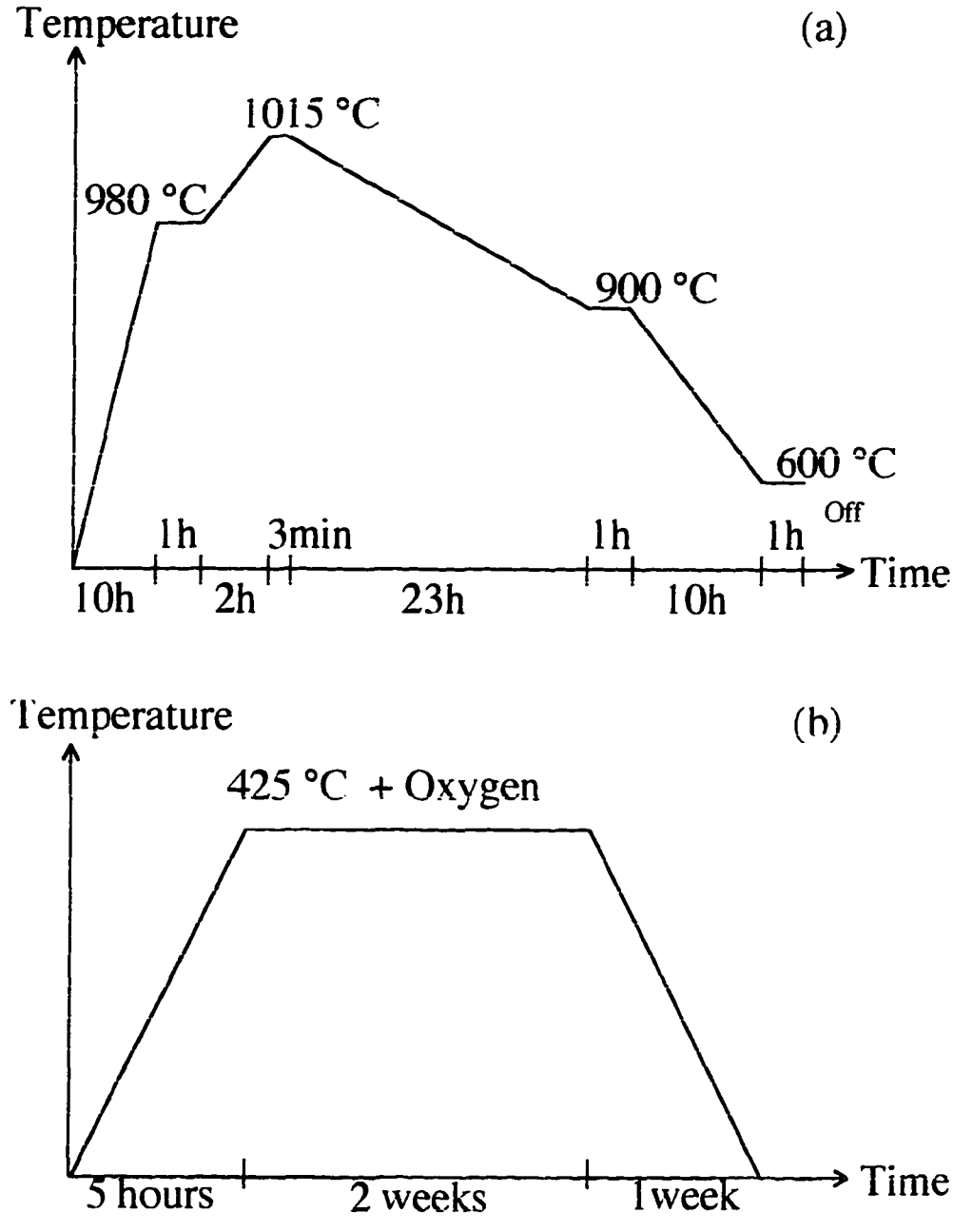

FIG. 3.20. Oven profile for (a) growing single crystals and (b) oxygen annealing. The 425°C assumes a 95°C temperature overshoot.

YBCO crystals grown from a flux are normally twinned. A twin in YBCO is a crystal defect in which there is a 90° rotation of the a-axis and b-axis so more than one domain exists. Orthogonal chains thus intersect along a plane, the twin boundary. Detwinning forces oxygen in the chain parallel to the detwinning force to hop over to a copper chain perpendicular to the force. This destroys one chain and adds to a perpendicular chain, thus for example, an a-axis domain is converted to a b-axis domain (Fig. 3.21).

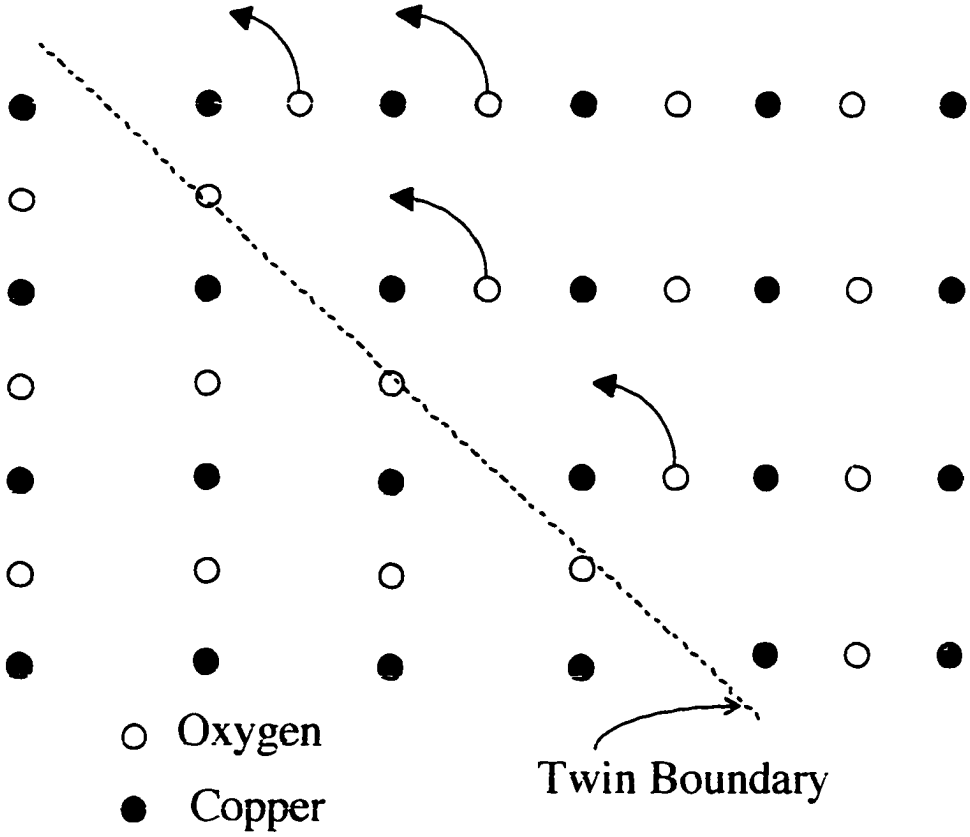

FIG. 3.21. Oxygen hopping during detwinning.

The twin boundaries are visible under a polarized light microscope as fine lines as shown in Fig. 3.22a.

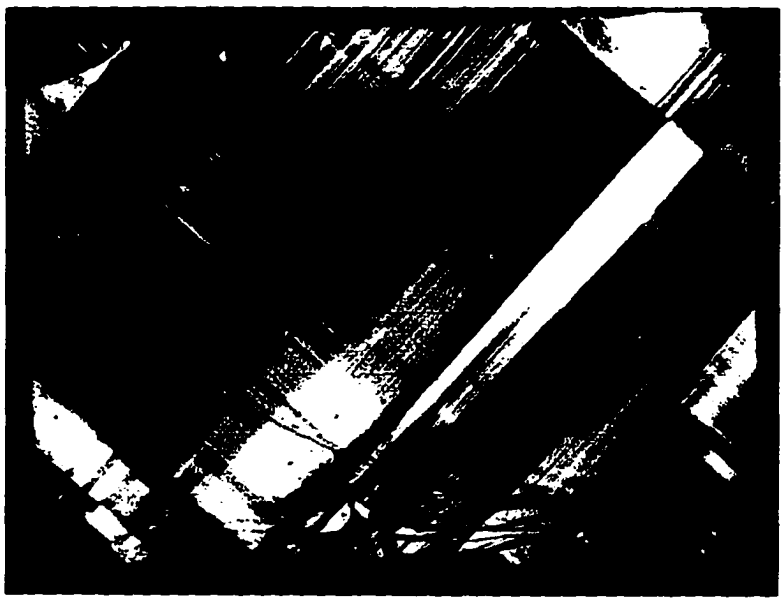

FIG. 3.22a. Heavily twinned crystal. Photographed in polarized light. Courtesy of Chris Kuklewicz.

A partially detwinned crystal is shown in Fig. 3.22b where a few isolated twin boundaries remain.

FIG. 3.22b. Partially detwinned crystal. The center is untwinned while edges remain twinned. Photographed in polarized light. Courtesy of Chris Kuklewicz.

Unless one is trying to study the effects of twin boundaries, they may need to be removed so as not to mask other effects such as the melting transition as will be discussed later. The detwinning process is an art; too much pressure and the crystal will break, too little and it will not detwin. Crystals with rectangular geometry or at least two parallel sides work best. The detwinning apparatus is drawn in Fig. 3.22 and is similar to the one used by the Welp's group at Argonne National Lab [Welp, 1989].

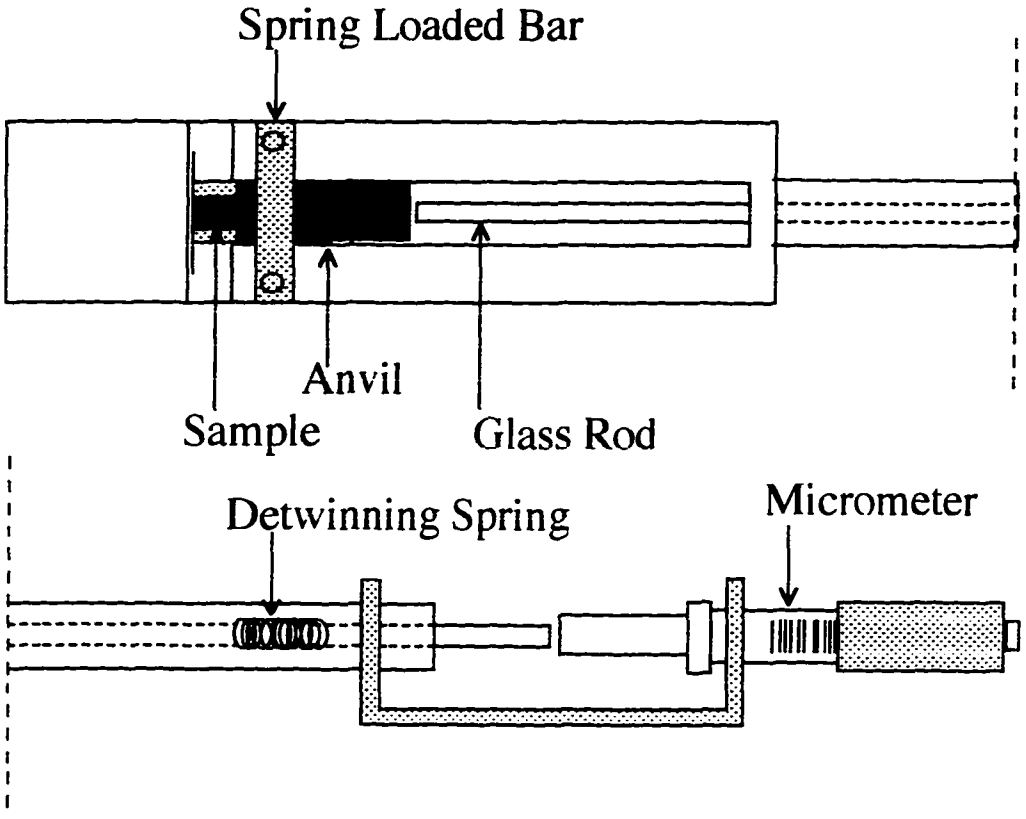

FIG. 3.23. Detwinning apparatus.

In it, the crystal is compressed between a silicon anvil and glass cover slide. The anvil is held down by a spring loaded metal bar. In order to reduce friction, a silicon nitride shim is used to separate the metal and silicon. The bar springs should have just a enough tension to hold the bar down so that it does not ride over the sample when applying the detwinning pressure—finding this tension out just takes experience and will depend on the condition of the anvil edge; this pressure is roughly not more than a few turns of the screw. The anvil is pressed into the sample via a spring-loaded rod that is, in turn, compressed by a

micrometer. This "detwinning spring" has a spring constant of approximately 0.16 N/mm at room temperature, so a few millimeters of compression will usually be enough to produce the MPascals needed for detwinning given the small ~1 mm × ~30 mm cross sectional area of the crystals. All the pieces should be wiped down before each run to reduce friction. The temperature of the run must remain below 450 °C or oxygen will be lost [J. Giapintzakis]. Also, pressure should only be applied after the peak temperature has been reached, otherwise the surface will degrade. After 24 hours of pressure, the sample can be quenched and the pressure released.

A few helpful notes on making a SQUID sample holder are in order, especially because the sample should be carefully checked with the SQUID magnetometer before running any experiment. Cylindrical sample holders are best for easy background subtraction. First, Plexiglas can be paramagnetic or diamagnetic. Plexiglas has a tendency to crack if cleaned with alcohol—don't even think about acetone. Temperature cycling may also cause the Plexiglas to crack. For these reasons, the author found Teflon to be a good alternative. There are a couple of issues with Teflon, but these are easy to work around. Teflon is a soft material, and if put in a quartz tube (instead of a straw) and warmed from a cold temperature suddenly, the quartz may warm faster leaving the Teflon in a state of partial compression from the cool down, enabling the Teflon holder to slip out of the tube. This problem should not occur if a good snug fit is made between the holder and tube. If a straw is used, two diametrically opposite pin holes can be made below the sample holder; this will ensure that the holder will remain in place. The holder should have a hole so oxygen (paramagnetic) does not become

trapped inside. Ideally the holder would have no signal at any field or temperature. Since no such non-magnetic material exists, the best one can do is to cancel the net moment using some paramagnetic material with a diamagnetic one. There are several ultra high purity (at least 99.99%) paramagnetic metals that work to cancel the signal from Teflon. Note, avoid metals with ferromagnetic impurities. By pressing high purity aluminum pellets with pressures up to 15 000 psi, one can make flat sheets. The pellet is placed in a latex glove to prevent iron contamination from the press. A disk can be cut from the sheet with a stainless–steel "cookie cutter" made by machining an edge on a tube. The knife edge should be machined such that the inner diameter of the tube remains constant and the bevel slopes to the outside. This pressing/cookie cutting technique works for soft metals only. Other materials that come in sheets or foils also work, i.e., tantalum foil. Foils are good for fine–tuning, the cancellation if sanding is to be avoided. A table of some susceptibilities at 294 K is given below. * Data from [CRC]:

Material	Susceptibility ($\times 10^{-6}$ emu/mole)
Teflon	-0.21
*Aluminum	+16.5
*Tantalum	+154
Plexiglas	-0.47
*Platinum	+201.9
*White Tin	+3.1

Table 3.4. Material Susceptibilities.

The SQUID seems to have an easier time fitting the sample holder when the holder has a diamagnetic/ paramagnetic/ diamagnetic structure, i.e., a Teflon holder, a tantalum plug which fits in the holder, and then a small Teflon lid; this symmetrical layering is recommended in addition to the standard advisory for a cylindrically symmetric holder. The whole structure should be no taller than 3 or 4 mm.

Chapter 4: Background

INTRODUCTION

This is a just a few–page chapter to explain a few terms that are used in following chapters. It is largely a cursory review of several sections from Tinkham's book [Tinkham, 1996]. These terms are used to describe various parts of the H–T phase diagram for high–temperature superconductors. The concepts to be considered are: the flux–flow regime, irreversibility, the melting line, and the thermally activated flux–flow regime.

From the Lorentz force law, one knows that a vortex in the presence of a current will experience a force:

$$\mathbf{f} = \mathbf{J} \times \frac{\Phi_0}{c} \qquad 4.1$$

which will produce a velocity component for the vortex that is perpendicular to the current, **J**. This transverse motion of a flux line will induce an electric field parallel to **J**. Now $\mathbf{J} = \mathbf{E}/\rho$ (Ohm's law), so this motion acts as a resistance,

producing dissipation. If there is no pinning or the pinning is very weak, one can ignore it and equate the resistive force to a drag term, η, proportional to the vortex's velocity, v_L:

$$J\frac{\Phi_0}{c} = \eta v_L. \tag{4.2}$$

If one now uses Ohm's law to replace J and then applies Faraday's law, the flux flow resistivity is found to be

$$\rho_f = B\frac{\Phi_0}{\eta c^2}. \tag{4.3}$$

Much of the microscopic physics is actually wrapped up in η. Bardeen and Stephen [Bardeen, 1965] made a model in which a fully normal core of radius ξ produces dissipation by ordinary resistive processes. This theory results in

$$\eta = \frac{\Phi_0 H_{c2}}{\rho_n c^2} \tag{4.4}$$

where H_{c2} is the upper critical field and ρ_n is the normal state resistivity. For a superconductor with weak pinning, the 1st order transition from an Abrikosov lattice to the flux flow state is denoted in H–T phase space by the melting line.

If pinning sites are present, as invariably there are, the vortex can be trapped on these locations. The trapping can be expected because the pinning site produces a spot of lower free energy relative to its surrounding; basically one has a local well. Should a vortex be in one of these sites, the vortex can escape if it has enough thermal energy, ~kT. Given that the pinning is sufficiently strong so that the flux does not move in response to the driving force of the currents alone, it is still possible for flux lines to hop around between pinning sites if there is enough thermal energy—this is the thermally activated flux flow regime. If this is the case, the driving force will influence the direction of the jumps. In essence

the thermal energy slows the normal flux motion to that of a creep, hence the term flux creep. In Anderson–Kim flux–creep theory [Anderson, 1962], the jumping is assumed to occur in bundles of flux and is characterized by a jump rate,

$$R = \omega_0 e^{-\frac{F_0}{kT}} \qquad 4.5$$

from which the creep rate can be calculated. Here, ω_0 is some parameter that describes the flux line, F_0 is the barrier energy given by

$$F_0 = p\frac{H_c^2 L^3}{8\pi}. \qquad 4.6$$

L is the length of the flux bundle and p is the fraction of modulation of the condensation energy in a volume L^3 that is available as pinning energy; p is << 1. Because the coherence length is much smaller for the high–T_c materials, p is smaller and hence the pinning barrier size is less than for conventional superconductors, and the flux jump rate is much higher for the high-T_c materials. Note, the flux moves in bundles because the repulse range of individual flux lines, λ, is large compared to the distance between lines in this model. All in all, the flux creep for some drive force of magnitude, α, would cause a dissipation per unit volume of

$$P = \alpha v_0 e^{-\frac{F_0 - \alpha L^4}{kT}}, \qquad 4.7$$

where v_0 is the creep velocity with no pinning barrier. The resistivity will exponentially drop as temperature decreases.

The flux pinning and flux jumping as determined by group motion of vortices and available thermal energy can cause hysteretic effects in magnetization measurements given that measurements occur over a short time. Given enough time, magnetization measurements would theoretically relax to the

same value. The line in H–T space where irreversibility sets in is called the irreversibility line; it separates the flux flow and thermally activated flux flow regimes and is indicated by the peak in the oscillator dissipation. (Note, this line does not denote a 1st order phase transition.) Because the irreversibility line separates two regions that have very different resistivities, the line can also be defined as the locus below which the resistivity drops several orders of magnitude. The theoretic changeover between these two regions is still not well understood for the high-T_c materials.

Chapter 5: Flux Diffusion Modes

INTRODUCTION

Over the last decade, techniques utilizing vibrating reeds [De Long, 1992] and their closely related cousin, torsional oscillators [Gammel, 1988], have been applied to studying the vortex dynamics of high temperature superconductors, in particular, dissipation. Because of the added complexity of a high transition temperature and the large number of defects in these materials, an initially speculative phase diagram of vortex dynamics was developed [Nelson, 1989]. Although many of the theories for vortex motion, dissipation, pinning and other quantities associated with vortex motion have been clarified and fleshed out [Brandt, 1991; Blatter, 1995], further experimental testing is needed. The thermally activated flux flow (TAFF) and flux flow (FF) regime have been well established [Palstra, 1988; Golosovsky, 1992]; however, even here there is still

effort in establishing the correct temperature and field dependence of the resistivity [Qiu, 1993].

The explanation for dissipation in high-T_c superconductors (HTSC's) from oscillator-type data is still somewhat vague or non-existent. Multiple peaks and knees are observed, the origin of which is most likely related to both sample geometrical factors as well as materials properties such as pinning [Brandt, 1992]. Further efforts are increasingly turning to include the effects that twin boundaries have on the pinning of flux [Kwok, 1992; Fleshler, 1993]. The twins are highly anisotropic and produce a controlled pinning potential for experimentation [Crabtree, 1995].

For ac measurements such as dissipation studies using torsional oscillators, there is believed to be a characteristic time, τ, that is proportional to the diffusivity such that when $\tau = 1/\omega$, dissipation is maximized [Brandt, 1992]. The diffusivity is dependent on the pinning potential, $U(T,B)$; hence, the dissipation peak is a probe of this potential.

In this chapter, dissipation experiments in which different orientations (parallel and perpendicular to the field) of the c–axis and of the twin boundaries are considered to test and extract parameters from existing models (Fig. 5.1). Specifically, geometrical dimensions of the crystal are looked at to see if they can account for the shape of the dissipation curves seen here and whether the twin anisotropy plays any role.

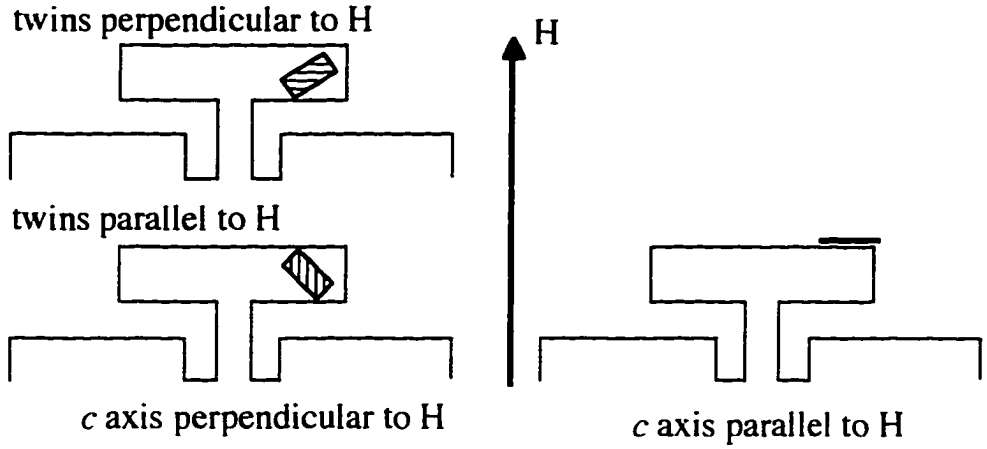

FIG. 5.1. Possible orientations of the YBCO crystal used in these experiments.

EXPERIMENTAL

Single–crystal $YBa_2Cu_3O_{7-\delta}$ crystals were grown from a flux in zirconia crucibles and oxygenated as described previously [Phelps, 1994]. A rectangular sample was chosen from the batch. The sample used had an area of 1.38×0.82 mm^2 and mass of 192 μg. The 10% – 90% transition width of the sample was 1 K with the transition onset at 92 K as determined by SQUID magnetometry. The sample was glued 3.5 mm out onto the head of a single-crystal silicon double–torsional oscillator that had a frequency of 8×10^3 Hz and Q of 300,000 at 100 K [Kleiman, 1985]. A frequency sweep of the drive voltage gives the resonance curves from which the Q at room temperature, ~100000, can be found. The oscillator is kept on resonance as the temperature is lowered. The temperature is lowered from 100 K to 60 K at a rate of 1 K every 5 min and slowed to 1 K every 10 to 15 min near the transition.

THEORY

Dissipation in general

The dissipation, as defined by $1/Q$, is what will usually be referred to. The dissipation for the oscillator alone is measured as a function of temperature and field; this is the background dissipation and is subtracted out to give the dissipation of the superconductor alone, as discussed in Chapter 3. As for any damped oscillatory system, the dissipation can be written as

$$\frac{1}{Q} = \frac{1}{2\pi} \frac{E_{dissipated\ per\ cycle}}{E_{ave}}. \tag{5.1}$$

Because the measuring time constant is on the order of 300 ms and the frequency of the oscillator is ~9000 Hz, it is reasonable to use the time average of the instantaneous power dissipated. From [Brandt, 1992], the power per unit volume is

$$P = \frac{\omega B_s^2 |\chi''|}{2\mu_0} \tag{5.2}$$

where B_s is the magnitude of the ac field that the sample experiences, χ'' is the imaginary part of the susceptibility, and ω is the frequency of the ac field—i.e., the resonant frequency of the oscillator. The total energy is primarily the energy stored in the head of the oscillator as $\phi_{max(head)} >> \phi_{max(wings)}$, where ϕ is the angular displacement of the respective part. The difference in the angular displacements is a result of the difference in inertia between the head and wings, which is about 1:33. The total energy then becomes approximately:

$$\frac{1}{2}\kappa\left(\phi_{max(head)} - \phi_{max(wings)}\right)^2 + \frac{1}{2}\kappa\phi_{max(wings)}^2 \approx \frac{\kappa\phi_{max(head)}^2}{2} \tag{5.3}$$

where κ is the torsional constant and can be written in terms of the head and wing inertias:

$$\frac{2\omega^2 I_{wing} I_{head}}{2I_{head} + I_{wing} + \sqrt{4I_{head}^2 + I_{wing}^2}} \tag{5.4}$$

Equation 5.4 is merely the solution for the upper resonance of a two–mass–two spring oscillating system where the springs are of equal stiffness. For simplicity, this will be called $\omega^2 I_{eff}$. Substituting the dissipated energy and total energy in Q yields:

$$\frac{1}{Q} = \frac{2\pi}{\omega^3 I_{eff}} \left[\frac{\omega B^2 V |\chi''|}{2\mu_0} \right] \tag{5.5}$$

where V is the sample volume and B is now the applied field.

Tilting & Misalignment

The applied field is along the axis of the Dewar and is also parallel to the axis of rotation of the untilted oscillator. Because the crystal is glued to the face, the oscillator must be tilted by some small angle, θ, so that the crystal sees an effective ac field produced by its motion (Fig. 5.2).

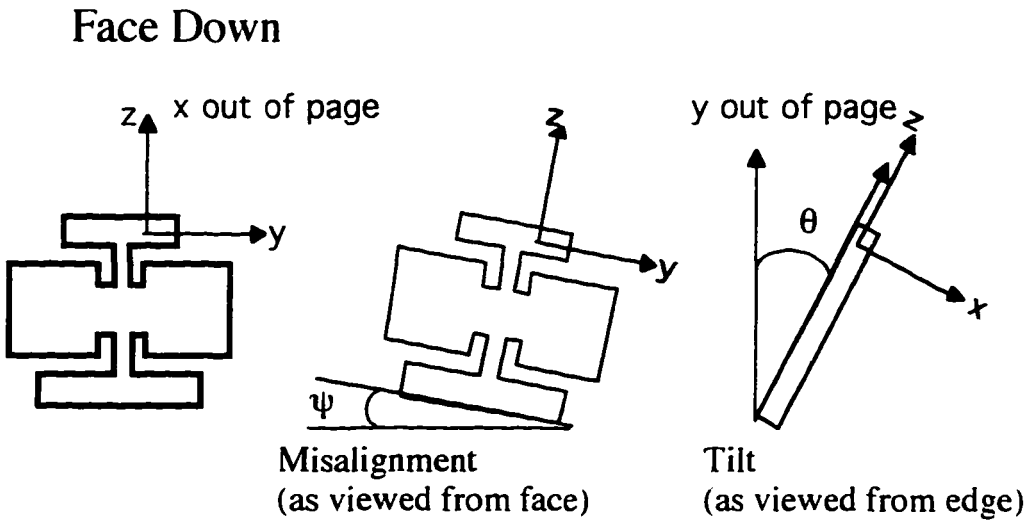

FIG. 5.2. Example of the oscillator rotations for the Face Down position with misalginment AND tilt.

The oscillator could be tilted by θ around the x axis (edge down; ED), or around the y-axis (face down; FD). This does not preclude the possibility that there was a pre-existing tilt already in the perpendicular direction, ψ, (i.e., if the oscillator was tilted around the x axis, it may have already had a small misalignment around the y axis). For this study, θ was set to $3^\circ \pm 1^\circ$ with less than 1° of pre-existing misalignment, ψ, in the perpendicular direction. The coordinates shown are in the reference frame of the undriven oscillator; when the oscillator is driven, they do not move with the oscillator.

By applying a series of rotations, the effective field that the superconductor experiences may be extracted. Rather than rotating the oscillator to find the field that the tilted oscillator sees, the field is rotated in the opposite direction. So the first rotation is to account for misalignment, the second to produce a tilt, and the third is to produce the ac field, i.e., a time varying rotation,

$\phi(t)$, which is applied around the z axis. Thus, three rotations applied to H for the face down and edge down configurations respectively are

$$H_{total} = R_z(\phi(t))R_y(\theta)R_x(\psi)H_{cryostat}, \tag{5.6}$$

$$H_{total} = R_z(\phi(t))R_x(\theta)R_y(\psi)H_{cryostat}. \tag{5.7}$$

$H_{cryostat}$ is taken along the z axis, and R_{axis} refers to the 3 × 3 rotational matrix around the subscript axis. Using $\phi(t) = \phi_0 cos(\omega t)$, for small angles, H_{total} in terms of the ac and dc fields for the two orientations becomes, and setting $H_{cryostat}$ = H yields

$$H_{total(FD)} = \begin{pmatrix} H\sin\theta\cos\psi - H\phi_0\cos\omega t\sin\psi \\ -H\phi_0\cos\omega t\sin\theta\cos\psi - H\sin\psi \\ H\cos\theta\cos\psi \end{pmatrix}, \tag{5.8}$$

$$H_{total(ED)} = \begin{pmatrix} H\sin\psi - H\phi_0\cos\omega t\cos\psi\sin\theta \\ -H\phi_0\cos\omega t\sin\psi - H\cos\psi\sin\theta \\ H\cos\theta\cos\psi \end{pmatrix}. \tag{5.9}$$

Second order terms, $O(\phi_0^2)$, have been dropped. This "theta", the angle between the axis of the Dewar and the axis of rotation, must not be confused with the "theta" used later for the angle between the field and c axis of the crystal.

Sections of the dissipation curves

For low amplitude motion, the dissipation curves showed several types of structure other than the usual smooth single peak. Starting above the transition and moving downward, it should first be noted that there is no apparent melting transition as one goes from the normal state to the upside of the dissipation peak. The melting temperature for various fields is shown in Fig. 5.3 for three different T_c's [Beck, 1992]. This is not surprising as the primary crystal was twinned, and the strong pinning produced by twin boundaries will suppress the melting

transition [Kwok, 1992]. In fact, as few as six twin boundaries have been shown to suppress the first order melting transition [Kwok, 1994]!

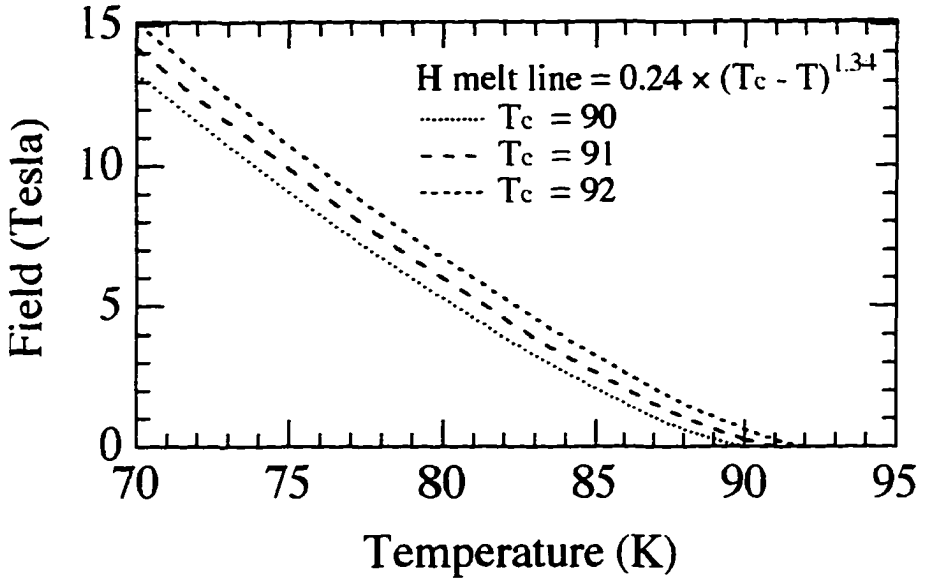

FIG. 5.3. Expected melting line for three different T_c's.

Typical behavior is shown in Fig. 5.4. One may split the overall shape into two main regions: a narrow initial peak near T_c and a broad shoulder at lower T. Note that there is apparent structure even within these two main regions; this structure is discussed in the next chapter. The initial part, nearer the transition, is larger at higher fields relative to the lower–T region.

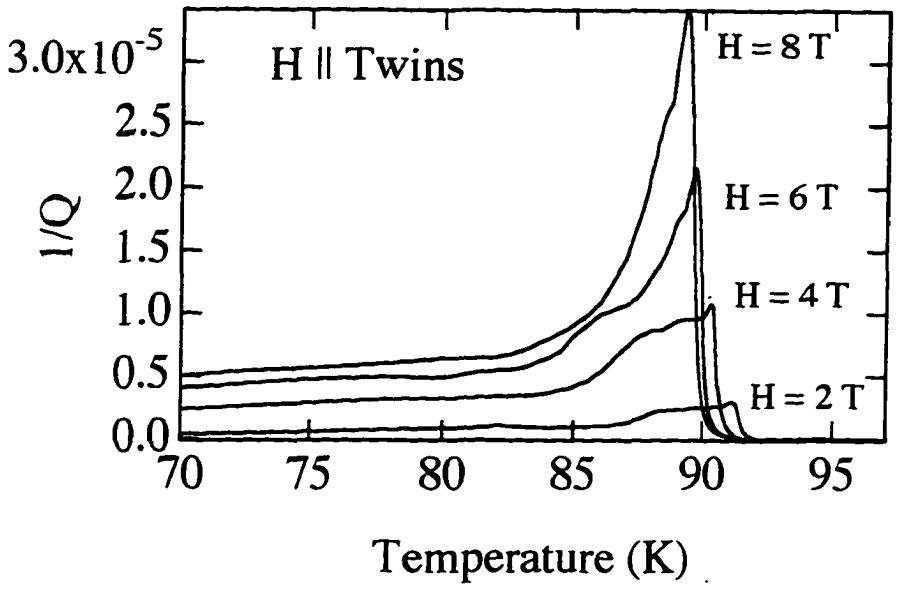

FIG. 5.4. Dissipation curves for twins parallel to the applied field.

The sharp peak can be used to define the irreversibility line. To show this, the temperature for each of the peaks shown in Fig. 5.4 have been graphed against the field at which they were taken (Fig. 5.5). The irreversibility line as determined from ac susceptibility, is in close agreement with the line determined from dissipation. Fitting to the function

$$H_{irr} = A\left(1 - \frac{T}{T_c}\right)^{\alpha} \tag{5.10}$$

yields A = 1899 and α = 1.64. This compares to a value α = 1.33 for the ac susceptibility measurement [Krusin-Elbaum, 1993]. Values as high as $\alpha = 2$ have been found elsewhere. The difference most likely results from a frequency dependence in α. For ac susceptibility measurements, 1 MHz, α increases toward

the oscillator value as the measurement frequency decreases. Note, the oscillator frequency is ~10 kHz.

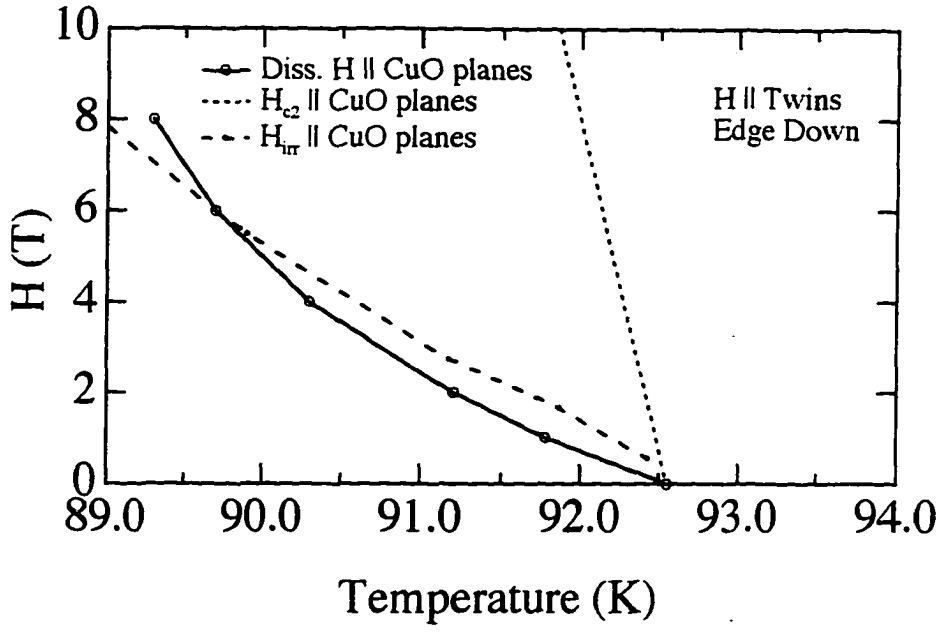

FIG. 5.5. Solid line shows the irreversibility line as determined by dissipation measurement, while long dashes are from ac suseptibility measurements. H_{c2} is added for scale.

Also, the dissipation curves for the two twin directions change form in different ways as a function of applied field. At high field (8 T), the peaks are similar and nearly smooth. As the field decreases, the sharp initial peak dwindles more quickly for $H \perp$ twins (Fig. 5.6). The low-T shoulder is more apparent in the H || twin curves, and becomes pronounced at low fields. The same overall structural changes were seen in both the edge-down and the face-down oscillator orientations.

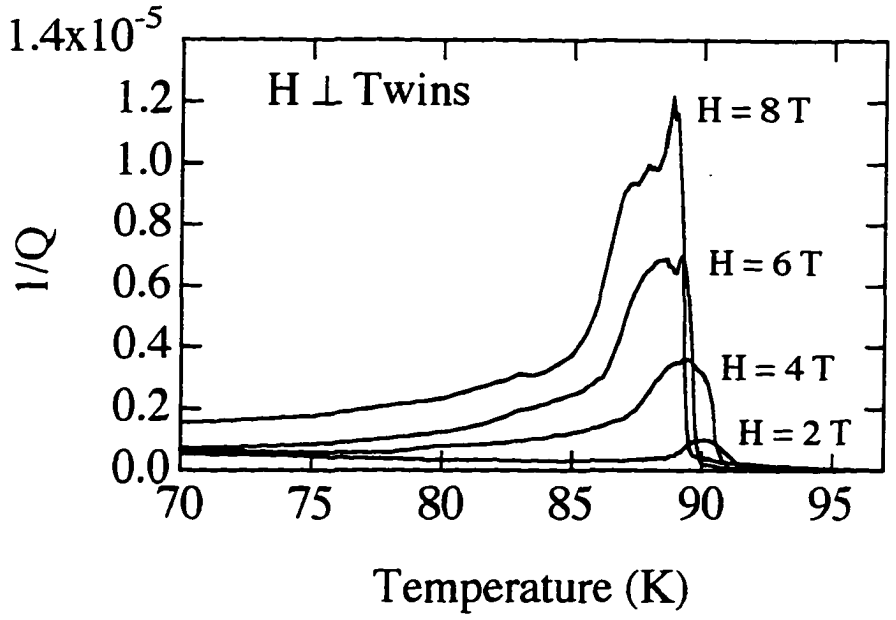

Fig. 5.6. Dissipation curves for twins perpendicular to the applied field. With increasing field, the families of curves generated show different evolutions for the two orientations.

The sections of the curves described above most likely result from flux diffusion modes through the crystal. In order to attempt a fit of Brandt's modes to the dissipation curves, the diffusivity for an anisotropic crystal must be worked out because of the dependence on it.

Diffusivity

For an isotropic superconductor, the flux diffusivity is the same in all directions. Unfortunately the layered structure of YBCO makes it anisotropic; this leads to different values of the diffusivity depending on which direction the flux is driven. To make matters worse, the twin boundaries add an extra symmetry breaking in the *ab* plane of the crystal. Blatter et al. have developed a

method by which theoretical results for isotropic superconductors may be scaled to extend to the anisotropic case [Blatter, 1992]. They apply their technique for one direction as is needed for untwinned YBCO. In this section, the theory has been applied to an extra dimension to account for the effect of the twin boundaries should they produce a sizable role. Although this extra scaling is for the twin boundaries, it could just as easily be used to account for the small anisotropy in the *ab* plane caused by the chains. However, since most of the conductivity is in the plane, this *ab* anisotropy will be ignored for this study. To begin, one first scales the coordinates and vector potential:

$$x = \tilde{x},\ \ y = \varepsilon_t \tilde{y},\ \ z = \varepsilon_p \tilde{z} \tag{5.11}$$

$$\mathbf{A} = \left(\tilde{A}_x, \frac{\tilde{A}_y}{\varepsilon_t}, \frac{\tilde{A}_z}{\varepsilon_p} \right) \tag{5.12}$$

where the tilda are the coordinates of the isotropic case, ε_p is the standard anisotropy for YBCO, and ε_t is a "new" anisotropy to take into account the twins. The coordinates used for this section are shown in Fig. 5.7 for a twinned YBCO crystal. Note, the crystal edges do not necessarily line up with the twins, and the *a* and *b* axis of the crystal definitely do not, but they are at 45°.

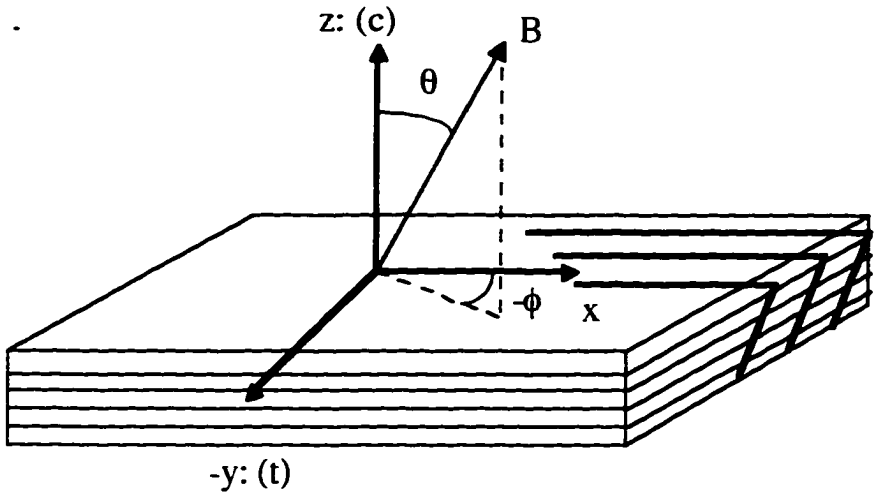

FIG. 5.7. Coordinates for BGL theory. Twin planes are bold. The crystallographic axis is aligned with the z axis.

By taking the curl of **A**, one may find **B**:

$$\mathbf{B} = \nabla \times \mathbf{A} = \begin{vmatrix} \mathbf{i} & \mathbf{j} & \mathbf{k} \\ \dfrac{\partial}{\partial \tilde{x}} & \dfrac{\partial}{\varepsilon_t \partial \tilde{y}} & \dfrac{\partial}{\varepsilon_p \partial \tilde{z}} \\ \tilde{A}_x & \tilde{A}_y & \tilde{A}_z \end{vmatrix}. \tag{5.13}$$

This results in

$$\mathbf{B} = \left(\frac{\tilde{B}_x}{\varepsilon_t \varepsilon_p}, \frac{\tilde{B}_y}{\varepsilon_p}, \frac{\tilde{B}_z}{\varepsilon_t} \right). \tag{5.14}$$

The scaling removes the anisotropy from the gradient terms in the Gibbs free energy and puts it into the magnetic energy term, which is easier to minimize. Minimizing the magnetic–field energy, allows one to determine $\tilde{\mathbf{B}}$ in terms of the external field, **H**, where now **B** = **H** in the original unscaled system. The magnetic energy is

$$G_m = \int d^3 r \frac{B^2}{8\pi} - \frac{\mathbf{B} \cdot \mathbf{H}}{4\pi}. \tag{5.15}$$

Substituting in for **B** and minizing with respect to $\tilde{B}$ results in the following three equations,

$$\partial_{\tilde{B}_x} G_m = \frac{\tilde{B}_x}{\left(\varepsilon_t \varepsilon_p\right)^2} - \frac{H_x}{\varepsilon_t \varepsilon_p} = 0, \tag{5.16a}$$

$$\partial_{\tilde{B}_y} G_m = \frac{\tilde{B}_y}{\left(\varepsilon_p\right)^2} - \frac{H_y}{\varepsilon_p} = 0, \tag{5.16b}$$

$$\partial_{\tilde{B}_z} G_m = \frac{\tilde{B}_z}{\left(\varepsilon_t\right)^2} - \frac{H_z}{\varepsilon_t} = 0. \tag{5.16c}$$

From Eqs. 5.16(a) – 5.16(c), $\tilde{\mathbf{B}}$ can be found;

$$\tilde{\mathbf{B}} = \left(H_x \varepsilon_t \varepsilon_p, H_y \varepsilon_t, H_z \varepsilon_p\right). \tag{5.17}$$

Finally, dotting $\tilde{\mathbf{B}}$ with itself and replacing the x, y, and z components of **H** with the components in terms of the angles shown in Fig. 5.7, one will at last arrive with an anisotropic scaling factor that can be used to change isotropic equations into anisotropic ones.

$$\left|\tilde{\mathbf{B}}\right| = \sqrt{\left(\varepsilon_t \varepsilon_p\right)^2 H^2 \sin^2\theta\cos^2\phi + \varepsilon_p^{\,2} H^2 \sin^2\theta\sin^2\phi + \varepsilon_t^{\,2} H^2 \cos^2\theta} \tag{5.18}$$

Thus,

$$\tilde{\mathbf{B}} = \varepsilon(\theta,\phi)\mathbf{B} \tag{5.19}$$

where

$$\varepsilon^2(\theta,\phi) = \varepsilon_p^{\,2}\sin^2\theta\left(\varepsilon_t^{\,2}\cos^2\phi + \sin^2\phi\right) + \varepsilon_t^{\,2}\cos^2\theta. \tag{5.20}$$

Note that ε_p is $1/\Gamma = \lambda_{ab}/\lambda_c$ = 1/5.5 and that for ε_t = 1, $\varepsilon^2(\theta,\phi)$ reduces to one degree of anisotropy $\varepsilon^2(\theta) = \varepsilon_p^{\,2}sin^2\theta+cos^2\theta$. Other quantities scale also. The volume, V, should scale as $\tilde{V} = \varepsilon_t\varepsilon_p V$ (the poduct of the scaled coordinates); the Gibbs free energy will scale as $\tilde{G} = \varepsilon_t\varepsilon_p G$, and similarly the temperature as $\tilde{T} = \varepsilon_t\varepsilon_p T$ [Blatter, 1992].

For one degree of anisotropy, given that the field makes an angle, θ, with the c axis, the viscous damping term for a flux line moving in this plane is $\eta_1(\theta) = \eta/\varepsilon(\theta)$ while moving perpendicular it is $\eta_2(\theta) = \eta\varepsilon(\theta)$. Once again, this has been shown by Blatter; however, the reference is not available. η is the isotropic viscosity per unit volume in the thermally activated flux flow region (TAFF) and is related to the isotropic resistivity and isotropic diffusivity by $D = \rho/\mu_0 = B^2/\mu_0\eta$. By considering vortices at the angles 0, $\pi/2$ and the angles near them and looking at the motion parallel and perpendicular to the B-c plane and B-t plane (see Fig. 5.7), the viscosities for two degrees of anisotropy have been guessed: There should now be four cases, which are summarized in Table 5.1.

$\eta(\theta,\phi)$	motion ∥ (B–c)plane	motion ⊥ (B–c)plane
motion ∥ (B–t) plane	$\eta_1(\theta,\phi) = \eta\varepsilon(\theta,\phi)$	$\eta_2(\theta,\phi) = \eta\varepsilon(\theta,\phi)$
motion ⊥ (B–t)plane	$\eta_3(\theta,\phi) = \eta/\varepsilon(\theta,\phi)$	$\eta_4(\theta,\phi) = \eta/\varepsilon(\theta,\phi)$

Table 5.1. Viscosity's for various vortex orientations and motion.

These formulae require that $\varepsilon_t > 1$ as compared to ε_p, which is < 1! Also the vortex is assumed to preferentially reside in the twin boundary as opposed to next to it when given the chance. In other words, the twin planes are considered to be the analog of the insulating regions between the CuO_2 planes. For example, given a vortex lying along the y axis ($\theta = \pi/2$ and $\phi = 0$) and an ac field along the z axis, $\eta_3 = \eta/\varepsilon_t\varepsilon_p$. Thus the diffusivity becomes

$$D_{ac}^{\parallel} = \frac{\rho_{ac}^{\parallel}}{\mu_0} = \frac{\rho_{iso}\left(U\varepsilon_t\varepsilon_p, T\varepsilon_t\varepsilon_p\right)}{\mu_0 f(\theta,\phi)}, \tag{5.21}$$

where $f(\theta,\phi)=\varepsilon(\theta,\phi)$ or $1/\varepsilon(\theta/\phi)$ depending on the direction of the applied field and vortex motion (Table 5.1) and ρ is the isotropic resistivity in terms of an activation energy (discussed later). There is a problem, however: what if the vortex moves at some oblique angle and not parallel and perpendicular to the norms in Table 5.1 (i.e., the ac field lies at an oblique angle)? The author's best guess for an approximation to this nightmare, which can easily occur if there is misalignment, is to split B_{ac} into components parallel and perpendicular to the *B-c* plane and use the angle between one of the components and the plane to scale the viscosity in each direction; these can be added to give an effective viscosity (i.e., $\eta_1$sin (angle)+$\eta_3$cos(angle)) which can in turn be divided back into components oriented with the crystal edges. Orientation with the edges allows the use of Brandt's modes.

The in–plane resistivity has been worked out to be [Qiu, 1993]:

$$\rho_{ab}^{c} = \frac{H}{A\exp\left(-\frac{U}{k_B T}\right) + p\frac{H\Phi_0}{c^2\rho_n(T)}}\frac{\Phi_0}{c^2}, \qquad (5.22)$$

where H is the applied field, Φ_0(flux quantum) = 2.07×10^{-7} Gcm^2, c (speed of light) = 3×10^{10} cm/s^2, $A = 0.04\Phi_0/c^2$, U is the activation energy, p is parameter of order unity, and $\rho_n(T)$ is the normal state resistivity = $10^{-2}T$ ($\mu\Omega$cm/K). In the denominator of Eq. 5.22, the first term is for the TAFF region and the second is for the FF region. Most of the dissipation curve falls in the TAFF region, only the very foot of the dissipation curve (before where one might expect a T_{melt} kink) should fall in the FF region; therefore it will be ignored. Equation 5.22 is almost

the same resistivity that was the starting point for Ziese, 1994. The prescaled resistivity from [Ziese, 1994] is

$$\rho_{ab}^{c}(T,H) = \rho_{ab}^{c}(T_m)\exp\left(-\frac{U(T,H)}{kT}\right), \tag{5.23}$$

where T_m is the melting temperature. U is an effective activation barrier given by

$$U(T,H) = U_0\left(1-\frac{T}{T_m}\right)^{p} H^{-q}. \tag{5.24}$$

U_0, p, and q are free parameters, also see [Palstra, 1990]. If the Blatter scaling theory is now applied, Eq. 5.24 becomes

$$U(T,H,\theta,\phi) = \varepsilon_t\varepsilon_p U_0\left(1-\frac{T}{T_m}\right)^{p} H\varepsilon(\theta,\phi)^{-q} \tag{5.25}$$

for $T \le T_m$. For $T \ge T_m$, $U = 0$.

Finally, the diffusivity can be more explicitly written as

$$D_v^{H}(T,H,\theta,\phi) = \frac{\rho_{ab}^{c}(T_m)\exp\left(-\dfrac{U_0\left(1-\dfrac{T}{T_m}\right)^{p}\left(H\varepsilon(\theta,\phi)\right)^{-q}}{k_B T}\right)}{\mu_0 f(\theta,\phi)}, \tag{5.26}$$

where $f(\theta,\phi)$ is determined by the conditions of the mode and can be found in Table 5.1 as previously mentioned. Note the melting temperature from [Beck, 1992] is a function of field and is given by

$$T_m = T_c - AH^{1/2}\varepsilon^{1/4}(\theta,\phi), \tag{5.27}$$

where

$$A = \frac{\pi^2 k_B T_c \lambda_{ab}^2}{\varepsilon_t\varepsilon_p \Phi_0^{1/2} c_L^2}, \tag{5.28}$$

λ_{ab} = 140 nm is the in-plane penetration depth at zero temperature and c_L~0.1 is the Lindemann fraction. Note, T has been assumed to scale like T_m as was

assumed by Zeise, this should be checked as this may not be correct on second thought).

Brandt's Modes

Given that there is some initial flux through the sample, any added magnetic perturbation, an ac field, that is orthogonal to the flux will cause the flux to move. Because the perturbation originates on the outside, it will diffuse in through the slab with some characteristic time, τ, dependent on the geometry and diffusivity of the sample. If a range of diffusivities are swept through during a temperature sweep ($D(T)$), at some point τ will match the ac perturbation. For this value, the flux will be most effectively driven into the sample resulting in maximal dissipation. A heuristic microscopic picture for the dissipation is that energy is dissipated because one is trying to move a vortex, which is locally pinned in a potential well, out of the well. If a vortex is strongly pinned as occurs at low temperatures < ~70 K, the vortex is not easily moved, and vortices which don't move don't dissipate energy. On the other hand, if the pinning is very weak, little energy will have to go into moving them, and there will once again be little dissipation. For intermediate pinning, one gets sufficiently deep wells and a sufficient amount of motion to produce lots of dissipation.

For a rectangular crystal of length (l) > width (w) > thickness (d), the geometry produces three modes for a cantilever shown in Fig. 5.8. For mode 1, B_{ac} is in the ab plane along the length and B_{dc} is parallel to the c axis; $\tau_1 = d^2/\pi^2 D$. For mode 2, B_{ac} is parallel to the c axis and B_{dc} is in the ab plane along the length; $\tau_2 = 4l^2 d/\pi^3 wD$. For mode 3, B_{ac} and B_{dc} are oblique to the c axis, for this case,

mode 3 will only be excited if the $\cos(c\text{-}B_{dc}) < w/l$; however, if $\cos(c\text{-}B_{dc}) > w/l$, then mode 2 will be excited instead; $\tau_3 = wd/\pi^2 D\cos(c\text{-}B_{dc})$. Oblique angles will scale the peaks by the square of the sine and cosine. There might be a fourth mode for torsional oscillators; one in which both the ac and dc fields are perpendicular to c axis where $\tau \sim wl/\pi^2 D$–this is just an educated guess.

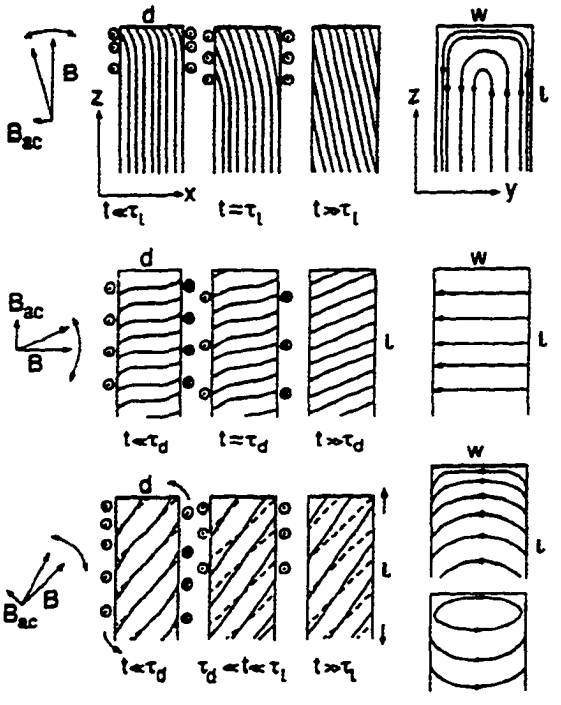

FIG. 5.8. Three possible dissipation modes in an isotropic superconductor. (Top) is mode 2. (Middle) is mode 1 and (bottom) is mode three. The frames show the time evolution relative to the diffusion time for the mode (center). Direction of super currents (right) and ac and dc field (left) [Brandt, 1992].

The dissipation for each mode is given by Eq. 5.2. The imaginary part of the ac susceptibility, χ'', is

$$\chi'' = \frac{\sinh(v) - \sin(v)}{v(\cosh(v) + \cos(v))} \tag{5.29}$$

where

$$v = \left(\omega(l_{mode})^2 \mu_0 / 2D_{ac}^{B}\right)^{1/2}. \tag{5.30}$$

l_{mode} is the diffusion length for a given mode; it is just $\tau \times \pi^2 D$; i.e., d^2, $4l^2d/\pi w$, $wd/cos(c\text{-}B_{dc})$, and wl for modes 1, 2, 3, and the 4 respectively [Gupta, 1993; Ziese, 1994]. ω is the resonant frequency. With Eqs. 5.4, 5.5, 5.20, 5.26, 5.28, and 5.29, fits can be attempted to the experimental dissipation peaks.

H*||*c

The first case involves a crystal 1.4 mm × 0.2 mm rectangular crystal, whose edges are square with the stage. The crystal showed only ~5 twins under a polarized light microscope thus $\varepsilon_t = 1$. For a $\theta = 12.7°$ tilt in the face down orientation with $H \,||\, c$, one might expect two main modes. The primary mode is mode 1, mentioned above, and the other is the hypothetical mode 4. For these modes, B_{ac} is orthogonal to the *B*-*c* plane. This implies that $\eta(modes) = \varepsilon(\theta) \times \eta(inplane)$. Using these conditions gave the fits shown in Fig. 5.9 depicted by dashed lines.

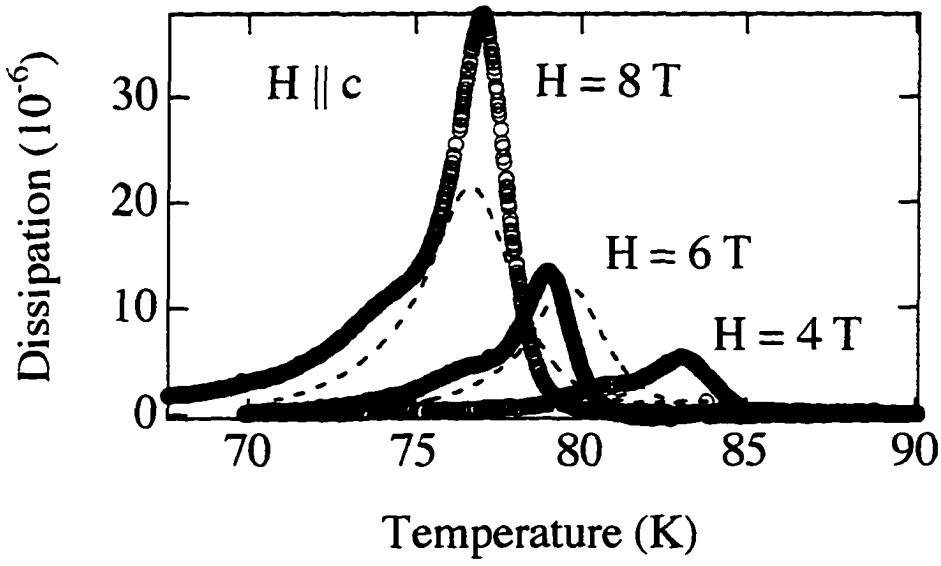

FIG. 5.9. Dissipation vs temperature for increasing field. (Dashed) line fits for data (circles).

The free parameters in Eq. 5.25 are found to be $U_0 = 20350$, $p = 0.9$, $q = 0.7$. These compare with those found by [Ziese, 1994], $U_0 = 18600$, $p = 0.8$, $q = 0.4$. These parameters are not from a computational best fit, but an approximate fit determined by trial and error. Mode 1 accounted for the main peak at both 4 T and 6 T. The 8 T did not match in height although it did match in position; this mismatch most likely stems from the change of the bare oscillator Q which occurred at 8 T when the base fractured.

Unfortunately, the shoulder to the left of the main peak did not correspond to either of the modes used. Even if one was to increase the size of the assumed 1° misalignment, it would not produce a peak in this location.

The peak produced by the theoretical torsional mode 4 is at a higher temperature, and hence is a faster mode corresponding to the very small initial peak seen before the main mode. The mode 4 peak is nicely shown by the 6 T data (Fig. 5.10). The mode 4 peak could also be seen in the 4 T case.

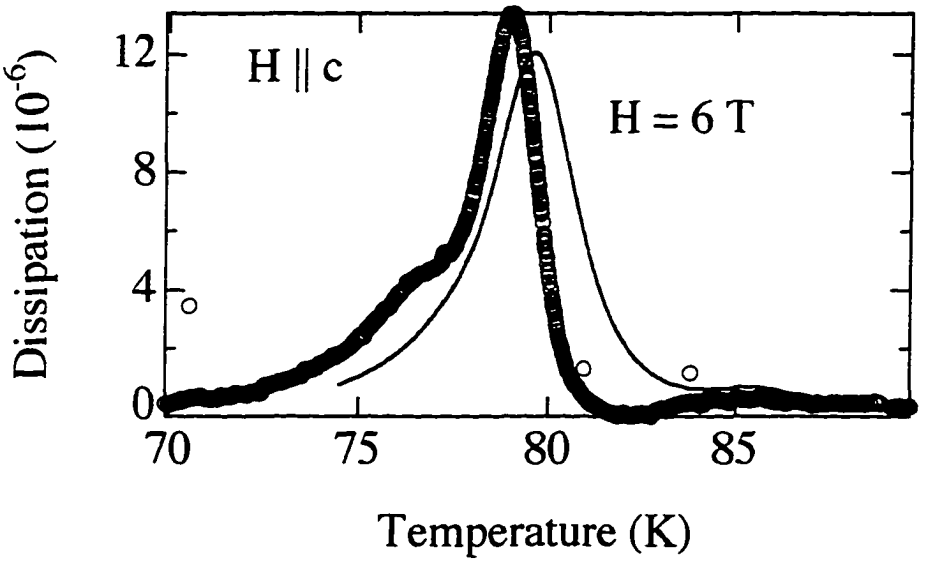

FIG. 5.10. A high temperature small peak corresponds to a theoretic new mode 4 with length scale, wl. The lower temperature peak corresponds to mode 1 with length scale d^2.

H ⊥ c; H || crystal edge; H oblique to twins

This case was performed with the crystal "*osc6 A 2nd crystal*". The crystal was 1.38 mm × 0.82 mm × 28.4 μm. The crystal was glued to the oscillator face such that the crystal edges were parallel to the oscillator edges. The twins were thus at a 42° angle with the x-axis, i.e., $\phi = 42°$. A face down tilt of $\theta = 3°$ was used. Because the crystal was twinned, ε_1 could no longer be set to

one. The resulting dissipation peak for 8 T and 4 T are shown respectively in Fig. 5.11 and Fig. 5.12.

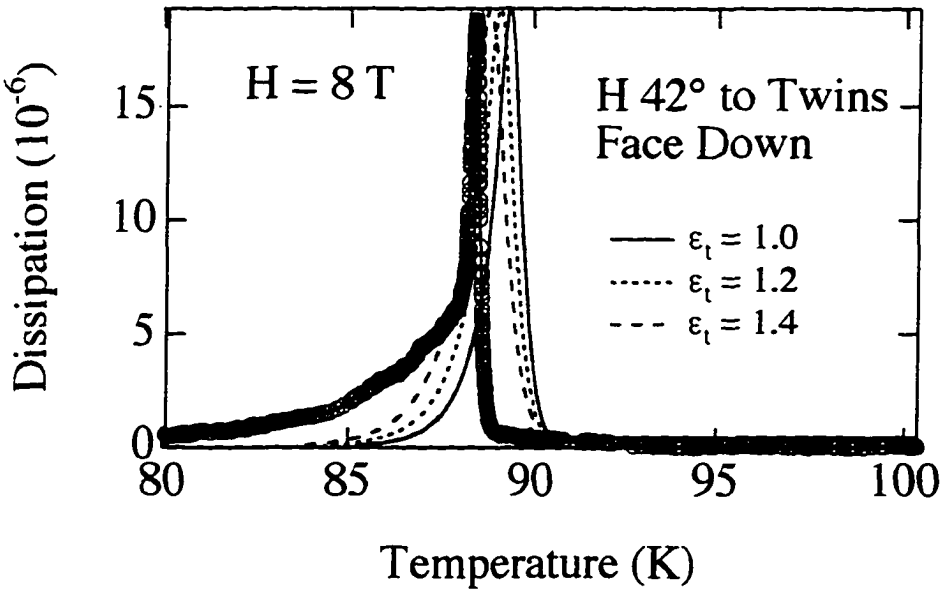

FIG 5.11. 8 T dissipation data, circles, shown against three different fits of the twin anisotropy.

The 8 T data shows a sharp single peak with a long tail. Although the fits do not match the width of the peak, they do mirror the same asymmetry. This data was fit using the torsional mode with length scale *wl*. Increasing the twin anisotropy tended to widen the peak and lower the peak temperature; however, this also tended to make the peak more symmetric—the failure of the fit in this case may be in part due to the neglect of the flux flow diffusivity. Another possibility is that the background, which was determined by an older thicker

oscillator, increases more steeply for the double-side polished wafers. Nevertheless to keep the asymmetry, ε_t is kept between 1.0–2.0.

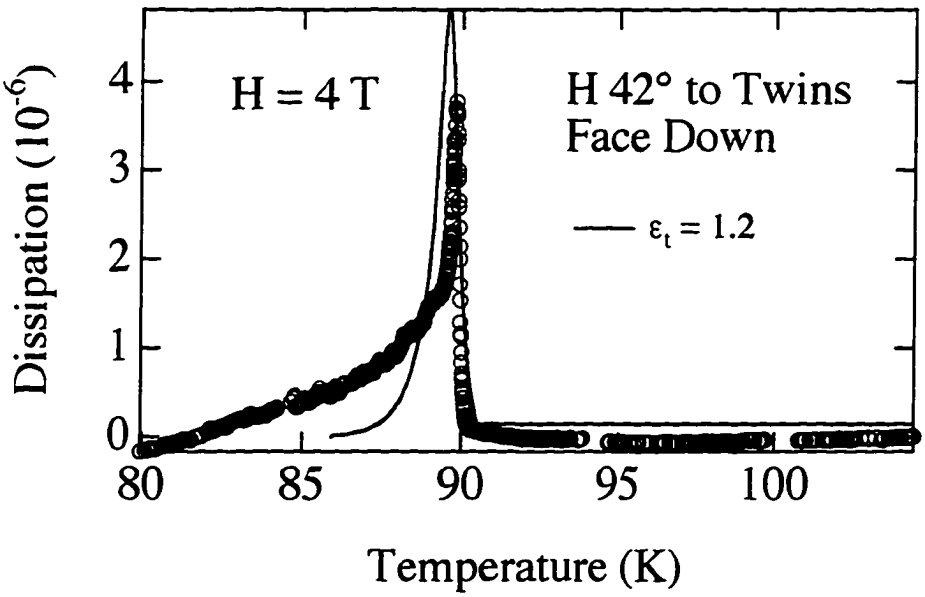

FIG 5.12. 4 T dissipation data, circles, shown against fits for the twin anisotropy.

The fit parameters for the 4 T and 8 T data are $p = 0.8$, $q = 0.3$, $U_0 = 18000$, and $\varepsilon_t = 1.2$. These are close to the values found for the other crystals. Unfortunately, p, q, U_0 can affect the peak in ways similar to ε_t. Extreme care will be needed to more accurately extract the role of the twins in future studies. For example, the twins should be lined up parallel to a side rather than at 42°; this geometry would require cleaving of the crystal! Cleavage should be doable by gluing and filing the crystal between rectangular steel blocks; the glue can be dissolved in acetone—this is similar in part to preparing crystals for the STM.

H ⊥ c; H oblique to crystal edge; H || to twins

For the next two cases, crystal "*osc6 A 2nd crystal*" was used again. For this case θ was taken as 3°; a misorientation of 0.5° was tried, but this produced a peak higher in temperature than the main peak, so this approach was dropped. The crystal was rotated on the head by 42°; this way, the twins were lined up with the field. Needless to say, splitting the dc field and using the diffusivities that corresponded to the length and width ($\tau = wd$ and $4l^2d/(\pi w)$ respectively) did not produce a peak with a secondary shoulder (Fig. 5.13).

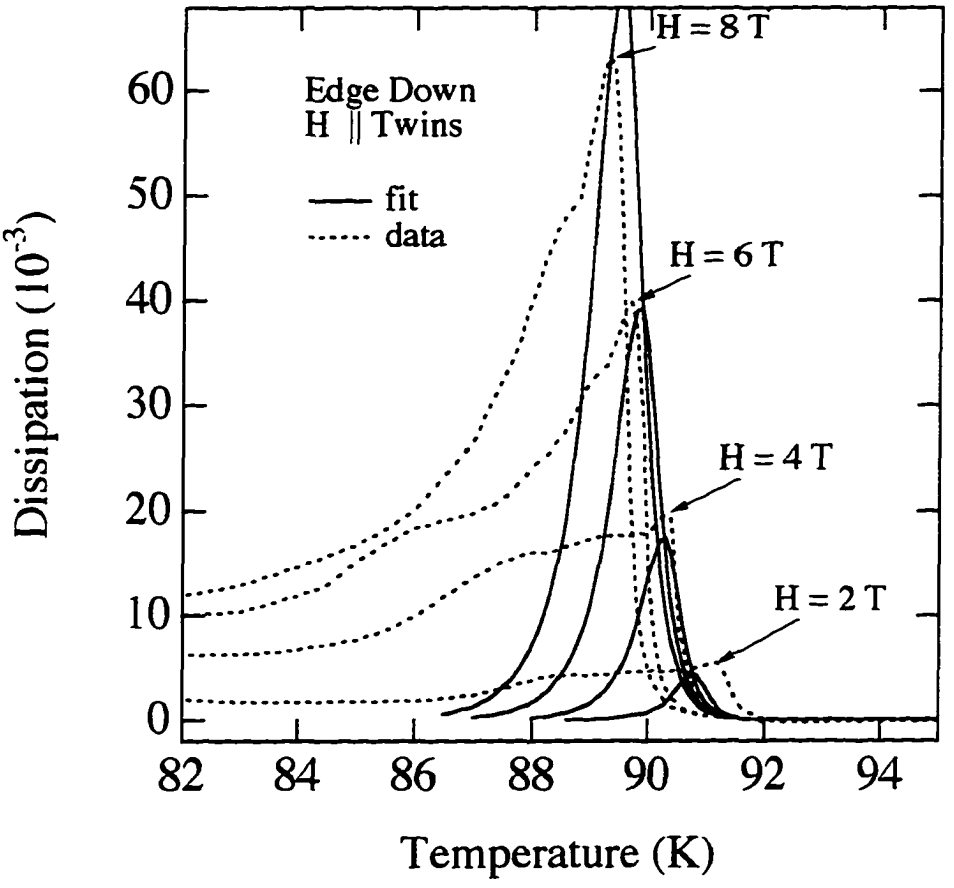

FIG 5.13. Family of dissipation curves for fields between 2 T and 8T (dotted line), shown with respect to fits (solid line). The applied field is parallel to the twins.

Apparently, there are other modes, or Brandt's theory is not being correctly applied to this setup. It may not be correct to simply split the field in the x and y direction. Given a field line parallel to the twin boundary which is driven parallel to the c-axis, there is a continuum of diagonal lengths ranging from zero at the corner to a region of constant length equal to $w/\cos(42°)$ for the crystal. This arrangement would suggest integrating the dissipated power over the different

length scales and then adding a peak for the crystal section where the field lines are of equal length.

For the peak that does fit, the temperature and amplitude scaling with field are in agreement with Brant's theory. The fit parameters also remain close to the other cases: $p = 0.9$, $q = 0.3$, $U_0 = 18000$, and $\varepsilon_t = 1.4$.

H ⊥ c; H oblique to the crystal edge; H ⊥ to the twins

For $H \perp$ twins, $\theta = 2°$. The fit parameters $p = 0.95$, $q = 0.3$, $U_0 = 18000$, and $\varepsilon_t = 1.3$. This case fit even worse than the previous case (Fig. 5.14). The difference in the curve shape implies an effect by the twins. Because the twins are roughly at a 45° angle with respect to the crystal, a 90° rotation of the sample would produce a geometry that is a reflection of the previous case. Thus, any modes resulting from the geometry should be the same as those seen above. The fact that the behavior of this family of curves is so different suggests that some length scale involving the twins might need to be incorporated into a "new mode". A simple twin anisotropy does not seem to be sufficient to describe the roles of the twin boundaries. Of course, not all of these additional features in the dissipation curves need come from geometric modes, as shall be seen in the next chapter.

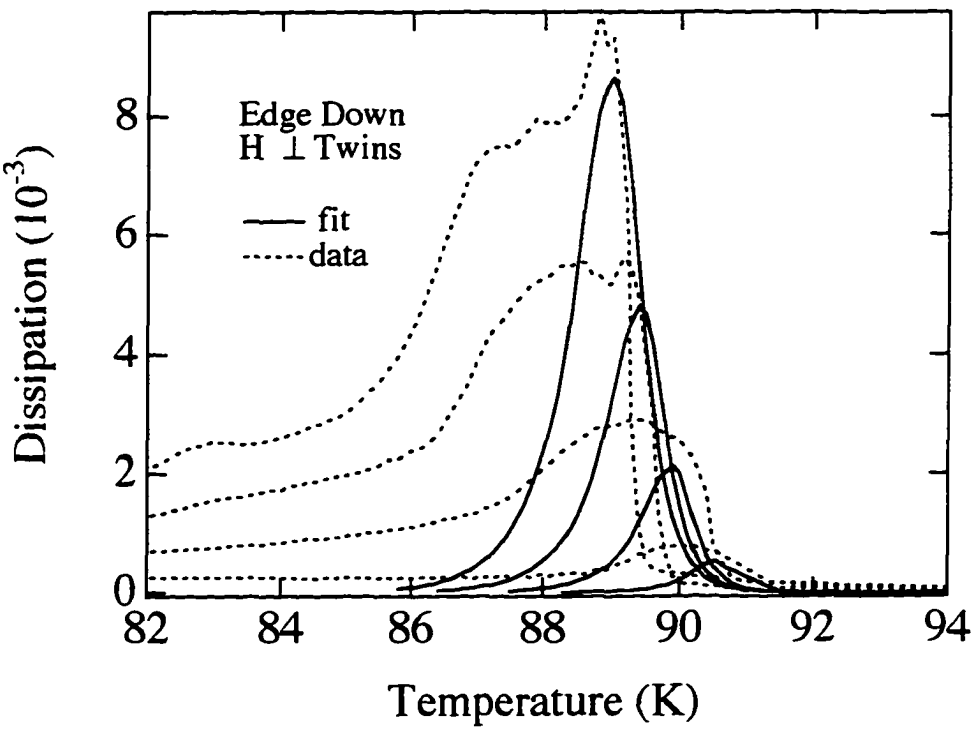

FIG 5.14. Family of dissipation curves for fields between 2 T and 8T (dotted line), shown with respect to fits (solid line). The applied field is perpendicular to the twins.

Chapter 6: Intrinsic Pinning

INTRODUCTION

Using high-Q double-torsional silicon oscillators vibrating at extremely low amplitude, numerous fine minima and maxima were observed in the dissipation vs. temperature data for certain characteristic fields perpendicular to the c axis in single crystal $YBa_2Cu_3O_{7-\delta}$. These additional fine structures, superimposed on the dissipation peaks normally seen, have characteristic properties with regard to field and amplitude. These features were also mirrored in the frequency shift vs. temperature data. An intrinsic pinning model in which the dissipation minima correspond to conditions of commensurability between the interlayer spacing and both the coherence length and Abrikosov lattice spacing was used to explain these features.

PINNING AND LOCKING BY THE SUPERCONDUCTING PLANES

Artificially layered Nb/Cu superconductors have shown interesting field-dependent maxima in their magnetization [Brongersma, 1993]. The layering is used to achieve the condition λ (penetration depth) > d (characteristic dimension) > ξ (coherence length), as is also the case for high-T_c materials, but for the multilayers, the layer spacing merely determines the mass anisotropy, since the coherence length remains relatively long. Shorter coherence length materials like $YBa_2Cu_3O_{7-\delta}$ (YBCO) should show additional effects [Fienberg, 1993; Balents, 1994], since the layer spacing is the characteristic dimension of interest. One such effect is due to the phenomena of "intrinsic pinning": for fields parallel to the layers, the vortices prefer to sit between the superconducting CuO_2 planes, since the suppression of the superconducting order parameter between the planes provides a vortex energy minimum there [Feinberg, 1990].

The potential that a vortex sees has been calculated by Tachiki, 1989. To do this, the order parameter is assumed to vary sinusoidally,

$$\Psi_0(z) = \Psi_1 + \Psi_2 \cos\left(\frac{2\pi z}{a_c}\right). \tag{6.1}$$

Ψ_1 and Ψ_2 are positive parameters and a_c is the plane spacing. The maxima in the order parameter correspond to the two CuO_2 planes. Considering an isolated vortex [Tinkham, 1996], the order parameter can be approximated as

$$\Psi(r) = \Psi_0(z)\tanh\left(\left(\frac{x}{\xi_{ab}}\right)^2 + \left(\frac{z-z_0}{\xi_c}\right)^2\right)^{1/2}, \tag{6.2}$$

where ξ_{ab} and ξ_c are the coherence lengths parallel to the corresponding crystal axes. Given that the condensation energy density of a uniform superconductor is

$-H_c^2/8\pi$, a perturbation in the order parameter will produce a change in the condensation energy density of the form [Saint-James, 1969]

$$f_s - f_n = \frac{H_c^2}{4\pi}\left[1-\left(\frac{\Psi_{perturbation}}{\Psi_1}\right)^2\right]. \tag{6.3}$$

Thus for the modulation caused by the planes and planes plus isolated vortex, one finds respectively,

$$\Delta f_{planes} = \frac{H_c^2}{4\pi}\left[1-\left(\frac{\Psi_0}{\Psi_1}\right)^2\right] \tag{6.4a}$$

$$\Delta f_{planes+vortex} = \frac{H_c^2}{4\pi}\left[1-\left(\frac{\Psi(r)}{\Psi_1}\right)^2\right]. \tag{6.4b}$$

Integrating the difference of Eq. (6.4b) and (6.4a) gives the energy barrier produced by the planes that a vortex sees. Taking the difference and substituting in Eq. (6.1) and Eq. (6.2), one finds this energy,

$$U(\xi_c, z_0) = \frac{H_c^2}{4\pi}\int_0^\infty\left[1+\delta\cos\left(\frac{2\pi z}{a_c}\right)\right]^2 \operatorname{sech}^2\left[\left(\frac{x}{\xi_{ab}}\right)^2+\left(\frac{z-z_0}{\xi_c}\right)^2\right]^{1/2} dxdz \tag{6.5}$$

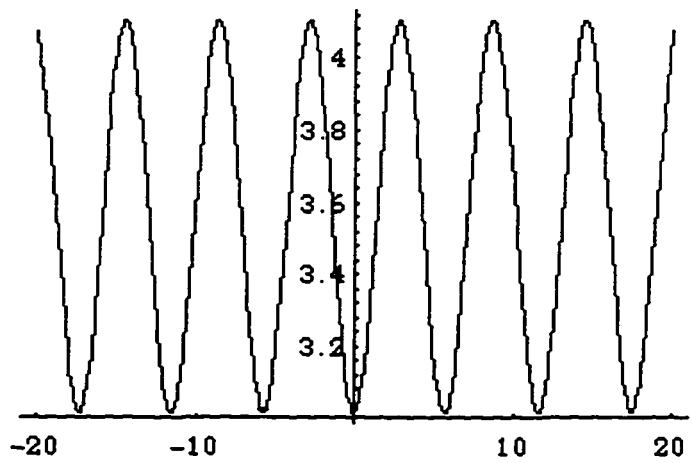

FIG. 6.1. The potential (y-axis) a vortex sees vs position in angstroms (x-axis).

This integral can be solved and is used in a later section of this chapter. It is graphed above in Fig. 6.1.

A consequence of this locational preference results in vortices being locked between the superconducting planes even when the applied field, **H**, is not entirely parallel to the planes; in other words, the induction **B** is not parallel to **H**. This trapping of the vortex cores will occurs as long as the angle between **H** and the normal to the planes is greater than a certain critical angle, θ_c, for the material at that applied field. Outside of this angular range, the cores are drastically affected, forming staircase structures (see Fig. 6.2).

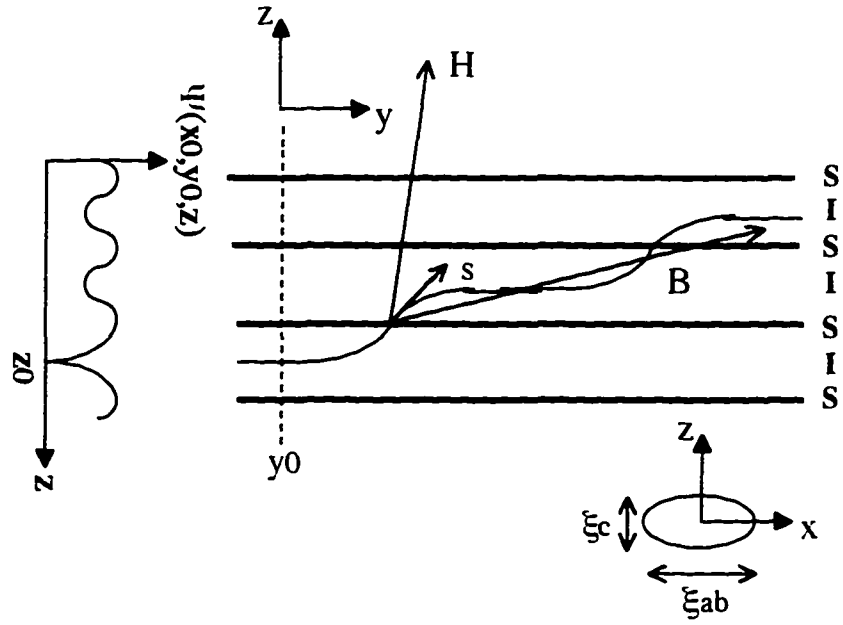

FIG. 6.2. Superconducting/Insulating layered structure and a staircase-like core. The periodically varying order parameter is shown left. The core cross-section is given below. The direction of the applied field (H), the local field (s), and the induction (B) are all different.

Note, the core can be much smaller relative to the superconducting plane spacing; it is strongly affected by the planes while the London penetration depth, which is long relative to the plane spacing, will show smaller effects.

In order to calculate θ_c, which determines the lock-in transition, one starts with the Gibbs free energy. The Gibbs free energy is used because for a fixed applied field, the minimum Gibbs free energy will describe the stable state. For intermediate fields, $H_{c1} << H << H_{c2}$, the Gibbs potential is

$$G = \int d^3 r \left\{ \frac{h^2 + \lambda^2 (curl h)^2}{8\pi} + \sum_{i>j} F_{ij} - \frac{B \cdot H}{4\pi} \right\}, \tag{6.6}$$

where the first term is the line energy, the second term is the vortex interaction energy—the vortices can be assumed to be in a periodic array, and the last term is the magnetic field energy. An explicit solution for Eq. 6.6 and the conditions derived from its minimization are given by Feinberg, 1990. One of the main results,

$$\cos\theta_c = \frac{1}{\pi} \left[2\alpha_1 \frac{H^*}{H} \left(1 + \varepsilon^2 \frac{H^*}{H} \right) \right]^{1/2}, \tag{6.7}$$

determines θ_c, where ε is the mass anisotropy, α_1 gives the barrier height which dissuades vortices from crossing the superconducting planes, and H^* is given by

$$H^* = \frac{\phi_0}{4\pi\lambda^2} \varepsilon^{-1/3} \left\{ \ln \left[\left(\frac{H_{c2}}{B} \right)^{1/2} \right] + \alpha \right\} \tag{6.8}$$

where α is an average difference in the condensation energy for a vortex in the superconducting layer relative to the insulating layer. Using $\alpha_1 = 0.5$, $H = 3$ T, $\varepsilon = 5$, and $H^* \approx 300$ Oe, $YBa_2Cu_3O_{7-\delta}$ would be expected to have a θ_c of 86°. Thus, any $YBa_2Cu_3O_{7-\delta}$ crystal attached to the oscillator must not have an angle

that exceeds this value for observation of intrinsic pinning (for crystals glued flat on the oscillator face, this means the tilt must be less than 4°).

Such additional pinning (intrinsic pinning) can lead to small perturbations in the field and temperature dependencies normally seen in magnetization measurements [Oussena, 1994]. Oscillatory tilting of a superconductor in a dc field is one technique for probing the effects of pinning [de Brion, 1991; Brandt, 1986]. Doing so produces an ac field in the material that drives vortices in the material. As discussed quantitatively for vibrating superconductors by Brandt [Brandt, 1991], an ac field applied to a type-II superconductor will result in dissipation as seen in chapter 5. Because the dissipation is dependent on the flux diffusivity, which is in turn dependent on the activation energy [Brandt, 1992], it will be sensitive to intrinsic pinning effects throughout the crystal. Besides the dissipation, one may also see changes in the resonant frequency depending on the depth of the pinning potential; i.e., a more strongly pinned vortex that cannot move relative to the crystal will cause an increase in the line tension and hence in the restoring force when the crystal is tilted.

For dissipation studies, such as those done with ac susceptibility or vibrating reeds (or other mechanical oscillators), one normally sees one or two peaks in the dissipation vs. temperature data [Ziese, 1994a; Ziese, 1994b]. These peaks were seen in Chapter 5. As a reminder, such peaks arise when flux diffuses through the sample in a characteristic time that matches the inverse of the oscillation frequency. The characteristic time is related to the geometry of the sample and the vortex pinning. For a given field, because the diffusivity changes with the temperature, this condition will be met once during a temperature sweep

for each particular diffusion mode, leading to a peak [Brandt, 1992]. Typically, one mode dominates; thus, only one dissipation peak is generally seen. For this study however, several fine peaks were seen. It is important to keep the oscillation amplitude small in these studies in order to remain in the linear damping region where local thermally activated depinning events dominate; otherwise, hysteretic damping where the diffusion is nonlinear will set in.

SETUP FOR THE INTRINSIC PINNING STUDY

The Q's as a function of temperature were determined from capacitive amplitude measurements. The oscillator was driven sinusoidally across a second capacitive gap, achieving tilt angles between 4×10^{-6} and 5×10^{-8} radians. For this study, a dc field was applied that was nearly perpendicular to the crystallographic c axis; the oscillator stage was oriented at various small angles (typically $0.5^\circ - 3^\circ$) with respect to the field to enable tilt oscillations. Fields between 1 and 8 T, and temperatures between 100 K and 70 K were employed for most of these studies. Typically, sweeps (requiring many hours, due to the high Q's employed) were started from above the transition to reduce hysteretic effects from trapped flux of the previous runs.

AMPLITUDE DEPENDENCE

In Fig. 6.3, dissipation data as a function of temperature for the torsional oscillator and superconducting crystal system is shown. The various curves are sequential in oscillation amplitude, which decreases from top to bottom. This series of runs was taken at the same applied field, 8 T; however, by virtue of the decreasing amplitude, the effective ac field seen by the sample decreases through

the series. Note that for the ~ 1 mm long crystal, the corresponding angular amplitudes are simply related, e.g., 5×10^{-8} radians for the 0.5 Å amplitude. Clearly, the largest amplitude shows the least amount of structure; there is basically a broad peak with a sharper peak near T_c.

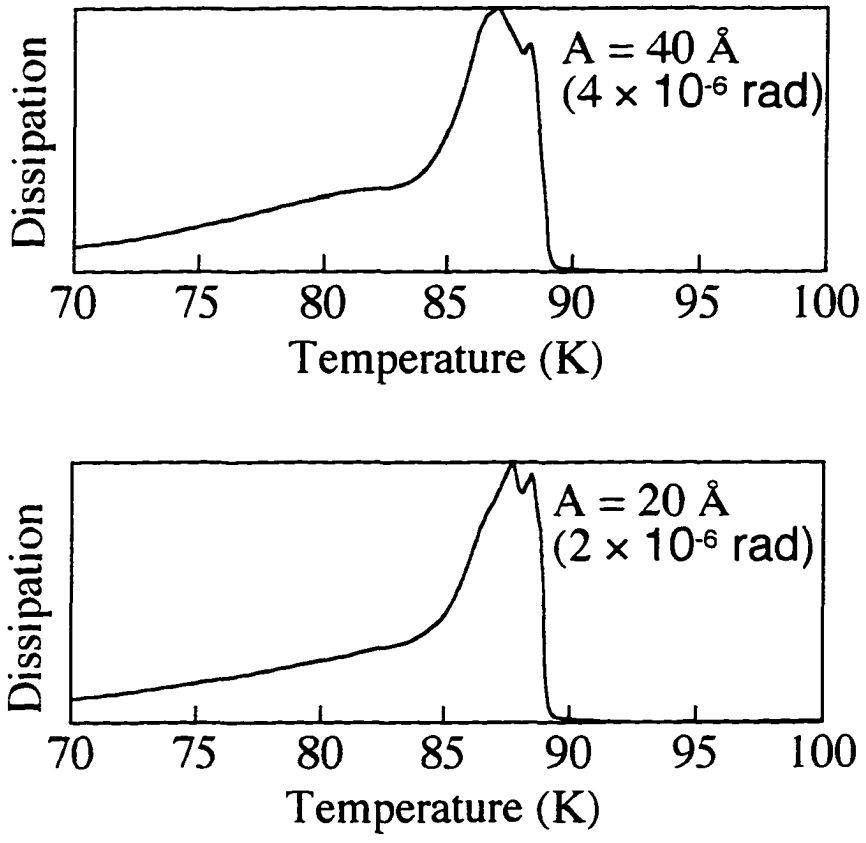

FIG. 6.3. Dissipation data ($1/Q$) as a function of temperature for a $YBa_2Cu_3O_{7-\delta}$ single crystal with the magnetic field H = 8 T applied parallel to the CuO_2 planes. (See next page for continuing frames). Different frames are for different tilt oscillation amplitudes, given in absolute amplitude (angstroms) and in angular amplitude (radians). Note that the fine structure becomes evident for tilt amplitudes comparable to or less than the superconducting layer spacing.

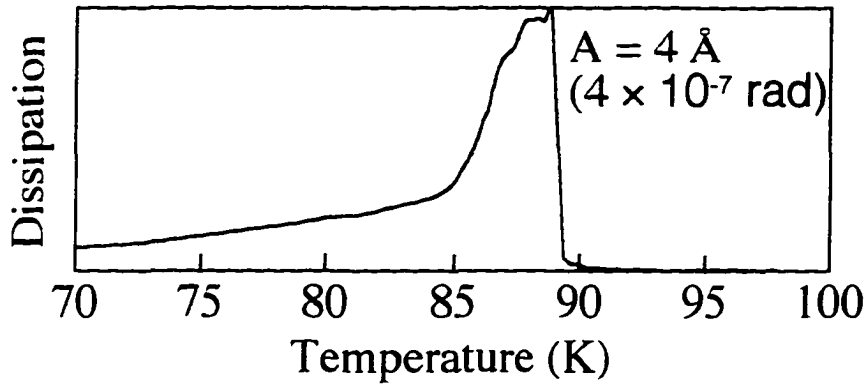

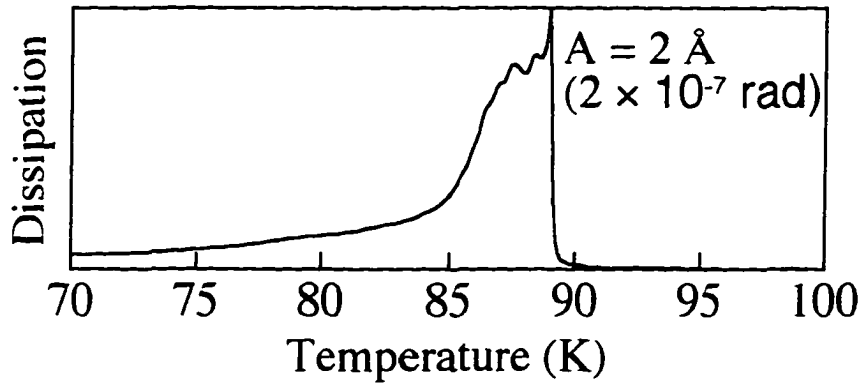

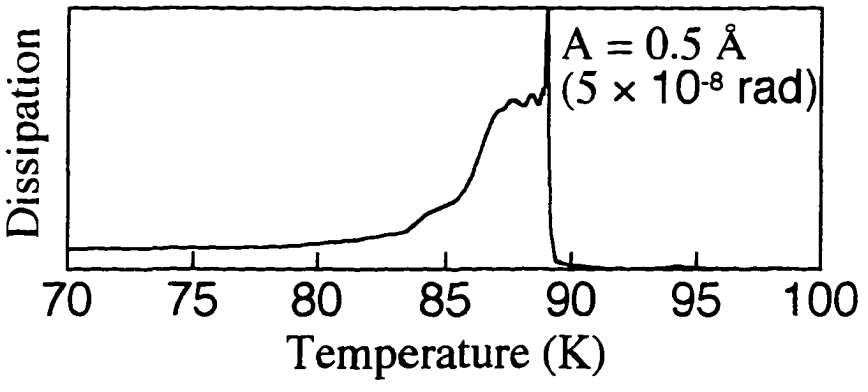

FIG. 6.3. cont.

Mechanical oscillator data taken at much larger amplitudes, ~10^{-3} radians, generally show a single smooth peak [Beck, 1992] shown in Fig. 6.4a.

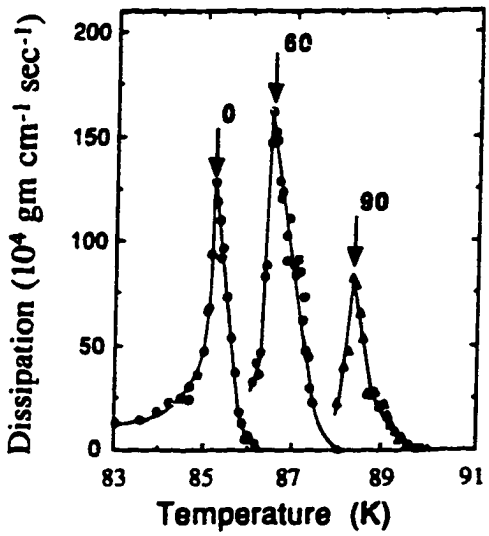

FIG. 6.4a. Large amplitude mechanical oscillator data taken at 2 T for the c axis of the crystal at three different angles relative to the field. Sample rotates through tens of thousands of angstroms [Beck, 1992].

As the amplitude drops, the sharper peak becomes more prominent, and eventually, the broader peak develops structure with several maxima. Other data indicate that these features, and others discussed in this paper, remain in the same relative positions when the temperature is cycled up or down. Apparently, this fine structure in the dissipation is sensitive to being overdriven. This would be reasonable for any very local pinning potential such as intrinsic pinning, where for large amplitudes vortices would be driven across many pinning barriers, washing out any small effects. Note that the majority of the maxima start to become defined between 4 Å and 20 Å amplitude, which is consistent with an

intrinsic pinning picture where the superconducting layers are separated by d = 11.8 Å.

Besides the increased resolution resulting from not over driving the sample, the tilt oscillation amplitude shows a critical value $\theta = 3 \times 10^{-7}$ radians below which the dissipation curves lose their amplitude dependence (Fig. 6.4b).

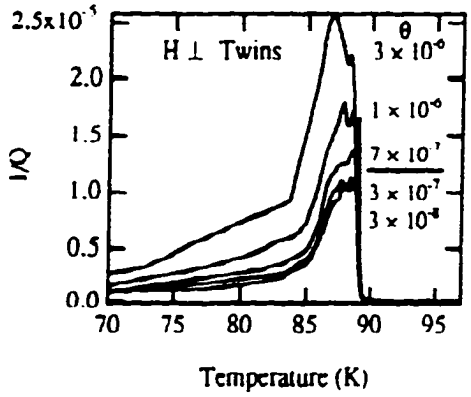

FIG. 6.4b. Amplitude dependence of the dissipation curves. The line denotes a boundary below which the dissipation loses its amplitude dependence.

Shown in Fig. 6.5 are the lowest amplitude data for H = 8 T. Upon examining the structure of this low amplitude data in more detail, one finds a gradual increase in the minima spacing with decreasing temperature. A simple and appealing possible explanation for both the multiple dissipation maxima and for this spacing is as follows: using a first-order approximation of a hard core (with semi-minor elliptical radius $\xi = \xi_c$) in a sinusoidal intrinsic pinning potential, a vortex would be periodically locked between the planes when the coherence length, ξ, is approximately equal to some integer, $n \geq 2$, times the superconducting plane spacing, d:

$$\xi_n \approx nd \tag{6.9}$$

From Ginzburg-Landau theory, the coherence length is a function of temperature [Tinkham, 1996],

$$\xi(T) = \frac{\xi_0}{\left(1 - T/T_c\right)^{1/2}}, \tag{6.10}$$

where ξ_0 is a parameter (for example, in WHHM theory [Maki, 1966, Werthamer, 1966], ξ_0 is related to the zero-temperature coherence length $\xi(0)$ by $\xi_0 = 1.20\ \xi(0)$). Thus the condition for maximum intrinsic pinning, Eq. (6.9), would be satisfied at various characteristic temperatures, T_n, obtained by simply inverting Eq. (6.10):

$$T_n = T_c\left[1 - \left(\frac{\xi_0}{nd}\right)^2\right]. \tag{6.11}$$

Using our value of the fitting parameter $\xi_0 = 5.4$ Å, one finds the characteristic temperatures denoted by the vertical bars in Fig. 6.5, where n runs from 2 to 6. Thus, the minima of the dissipation curve match the intrinsic pinning maxima which correspond to a commensurability of the coherence length and the intrinsic pinning lattice planes.

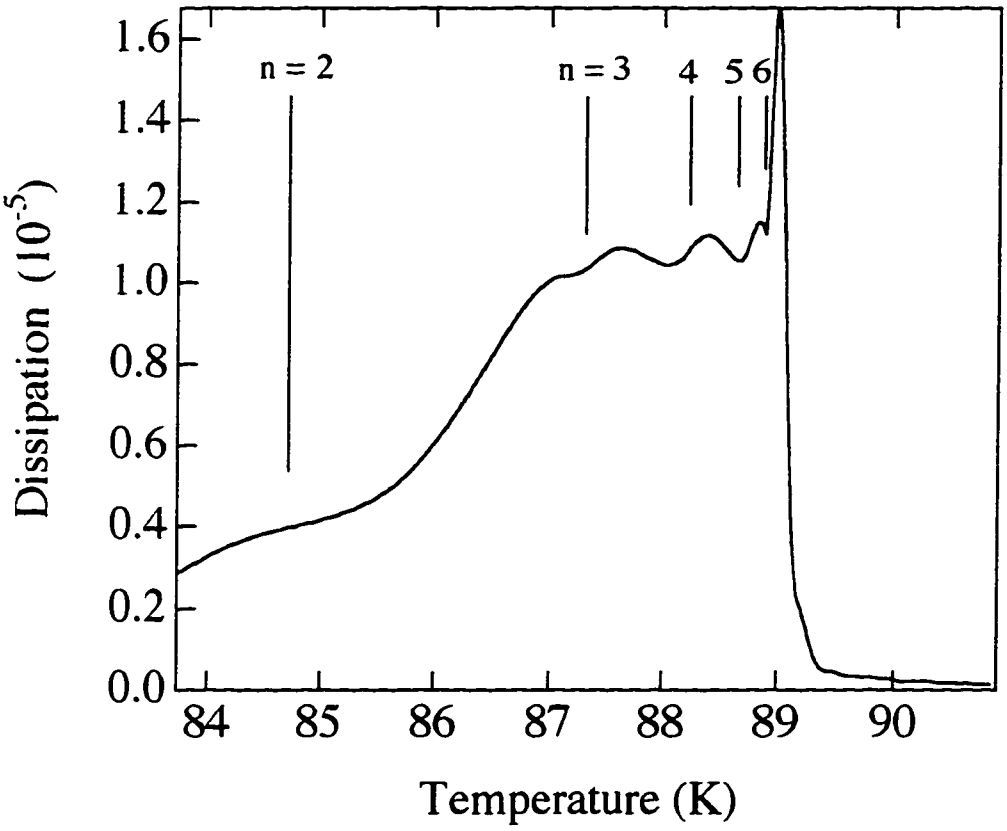

FIG. 6.5. Smoothed dissipation data ($1/Q$) as a function of temperature at H = 8 T for $H \parallel$ planes for the smallest tilt oscillation amplitude studied — approximately 5×10^{-8} radians. Several secondary maxima and minima are resolved. The numbered bars indicate the characteristic temperatures of commensurability between the coherence length and the superconducting layer spacing, reflecting the locations of dissipation minima in an intrinsic pinning model.

One problem remains with this theory. If one considers the potential in Eq. 6.5 as a function of the coherence length, one may graph the energy barrier for a vortex of increasing core size as if the temperature were increasing. Solely considering the core as above, the potential will contain oscillations that have the periodicity of the planes as shown in Fig. 6.6. Although this would tend to support the

coherence length / plane commensurability theory, the oscillations actually occur because of the discontinuity of the hard core approximation, i.e., a double-sided step function of width ξ:

$$U(\xi_c, z_0) = \frac{H_c^2}{4\pi}\int_0^{\xi}\left[1+\delta\cos\left(\frac{2\pi z}{a_c}\right)\right]^2 dxdz. \qquad (6.12)$$

(This can be more easily seen if one integrates Eq. 6.12 with a step function.)

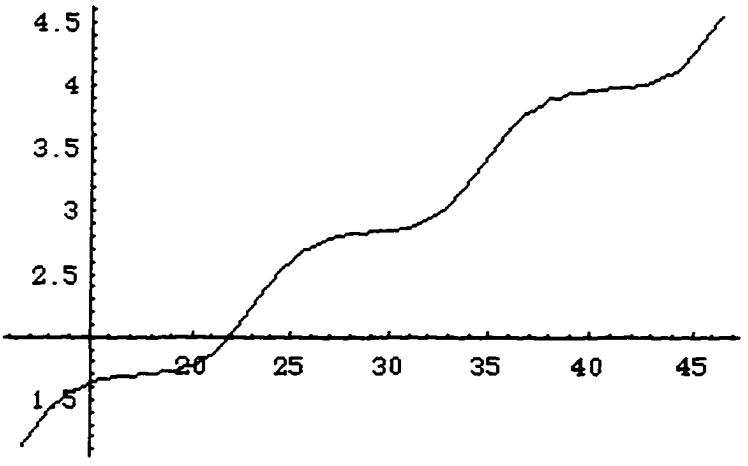

FIG. 6.6. Energy needed to expand a core (y-axis) across the planes vs increasing coherence length (x-axis).

If looks at the energy needed for expanding the standard solution a smooth vortex like that described by Eq. 6.2, (not just a hard core) across the planes, then one can graph Eq. 6.5 as a function of the coherence length. This results in Fig. 6.7.

FIG. 6.7. Energy needed to expand a vortex across the planes for increasing coherence length (x-axis).

The straight line implies that a vortex would not see any rate of change in the energy needed to expand across the planes, i.e., no oscillations in the dissipation should be observed. This is counter intuitive. Part of the problem might arise from the fact that the temperature dependence of the order parameter is never taken into account, or from the fact that the theory does not consider the discrete nature of electronic states in the core. Also, the cosine approximation for the periodic planes may not be correct. It might be interesting to see if these considerations will correct the computational conflict in some future study. Nevertheless, further evidence still keeps the intrinsic pinning model a possibility.

There is another condition that one might expect if these minima indeed arise from intrinsic pinning. Because the dissipation is a measurement that averages over the whole crystal, having only a few of the vortices located at intrinsic pinning sites is not enough for appreciable effects on dissipation. However, there should exist special fields for which the anisotropic Abrikosov

lattice is commensurate with the interlayer spacing that allow for coherent vortex trapping across the whole crystal, resulting in the dissipation maxima and minima described above. Commensurate field effects have been seen at much lower temperatures in the cuprates, as well as in multilayer systems [Brongersma, 1993; Oussena, 1994; Hunnekes, 1994]. The special fields for such commensurate behavior are given by [Oussena, 1994]:

$$H_k = \frac{\sqrt{3}\Phi_0}{2\Gamma d^2 k^2}, \tag{6.13}$$

where Φ_0 is the flux quantum, Γ is the mass anisotropy parameter [$\Gamma \equiv (m_\perp/m_\parallel)^{1/2}$], and k is an integer starting at one. The lower inset in Fig. 6.8 shows the fields for which the vortex lattice is commensurate with the crystallographic lattice spacing (calculated using our magnetically measured value of $\Gamma = 5.8$, which is typical of values obtained by other groups [Welp, 1989; Cobb, 1994]). One should see fine structure only near these field values, e.g., 2.1 T (for $k = 10$), 2.6 T, 3.2 T, 4.2 T, 5.8 T, 8.3 T (to $k = 5$ respectively), etc., up to 210 T ($k = 1$). From Figs. 6.3 and 6.5, appreciable fine structure was evident near 8 T. From Fig. 6.8, one also sees fine structure near 6 T, yet the 5 T data does not show fine structure; it is comparatively smooth, as it should be because it is not near a commensurate field. The upper inset of Fig. 6.8 shows the dissipation as a function of field at the temperature indicated by the arrow in Fig. 6.8 (a secondary maximum). Although oscillations do appear when using this method, they cannot all be directly attributed to commensurability alone. As the field is changed, the dissipation curves also shift down in position relative to the transition temperature in zero field.

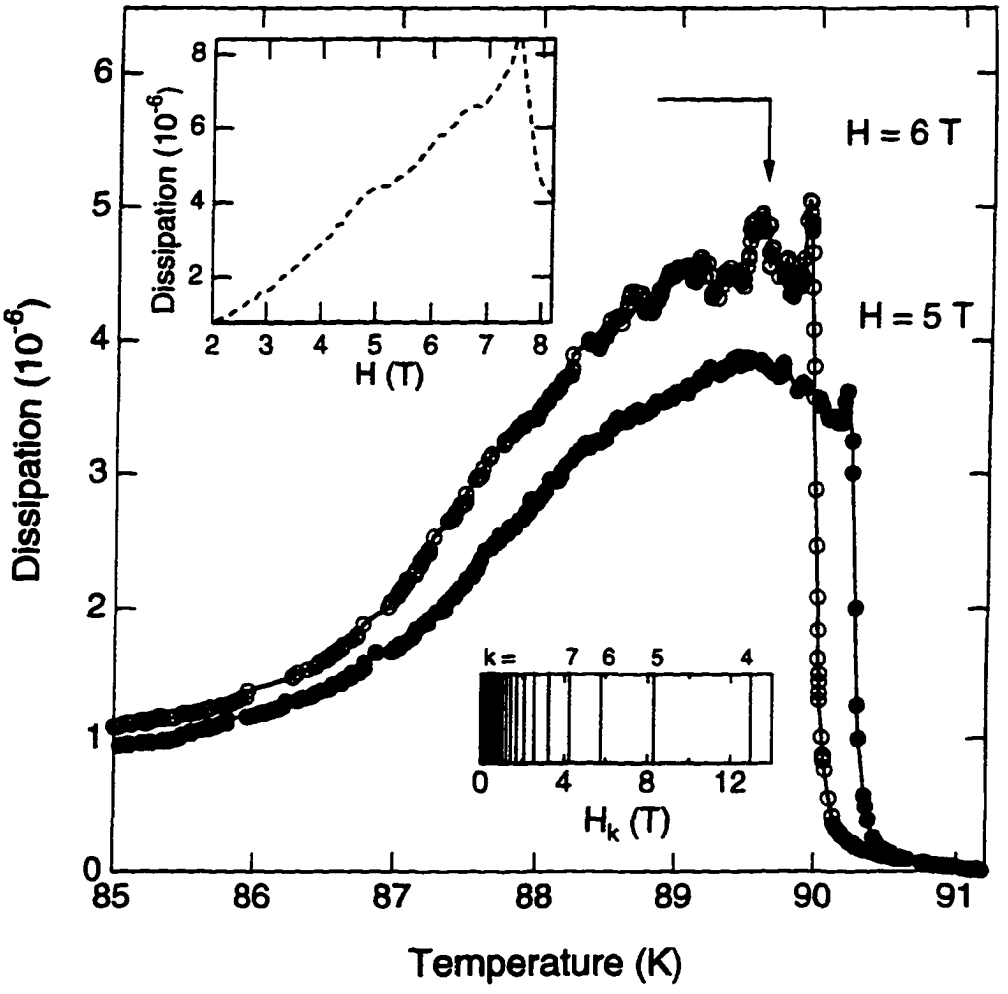

FIG. 6.8. Dissipation data as a function of temperature for H = 5 T and 6 T for H || planes. Like the 8 T data, minima are evident at 6 T; however, they are absent at 5 T. Lower inset: vertical lines indicate the positions of characteristic magnetic fields for which the crystal lattice and vortex lattice are commensurate. Note that magnetic field values of 6 T and 8 T are quite close to commensurate fields, while H = 5 T falls well between characteristic commensurability fields. Upper inset: dissipation as a function of field at the temperature shown by the arrow.

Any changes in the peak due to commensurability are somewhat obscured by the shifting pattern, especially as the large irreversibility peak moves through this

point. For this reason, it is actually more instructive to perform temperature sweeps at different fields so that the field evolution can be decoupled from the pattern shift. Data take at 4 T also showed some structure; however because the features decrease in size with field. they become hard to discern in the noise by this point.

To give a better mental picture and to summarize the two possible contributions to the observed pinning, see Fig. 6.9 below. The left figure depicts the increase in the core size that accompanies an increase in temperature. On the right, two different densities are shown, one which is commensurate with the lattice and one which is not.

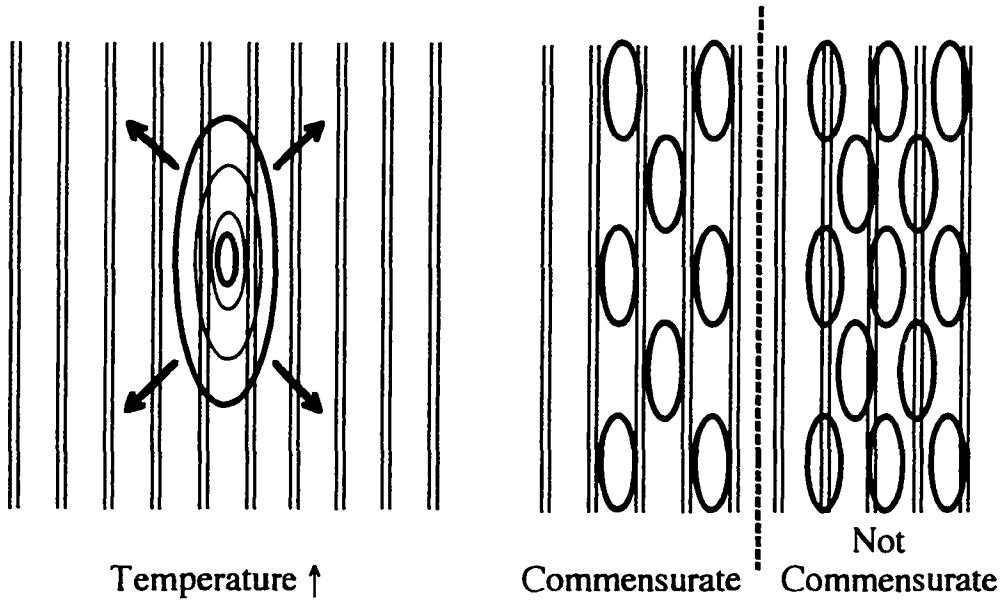

FIG. 6.9. Contributions to pinning. (Left) As the coherence length increases with temperature, the length periodically leads to increased pinning (bold). (Right) Position of vortex cores relative to CuO_2 planes for commensurability.

One quick comment should be made about the features that accompany the frequency shift which is measured in addition to the dissipation peak. Because the frequency changes rapidly in a small temperature range below T_c (due to the varying penetration depth), any small additional changes in the line tension of a vortex will only appear as very subtle perturbations in the slope of the frequency versus temperature data as seen in Fig. 6.10(a). The actual changes become more visible by taking the second derivative with respect to temperature. This second derivative data is compared to the corresponding dissipation peak in Fig. 6.10(b). It is apparent that the oscillations in the curvature of the frequency, i.e., of the vortex stiffness, match the dissipation oscillations discussed above.

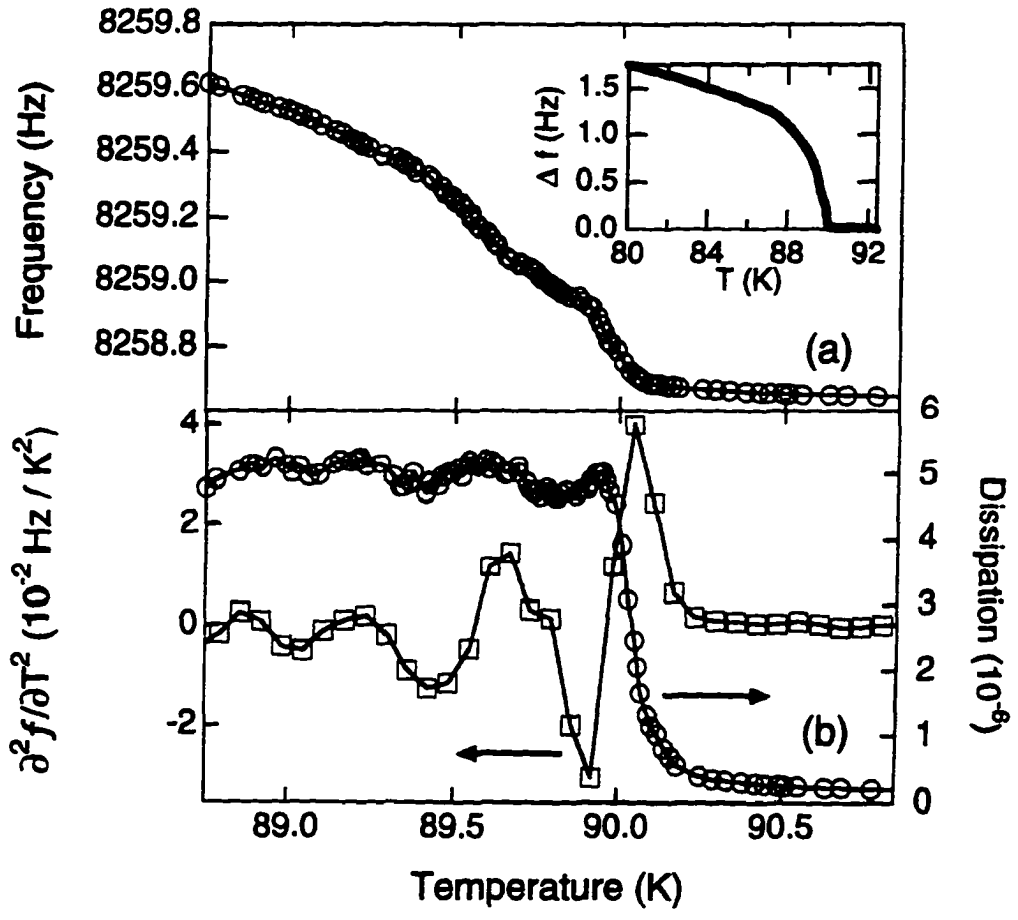

FIG. 6.10. (a) Mechanical oscillator resonant frequency as a function of temperature for $H = 6$ T, $H \parallel$ planes, for temperatures near T_c, with a tilt oscillation amplitude of several angstroms. On this expanded scale subtle variations in the frequency shift are barely evident. Inset: Frequency shift over a broader temperature range. (b) The second derivative of the frequency shift of (a) with respect to temperature and the dissipation data, both as a function of temperature. Note that the frequency shift (vortex stiffness) curvature and the dissipation peaks are correlated.

Finally, one should note that intrinsic pinning should be a higher temperature effect. As one cools the crystal, the flux lines become more rigidly frozen in place. Thus at low temperatures, the steps seen in the field sweep inset

of Fig. 6.8 should disappear. A field sweep done at 40 K is in fact relatively smooth (Fig. 6.11). Note, this sweep was performed on a different $YBa_2Cu_3O_{7-\delta}$ sample.

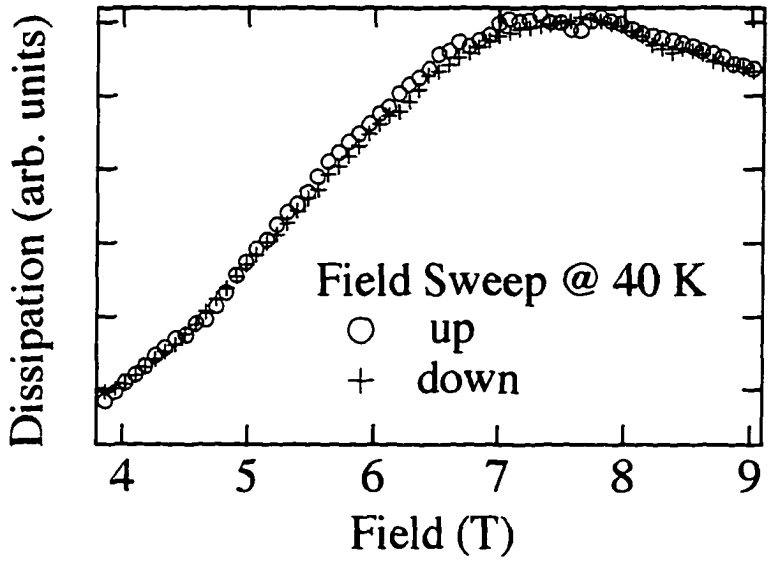

FIG. 6.11. Field sweep taken at 40 K showing relatively smooth curves.

In summary, a number of dissipation minima and maxima have been observed for $YBa_2Cu_3O_{7-\delta}$ using high-Q mechanical oscillators; corresponding features are observed in the oscillator frequency shift. This fine structure can be explained within the framework of an intrinsic pinning mechanism. A simple model, in which a hard-core vortex is strongly pinned when the coherence length is an integer multiple of the superconducting plane spacing and also when the Abrikosov lattice is commensurate with the plane spacing, has been suggested to explain the temperature and field behavior, respectively.

Chapter 7: Oscillators for Other Studies

INTRODUCTION

As alluded to in Chapter 2, the oscillator technique can be used for any experiment in which the forces under study can be coupled to the oscillator to produce changes in dissipation and resonant frequency. Two other applications of the oscillator technique were a viability study looking at aluminum fatigue and the current project to produce an NMR mechanical force detection microscope.

ALUMINUM FATIGUE

One of the workable technologies for flat panel displays uses micro mirrors. These aluminum mirrors can be tilted by applying a voltage and can thus be used to selectively project light to a screen. A problem that arose during the development of this technology was that, after repeated flexing, the mirrors would occasionally stick. The sticking was believed to be part of some fatiguing mechanism in the aluminum, and Texas Instruments started to look into what was

going on in the material. The physics involved was not to the best of the authors knowledge ever worked out, but rather, the problem was empirically solved. Nevertheless before an empirical solution was found, a trial experiment was done to see whether oscillators could be used to study the aluminum fatiguing.

A 10 μm thick aluminum film was evaporated on the oscillator neck. Because mechanical flexing of the aluminum film would be necessary, the film was evaporated onto this part as this is the only part of the oscillator that would allow for substantial bending. The dissipation as a function of temperature was then measured for a 1 V drive and a 10 V drive. The data did not yield any simple and obvious results in this study; they were quite chaotic. To give an idea of how jumpy the aluminum made the amplitude, the oscillator's amplitude and frequency are shown below before aluminum has been evaporated (Fig. 7.1). There are three humps of unknown origin; possibly coming from the epoxy freezing, but the important thing to observe here is that the curves are smooth. These data were taken with a 5 V drive, and the features are the same for a 0.25 V drive. Below 100 K the curves are monatonic and smooth; whatever the cause, the humps above 100 K disappear below.

The Q and frequency can be seen to change quite dramatically for the 1 μm aluminum film (Fig. 7.2). After freezing the film to 100 K, the Q and frequency changed again. From this result, it was apparent that the film was going to be unstable.

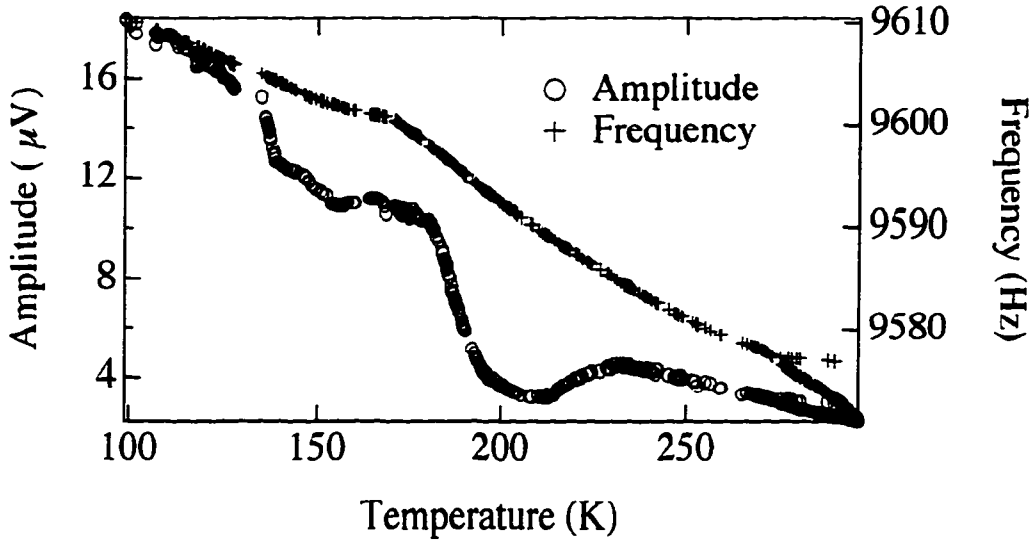

FIG 7.1. Amplitude and frequency of a bare oscillator vs. temperature before aluminum evaporation.

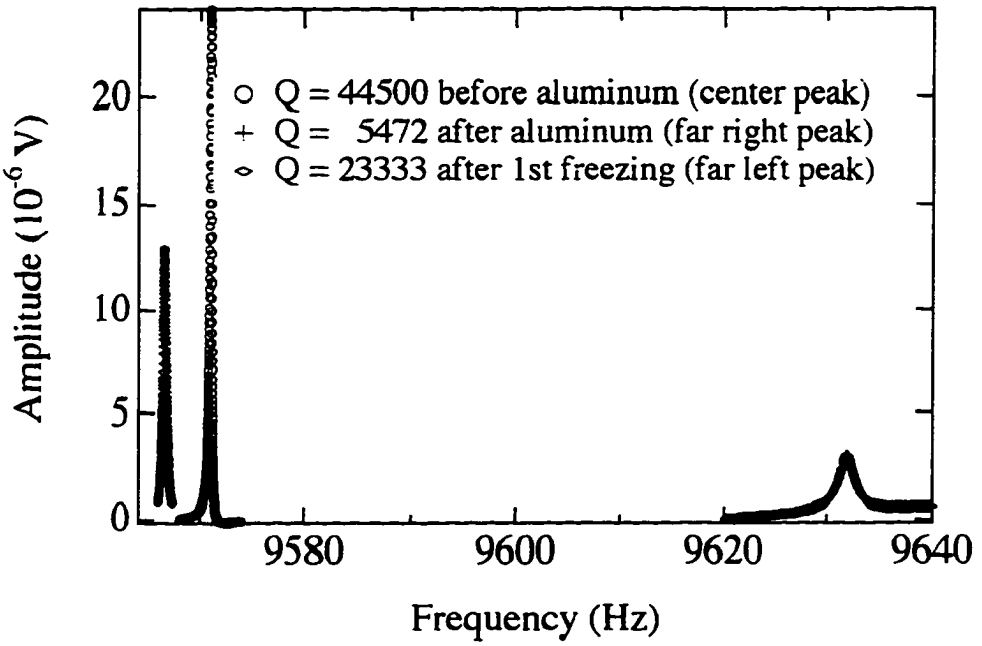

FIG 7.2. Amplitude vs. frequency at three points before the run. The aluminum can be seen to decrease the Q dramatically. After temperature cycling, the Q has partially recovered. The cycling probably relieved stresses in the film.

The runs were carried out for two different drives, one at 10 V and the other with $1/10^{th}$ the amplitude at 1 V. Usual operating procedures for each run were used except that cooling was achieved by slowly lowering the stick into a bath of liquid nitrogen. One prominent feature that stands out from the data shown in Fig. 7.3 and 7.4 is that the film's behavior goes through three distinct phases with respect to temperature. A speculative, but not unreasonable guess, as to what is going on in these regions follows as described for the 1 V case: Initially the dissipation of the oscillator is flat; in this region, roughly above 260 K, the film acts like a single spring in the Hooke's law region. Beyond this

point, the elastic limit for the film is exceeded, thus entering the second region. Here the film is becoming more brittle as it cools and it starts to fracture into multiple regions that dissipate energy as they rub against each other. The Q drops of course and is not smooth as the pieces stick and slip against each other. Finally, at a sufficiently low temperature the domains stop interacting; whether this would result from a sufficient amount of shrinking at this temperatures so that the regions do not rub or from the material cold welding is not obvious. It might seem, that with a larger drive, the third region should occur at a lower temperature than for the smaller drive, which the dissipation data clearly does not show. However, it may be that the film is fractured into much smaller regions by the large drive, and the small domains can contract easier so interactions between the smaller regions stop at a higher temperature. As a reminder, this is all just FUN guess work. For the 10 V drive, the drop in the amplitude occurred sooner and more dramatically than for the 1 V signal. This would tend to support the idea that cracks develop in the film where the larger driving amplitude pushes the film into a non-Hooke's law like behavior at a temperature at which it should not be as brittle. So one might be able to simulate stressing of the micro mirrors by running at a lower temperature.

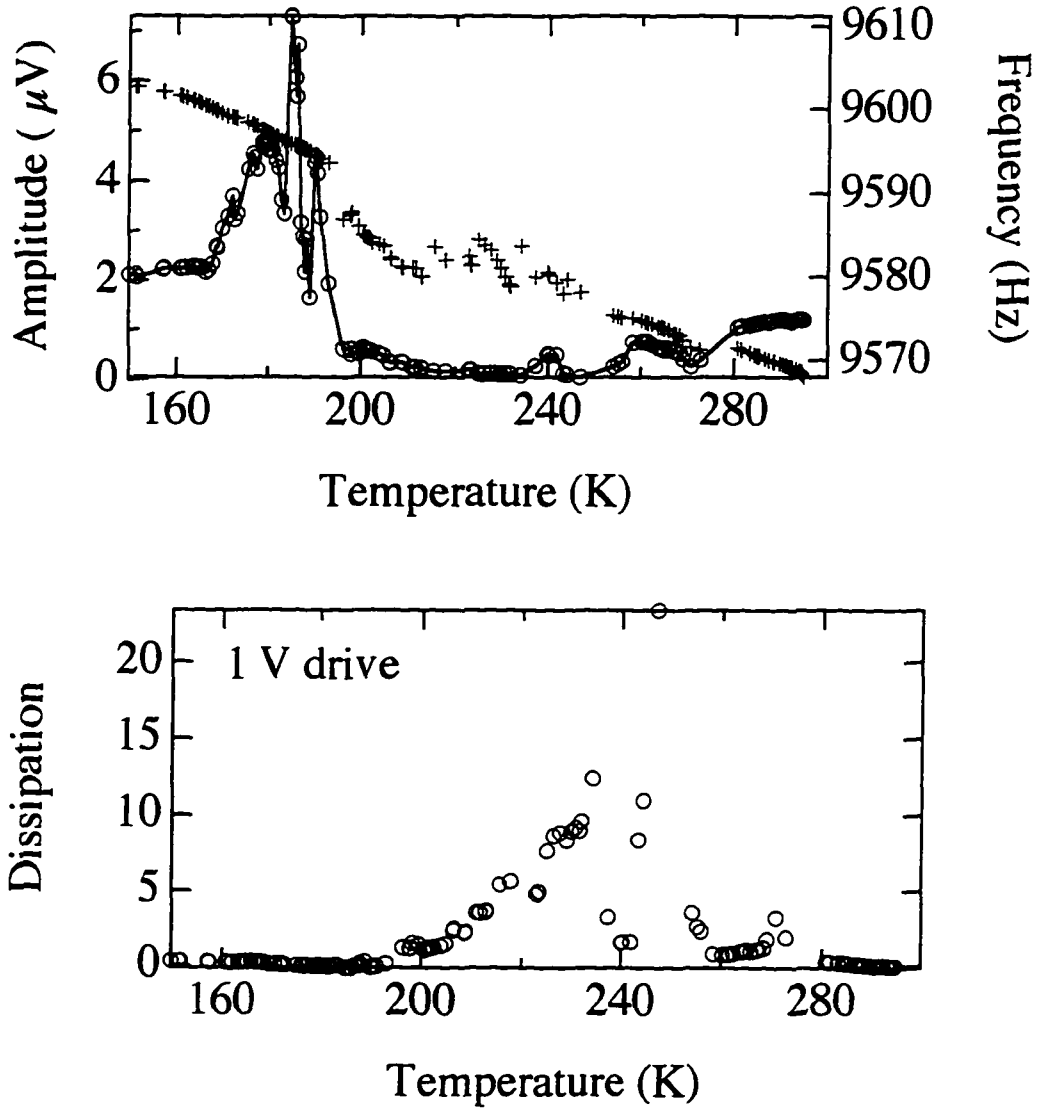

FIG 7.3. Upper shows dissipation in arb. units vs. temperature for a 1 V drive. Lower shows amplitude and frequency vs. temperature with the background subtracted off.

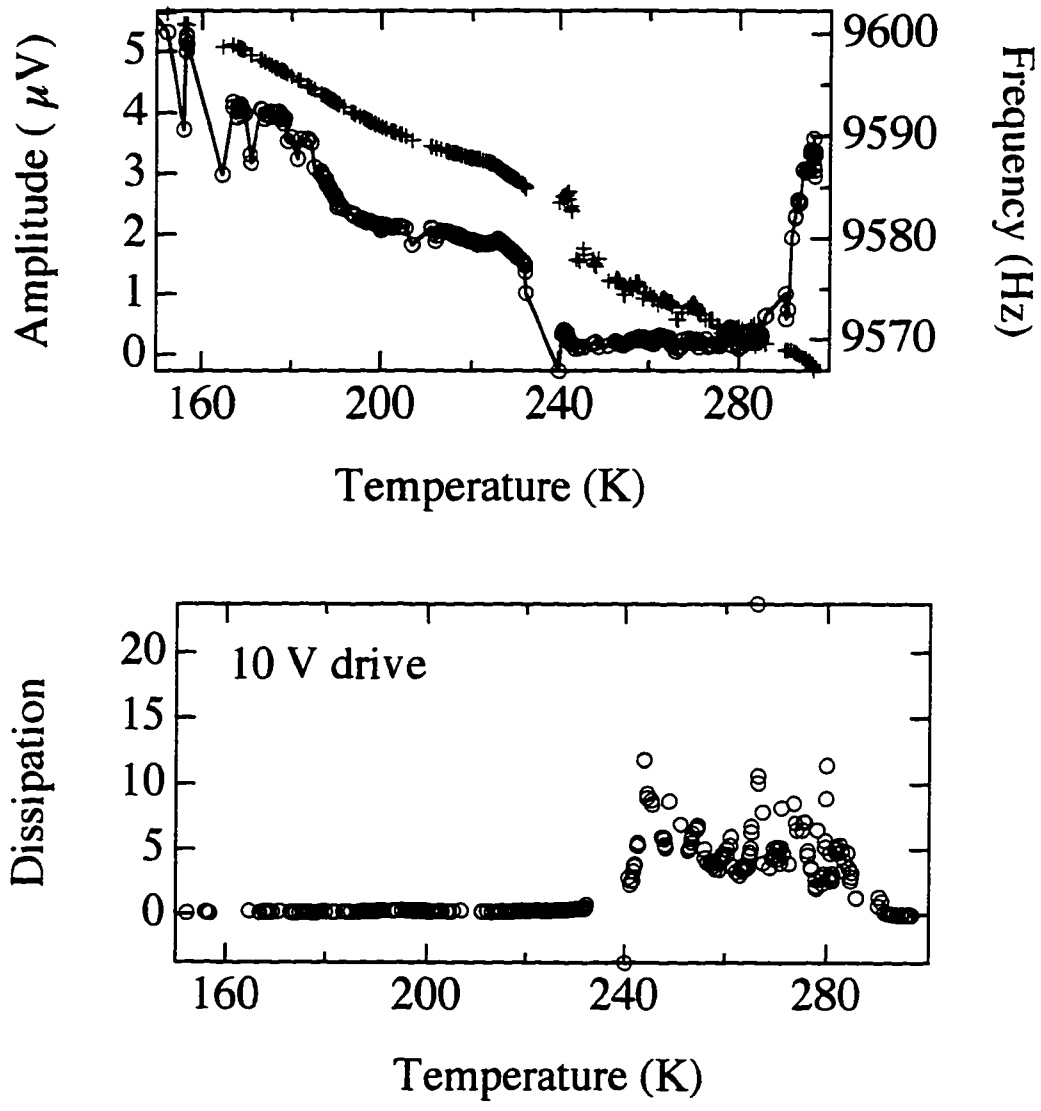

FIG 7.4. Upper shows dissipation in arb. units vs. temperature for a 10 V drive. Lower shows amplitude and frequency vs. temperature with the background subtracted off.

Because the data were taken manually, there is additional information in taking the data that may not be obvious from the computer recorded points. After

days of tracking resonances, one develops a feel for how hard it is to get on resonance and the changes in it once there. Figure 7.5 is a temperature line giving the observed behavior during the resonance tracking with the data never having been seen.

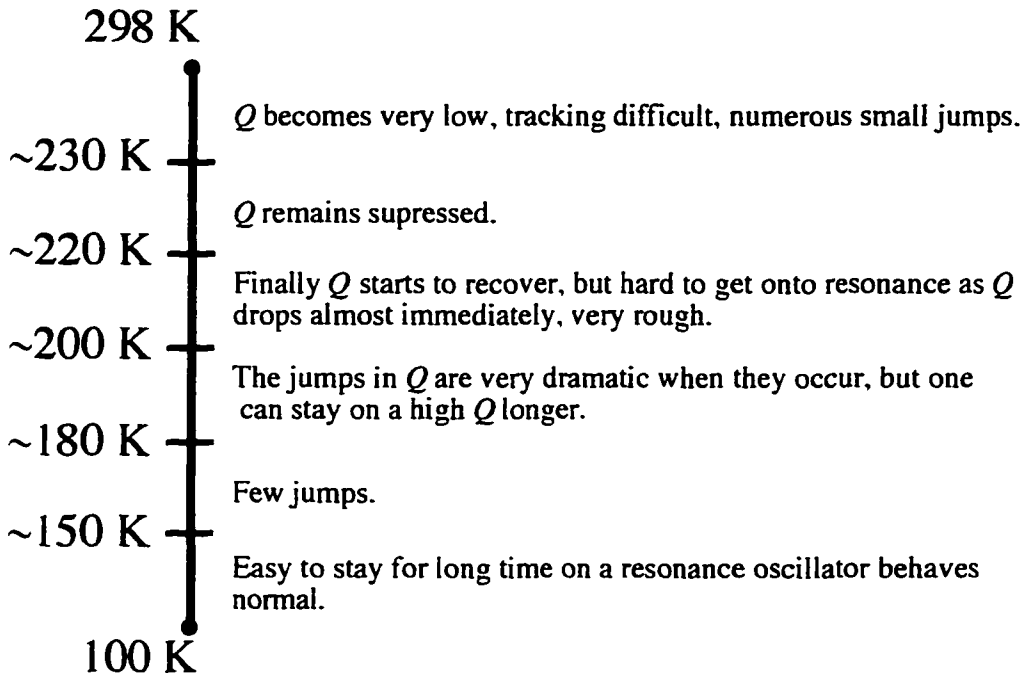

FIG 7.5. Film behavior with temperature noted during run.

After these runs, the Q of the oscillator was not as smooth (Fig. 7.6). Either the film or oscillator was damaged, if the damage is to the film, then this would also support the possibility of some sort of film cracking.

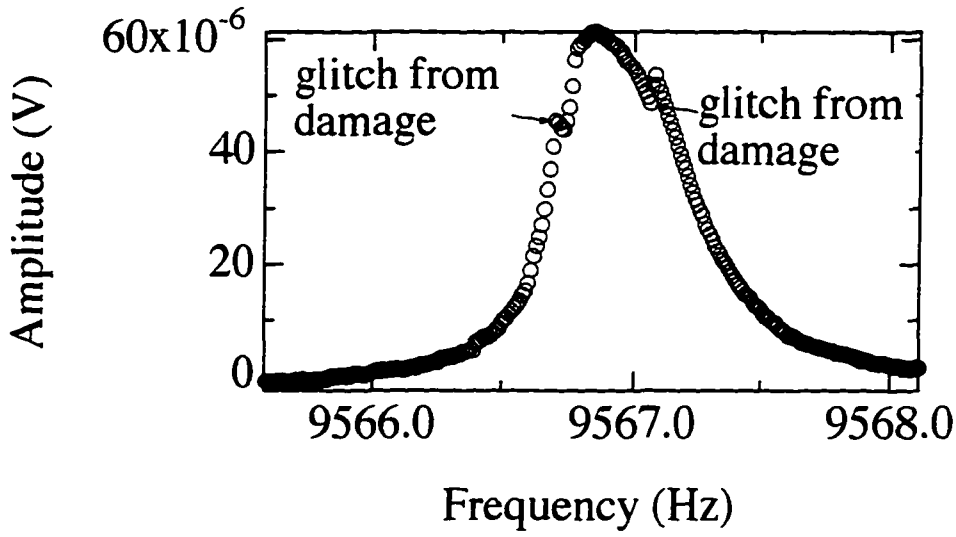

FIG 7.6. Amplitude vs. frequency at room temperature. The glitches do not occur for a healthy oscillator.

Ultimately, the aluminum survey did show complex and unusual behavior; unfortunately, it did not show anything of obvious interest or application for Texas Instruments.

MECHANICAL DETECTION OF MAGNETIC RESONANCE

Probably the most interesting and most revolutionary application of torsional oscillators in the lab, should it work, is in the NMR microscope [Rugar, 1994]. This is the dissertation topic of Tina Barrett and will be extensively discussed in her dissertation, but because it is a use for the oscillators, a few sentences should written if nothing more than for an advertising blurb.

In conventional NMR, some number of nuclear moments in the sample are aligned with a static magnetic field. The resulting magnetization of the sample is

proportional to the susceptibility and the field strength. The magnetization is then tipped perpendicular to the static magnetic field around which it precesses. If the tipping field is removed, the nuclear spins will relax back to their original state with time. This time can be used to extract properties of the sample. Because the moments precesses, it can induce a voltage in a coil allowing for the detection of the magnetization and changes in it.

Mechanical detection uses an oscillator rather than a coil for detecting the magnetization. By applying a field gradient, the precessing spins will feel a force, $\boldsymbol{F} = \boldsymbol{M} \bullet \nabla \boldsymbol{B}$. If the force is coupled to an oscillator by putting the sample on the oscillator and the source of the field gradient near by, then the force can be detected (Fig. 7.7). Because of the small size of the oscillators employed here, optical detection is used rather than capacitive.

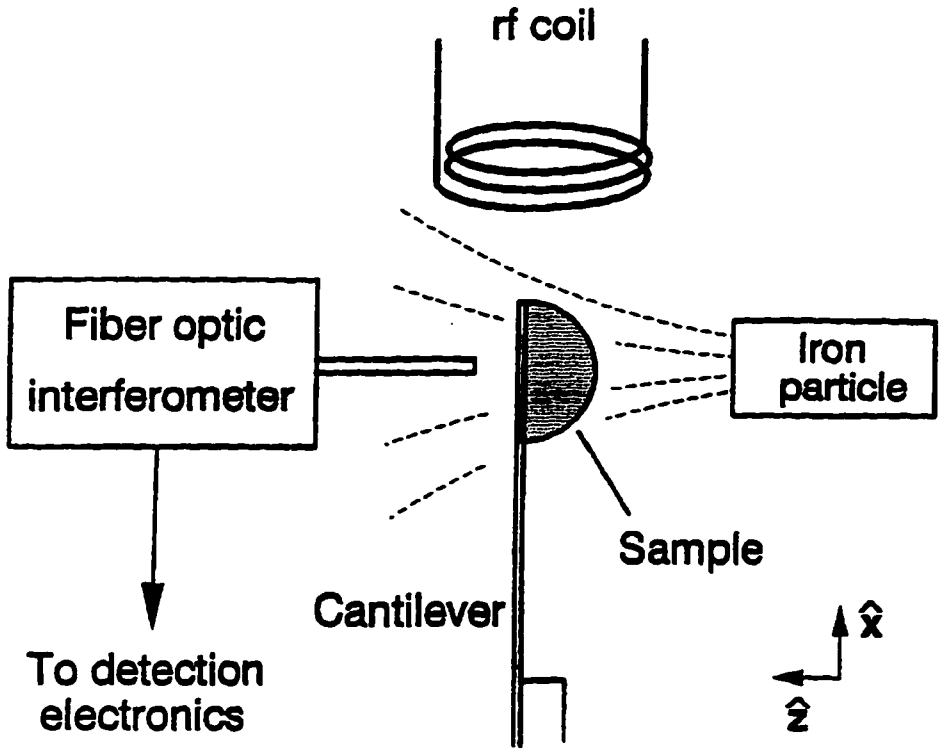

FIG 7.7. Experimental arrangement for mechanical detection NMR [Rugar, 1994].

The advantage with mechanical detection is that it has a much smaller minimum detectable force (discussed in chapter 2), so a smaller number of spins can be seen, thus, providing for better resolution. The improvement in F_{min} is primarily due to a higher Q and softer spring constant than can be achieved with a coil.

Appendix A

For quick reference, this appendix contains the dimensions of all currently used oscillators. CGS units are used for I's & κ's (g-cm^2 & dynes-cm). Frequency is in kHz. Neck to wing space is 0.1 cm.

SERIES B

	SECTION	WIDTH—LENGTH
#1	$I_h=1.04 \times 10^{-3}$	0.8 × 0.25
	$I_w=3.40 \times 10^{-2}$	0.8 × 0.85
	$\kappa_u=3.89 \times 10^{-6}$	0.12 × 0.3
	$\kappa_l=3.89 \times 10^{-6}$	0.12 × 0.3
	fr=13.8	

Table A.1. Standard Frequency.

SERIES C

	SECTION	WIDTH—LENGTH
#1	I_h=3.06 × 10^{-4}	0.8 × 0.08
	I_w=1.78 × 10^{-3}	0.4 × 0.425
	κ_u=4.87 × 10^{6}	0.08 × 0.14
	κ_l=4.87 × 10^{6}	0.08 × 0.14
	fr=21.9	

Table A.2. Frequency 1.

	SECTION	WIDTH—LENGTH
#2	I_h=1.30 × 10^{-4}	0.6 × 0.08
	I_w=1.78 × 10^{-3}	0.4 × 0.425
	κ_u=4.87 × 10^{6}	0.08 × 0.14
	κ_l=4.87 × 10^{6}	0.08 × 0.14
	fr=32.0	

Table A.3. Frequency 2.

	SECTION	WIDTH—LENGTH
#3	I_h=3.95 × 10^{-5}	0.4 × 0.08
	I_w=1.78 × 10^{-3}	0.4 × 0.425
	κ_u=4.87 × 10^{6}	0.08 × 0.14
	κ_l=4.87 × 10^{6}	0.08 × 0.14
	fr=56.4	

Table A.4. Frequency 3.

	SECTION	WIDTH—LENGTH
#4	I_h=2.48 × 10^{-4}	0.6 × 0.08
	I_w=1.78 × 10^{-4}	0.4 × 0.425
	κ_u=4.01 × 10^{6}	0.07 × 0.14
	κ_l=4.01 × 10^{6}	0.07 × 0.14
	fr=21.8	

Table A.5. Sensitive.

	SECTION	WIDTH—LENGTH
#5	I_h=4.24 × 10^{-4}	0.8 × 0.11
	I_w=1.78 × 10^{-4}	0.4 × 0.425
	κ_u=6.60 × 10^6	0.1 × 0.14
	κ_l=6.60 × 10^6	0.1 × 0.14
	fr=22.4	

Table A.6. Tough.

	SECTION	WIDTH—LENGTH
#6	I_h=3.06 × 10^{-4}	0.8 × 0.08
	I_w=1.78 × 10^{-4}	0.4 × 0.425
	κ_u=6.60 × 10^6	0.1 × 0.14
	κ_l=4.26 × 10^6	0.08 × 0.16
	fr=25.5	

Table A.7. Q-isolation.

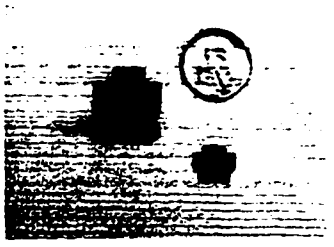

FIG. A.1. Left, Series B oscillator. Bottom, Series C oscillator.

For the NMR oscillators, SI units are used for I's & κ's (N-m^2 & N-m). Sections are in μm and frequencies are in kHz. The width for these oscillators is across "both" wings—there is no gap between the neck and wing. Oscillators spaced every 200 μm.

CURRENT NMR

	SECTION	WIDTH—LENGTH
#1	$I_h=1.53 \times 10^{-20}$	100 × 80
	$I_w=5.68 \times 10^{-20}$	150 × 100
	$\kappa_u=2.79 \times 10^{-9}$	14 × 40
	$\kappa_l=3.72 \times 10^{-9}$	14 × 30
	fr=79.5	

Table A.8. NMR Frequency 1.

	SECTION	WIDTH—LENGTH
#2	$I_h=2.18 \times 10^{-20}$	150 × 50
	$I_w=5.68 \times 10^{-20}$	150 × 100
	$\kappa_u=2.79 \times 10^{-9}$	14 × 40
	$\kappa_l=3.72 \times 10^{-9}$	14 × 30
	fr=71	

Table A.9. NMR Frequency 2.

	SECTION	WIDTH—LENGTH
#3	I_h=3.35 × 10^{-20}	150 × 70
	I_w=1.03 × 10^{-19}	150 × 140
	κ_u=2.79 × 10^{-9}	14 × 40
	κ_l=3.72 × 10^{-9}	14 × 30
	fr=55.6	

Table A.10. NMR Frequency 3.

	SECTION	WIDTH—LENGTH
#4	I_h=??? × 10^{-20}	150 × 25
	I_w=??? × 10^{-19}	200 × 120
	κ_u=??? × 10^{-9}	15 × 60
	κ_l=??? × 10^{-9}	15 × 50
	fr=???	

Table A.11. NMR Mystery Gamble.

	SECTION	WIDTH—LENGTH
#5	I=???	50 × 50
	κ=???	10 × 80
	fr=???	

Table A.12. NMR Paddle.

Appendix B

The program's path is *LABVIEW:AB:res location s ver 7 Aab&Ael.* Only the frequency synthesizer, lock-in amplifier and computer need to be connected to use the program. The front panel of the virtual instrument is shown in Fig. B.1. Most of the inputs are self explanatory. The cryptic ones are explained below.

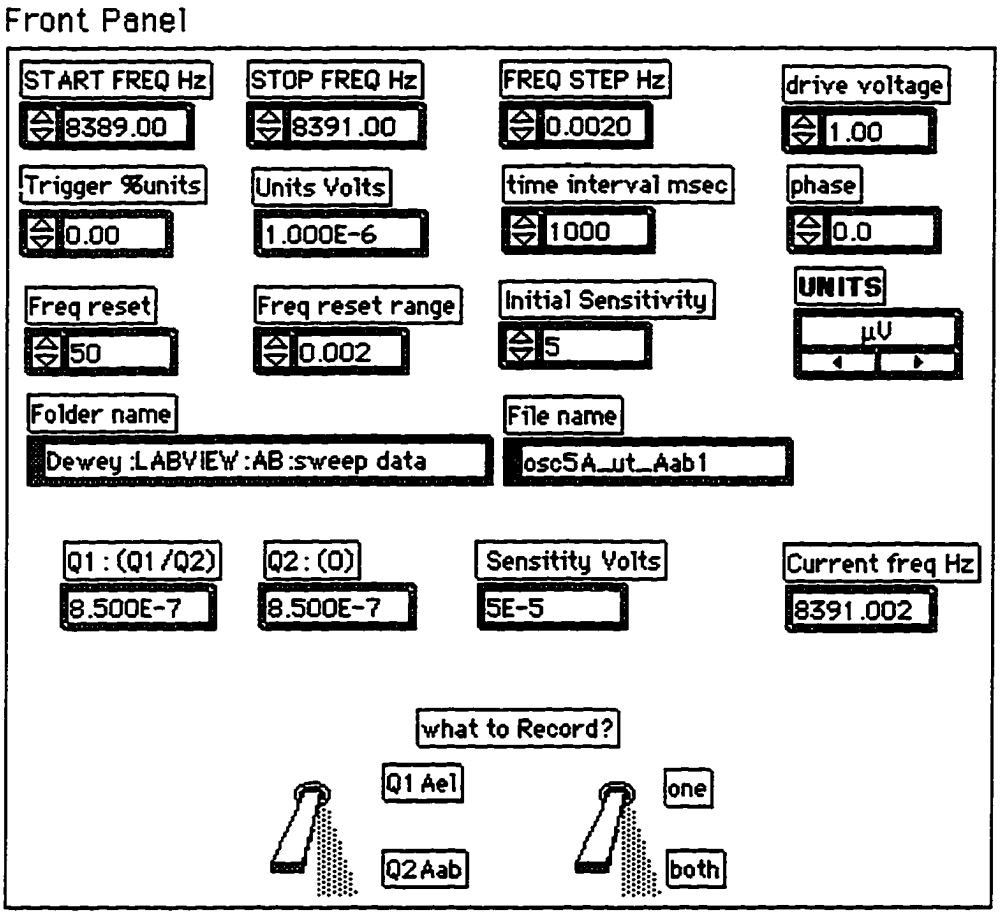

FIG. B.1. Front panel for LabView frequency sweeping program.

First, the *drive voltage* is the amplitude for the frequency synthesizer. It ought to be left at 1 V. It can be changed from one volt, but beware, occasionally it changes back. The *Trigger %units* is a threshold that allows data to be recorded. If this is set on 40%, for example, and the units are in the µV range, then unless Aab is greater than 0.4 µV, nothing will be recorded. To record all data points, set it to zero. The *time interval msec* is the time in milliseconds

between changing the frequency and recording the amplitude. The *Freq reset* is roughly the number of Hertz that is swept through before the lock-in is re-zeroed (i.e., any offsets that have developed are reset to zero). Over long or quick sweeps the lock-in will develope these. More specifically, if the current frequency divided by the *Freq reset* value is less than the *Freq reset range*, the lock-in will zero, otherwise it will not. For doing slow sweeps, *Freq reset range* should be set to zero so that the lock-in does not zero in the middle of a resonance. Jumping off a resonance and then suddenly back on is not wise, it is tantamount to kicking the oscillator! The *Initial Sensitvity* is the lock-in sensitivity on a particular *UNIT* scale. The lowest value corresponds to the lowest sensitivity. Make sure to be on a large enough scale to accommodate the peak value. The program will change scales if the amplitude is more than 90% of the current sensitivity, but play it safe.

Bibliography

[Abrikosov, 1957] A. A. Abrikosov, Soviet Phys.—JEPT **5**, 1174 (1957).

[Anderson, 1962] P. W. Anderson, Phys. Rev. Lett. **9**, 309 (1962).

[Balents, 1994] L. Balents and D. R. Nelson, Phys. Rev. Lett. **73**, 2618 (1994).

[Barr, 1995] A. L. Barr and J. T. Markert, Jour. of Superconductivity **8**, 667 (1995).

[Barr, 1996] A. L. Barr and J. T. Markert, Phys. Rev. Lett. **77**, 731 (1996).

[Bardeen, 1965] J. Bardeen and M.J. Stephen, Phys. Rev. **A140**, 1197 (1965).

[Bean, 1978] K. E. Bean, IEEE Trans. on Electronic Devices **ED-25**, 1185 (1978).

[Beck, 1992] R. G. Beck, D. E. Farrell, J. P. Rice, D. M. Ginsberg, and V. G. Kogan, Phys. Rev. Lett. **68**, 1594 (1992).

[Bohg, 1971] A. Bohg, J. Electrochem. Soc. **2**, 401 (1971).

[Blatter, 1992] G. Blatter, V. B. Geshkenbein, and A. I. Larkin, Phys. Rev. Lett. **68**, 875 (1992).

[Blatter, 1995] G. Blatter, M. V. Feigel'man, V. B. Geshkenbein, A. I. Larkin, and V. M. Vinokur, Rev. Mod. Phys. **66**, 1125 (1994).

[Braginsky, 1977] V. B. Braginsky and A. B. Manukin, *Measurement of Weak Forces in Physics Experiments*. Chicago: University of Chicago Press, (1977).

[Brandt, 1986] E. H. Brandt, P. Esquinazi, H. Neckel, and G. Weiss, Phys. Rev. Lett. **56**, 89 (1986).

[Brandt, 1991] E. H. Brandt, Phys. Rev. Lett. **67**, 2219 (1991).

[Brandt, 1992] E. H. Brandt, Phys. Rev. Lett. **68**, 3769 (1992).

[de Brion, 1991] S. de Brion, R. Calemczuk, and J. Y. Henry, Physica C **178**, 225 (1991).

[Brongersma, 1993] S. H. Brongersma, E. Verweij, N. J. Koeman, D. G. de Groot, R. Griessen, and B. I. Ivlev, Phys. Rev. Lett. **71**, 2319 (1993).

[Burns, 1990] D. W. Burns and H. Guckel, J. Vac. Sci. Technol. A **8**, 3606 (1990).

[Cobb, 1994] J. L. Cobb and J. T. Markert, Physica C **226**, 235 (1994).

[Cooper, 1956] L. N. Cooper, Phys. Rev. **104**, 1189 (1956).

[Crabtree, 1995] G. W. Crabtree, W. K. Kwok, U. Welp, J. Fendrich, C. J. van der Beek, V. K. Vlasko-Vlasov, V. I. Nikitenko, D. Gunter, and T. Gardiner, Invited Paper at the International Seminar on Superconductors in High Magnetic Fields. National Research Institute for Metals: Japan, (1995).

[Crawford, 1968] F. S. Crawford, *Waves: berkeley physics course-volume 3*. New York: McGraw-Hill, (1968).

[De Long, 1992] Lance E. De Long, Zhigang Xu, Ji-Chang Hou, and Joseph Brill, *High Temperature Superconductors*. S. K. Malik and S. S. Shah, Editors. New York: Nova Science Publishers, (1992).

[Dong–Ho, 1990] W. Dong–Ho and S. Sridhar, Phys. Rev. Lett. **65**, 2074 (1990).

[Durig, 1992] U. Durig, O. Zuger, and A. Stalder, J. Appl. Phys. **72**, 1778 (1992).

[Dearnaley, 1973] G. Dearnaley, J. H. Freeman, R. S. Nelson, and J. Stephen, *Ion Implantation*. North Holland: New York, (1973).

[Feinberg, 1990] D. Feinberg and C. Villard, Phys. Rev. Lett. **65**, 919 (1990).

[Feinberg, 1993] D. Feinberg and A. M. Ettouhami, Int. J. Mod. Phys. B **7**, 2085 (1993).

[Finne, 1967] R. M. Finne and D. L. Klein, J. Electrochem. Soc. **114**, 965 (1967).

[Flesher, 1993] S. Fleshler, W-K. Kwok, U. Welp, V. M. Vinokur, M. K. Smith, J. Downey, and G. W. Crabtree, Phys. Rev. B **47**, 14 448 (1993).

[Gammel, 1988] P. L. Gammel, L. F. Schneemeyer, J. V. Waszczak, and D. J. Bishop, Phys. Rev. Lett. **61**, 1666 (1988).

[Giapintzakis, 1989] J. Giapintzakis, D. M. Ginsberg, and P. D. Han, J. of Low Temp. Phys **77**, 155 (1989).

[Gibbons, 1975] J. F. Gibbons, W. S. Johnson, and S. W. Mylroie, *Projected Range Statistics*. Dowden, Hutchinson, and Ross: Stoudsburg, (1975).

[Ginzburg, 1950] V. L. Ginzburg and L.D. Landau, Zh. Eksperim. I. Teor. Fiz. **20**, 1964 (1950).

[Ghandhi, 1983] S. K. Ghandhi, *VLSI Fabrication Principles: Silicon and Gallium Arsenide*. New York: John Wiley & Sons, (1983).

[Golosovsky, 1992] M. Golosovsky, Y. Naveh, and D. Davidov, Phys. Rev. B **45**, 7495 (1992).

[Gray, 1972] D. E. Gray (editor), *American Institute of Physics Handbook*. New York: McGraw Hill, (1972).

[Heon, 1993] S. Heon, O. Zuger, C. S. Yannoni, H. J. Mamin, K. Wago, D. Rugar, Fabrication of Ultrasensitive Force Detectors. Not availible, (1993).

[Hunnekes, 1994] C. Hunnekes, H. G. Bohn, W. Schilling, and H. Schulz, Phys. Rev. Lett. **72**, 2271 (1994).

[Jorgensen, 1990] J. D. Jorgensen, B. W. Veal, A. P. Paulikas, L. J. Nowicki, G. W. Crabtree, H. Claus, W. K. Kwok, Physical Review B **41**, 1863 (1990).

[Kaminsky, 1985] G. Kaminsky, J. Vac. Sci. Technol. B **3**, 1015 (1985).

[Kendall, 1990] D. L. Kendall, J. Vac. Sci. Technol. A **8**, 3598 (1990).

[Kleiman, 1985] R. N. Kleiman, G. K. Kaminsky, J. D. Reppy, R. Pindak, and D. J. Bishop, Rev. Sci. Instrum. **56**, 2088 (1985).

[Krusin-Elbaum, 1993] L. Krusin-Elbaum, L. Civale, F. Holtzberg, and C. Feild, Physica A **200**, 314 (1993).

[Kwok, 1992] W. K. Kwok, S. Flesher, U. Welp, V. M. Vinokur, J. Downey, and G.W. Crabtree, Phys. Rev. Lett. **69**, 3370 (1992).

[Kwok, 1994] W. K. Kwok, J. Fendrich, U. Welp, S. Flesher, J. Downey, and G.W. Crabtree, Phys. Rev. Lett. **72**, 1088 (1994).

[Lawrence, 1971] W. E. Lawrence and S. Doniach, in E. Kanda (ed.) Proc. 12th Int. Conf. Low Temp. Phys. (Kyoto, 1970; Keigaku, Tokyo, 1971), p. 361.

[Lee, 1969] D. B. Lee, J. Appl. Phys. **40**, 4569 (1969).

[Maki, 1966] K. Maki, Phys. Rev. **148**, 362 (1966).

[Moore, 1989] J. H. Moore, C. C. Davis, M. A. Coplan, *Building Scientific Apparatus*. New York: Addison–Wesley, (1989).

[Nelson, 1989] D. R. Nelson, J. Stat. Phys. **57**, 511 (1989).

[Oussena, 1994] M. Oussena, P. A. J. de Groot, R. Gagnon, and L. Taillefer, Phys. Rev. Lett. **72**, 3606 (1994).

[Palstra, 1988] T. T. Palstra, B. Batlogg, L. F. Schneemeyer, and J. V. Waszczak, Phys. Rev. Lett. **61**, 1662 (1988).

[Qiu, 1993] X. Qiu and M. Tachiki, Physica C **207**, 255 (1993).

[Palik, 1982] E. D. Palik, J. W. Faust, Jr., H. F, Gray, and P. F. Green, J. Electrochem. Soc. **129**, 2051 (1982).

[Palstra, 1990] T. T. M. Palstra, B. Batlog, R. B. van Dover, L. F. Schneemeyer, and J. V. Waszczak, Phys. Rev. B **41**, 6621 (1990).

[Phelps, 1994] R. B. Phelps, P. Akavoor, L. L. Kesmodel, A. L. Barr, J. T. Markert, J. Ma, J. Kelley, and M. Onellion, Phys. Rev. B. **50**, 6526 (1994).

[Prescesky, 1992] S. Prescesky, M. Parameswaran, A. Rawicz, R. F. B Turner, and U. Reichl, Can. J. Phys. **70**, 1178 (1992).

[Robbins, 1960] H Robbins and B. Schwartz, J. Electrochem. Soc. **107**, 108 (1960).

[Reisman, 1979] A. Reisman, M. Berkenblit, S. A. Chan, F. B Kaufman, and D. C. Green, J. Electrochem. Soc. **126**, 1406 (1979).

[Rugar, 1994] D. Rugar, O. Zuger, S. Hoen, C. S. Yannoni, H, -M. Vieth, R. D. Kendrick, Science **264**, 1560 (1994).

[Runyan, 1990] W. R. Runyan, K. E. Bean, *Semiconductor Integrated Circuit Processing Technology*.. New York: Addison–Wesely, (1990).

[Saint-James, 1969] D. Saint-James, E. J. Thomas, and G. Sarma, *Type II Superconductivity* (Pergamon Press, London, (1969).

[Schleger, 1990] P. Schleger, W. N. Hardy, and B. X. Yang, Physica C **176** 261 (1990).

[Seidel, 1970] T. E. Seidel and A. U. MacRae, Some Properties of Ion Implanted Boron in Silicon: Trans. Met. Soc. AIME **245**, 491 (1969).

[Sidles, 1992] J. A. Sidles, J. L. Garbini, and G. P. Drobny, Rev. Sci Instrum. **63**, 3881 (1992).

[Swartz, 1985] J. M. Swartz and L. G. Rubin, *Fundamentals for Usage of Cryogenic Temperature Controllers*. (Application note). LakeShore Cryogenic, Inc. (1985).

[Tachiki, 1989] M. Tachiki and S. Takahashi, Solid Sate Commun. **70**, 291 (1989).

[Timoshenko, 1970] S. D. Timoshenko and J. N. Goodier, *Theory of Elasticity*. New York: McGraw-Hill, (1970).

[Tinkham, 1996] M. Tinkham, *Introduction to Superconductivity* . McGraw-Hill, Inc., New York, (1996).

[Veal, 1991] B. W. Veal and A. P. Paulikas, Physica C **184**, 321 (1991).

[Veal, 1990] B. W. Veal, A. P. Paulikas, Hoydoo Hou, Hao Shi, Y. Fang, and J. W. Downey, Physical Review B **42**, 6305 (1990).

[Welp, 1989a] U. Welp, M. Grimsditch, H. You, W. K. Kwok, M. M. Fang, G.W. Crabtree, and J.Z. Liu, Physica C **161**, 1 (1989).

[Welp, 1989b] U. Welp, W. K. Kwok, G. W. Crabtree, K. G. Vandervoort, and J. Z. Liu, Phys. Rev. Lett. **62**, 1908 (1989).

[Werthamer, 1966] N. R. Werthamer, E. Helfand, and P. C. Hohenberg, Phys. Rev. **147**, 295 (1966).

[White, 1987] G. K. White, *Experimental Techniques in Low–Temperature Physics*. OxfordUniversity Press, New York (1987).

[Young, 1989] Warren C. Young, *Roark's Formulas for Stress and Strain*. New York: McGraw-Hill, (1989).

[Ziese, 1994a] M. Ziese, P. Esquinazi, and H. F. Braun, Supercond. Sci. Technol. **7**, 869 (1994).

[Ziese, 1994b] M. Ziese, P. Esquinazi, Y. Kopelevich, and A. B. Sherman, Physica C

Vita

"They" say a picture is worth a thousand words.... A picture of Alexander Lloyd Barr is shown below. It is left as an exercise for the reader's imagination to make a vita for the author. (Do not try drinking liquid nitrogen at home—it could be lethal and is definitely NOT good for your teeth!)

Permanent address: ra5549@email.sps.mot.com

This dissertation was typed by the mad Dr. Cryo.